INVESTIGATION OF IDLING INSTABILITIES IN WIND TURBINE SIMULATIONS

Master of Science Thesis

For obtaining the degree of Master of Science in Engineering Wind Energy at Technical University of Denmark and in Aerospace Engineering at Delft University of Technology

Garry Yuan, Kwan

31 July 2017

Wind Energy Research Group, Faculty of Aerospace Engineering, Delft University of Technology

Dr. J. G. Holierhoek / Dr. M. H. Hansen

Abstract

Idling instabilities of large wind turbines in extreme winds is a relatively well known problem for manufacturers, at least in terms of the results in calculations. However, many are still sceptical of how realistic such instabilities are in actuality due to limitations in the current state of the art aeroelastic tools.

The overall aim of this thesis is twofold. Firstly, through the use of analytical solutions for a parked blade developed by adapting existing formulations for the aerodynamic damping forces as well as numerical means in the form of the aeroelastic tool Focus 6, Phatas, versions 9083 and 10041 (kindly provided by WMC), this thesis aims to determine how parameters relating to the local angle of attack of a wind turbine blade contribute towards inducing idling instabilities in large wind turbines and to subsequently identify the underlying mechanisms that drive such instabilities to occur in simulations. Subsequently, from the results gathered from the analyses, the second goal is to then determine if the current state of the art aeroelastic tools are able to reasonably capture such instabilities. The reference wind turbine used in this thesis was the NREL 5mW turbine.

The method used to obtain the results in the analytical solutions were first validated against existing literature and generally showed good agreement in the trends. The analytical solutions showed the aerodynamic damping values of a blade section at various nacelle yaw, rotor azimuth as well as blade pitch angles. The results from the analytical solutions showed that under certain conditions, idling instabilities were present.

The results of the numerical simulations when first run with quasi steady aerodynamics and a constant wind profile showed good agreement with the analytical results (and also existing literature) and also suggested that the instabilities were driven by the edgewise modes of the tubine. Assessment of the outputs after the inclusion of dynamic stall (where simulations were largely limited to angles of attack between -45° and 45° as this was the range where the dynamic stall model was applied in its full extent) as well as turbulence to further simulations showed that Focus 6, Phatas still calculated instabilities at settings close to the analytical solutions' predictions.

As a final conclusion, this thesis provided a theoretical basis to argue for the case of idling instabilities being a possible issue. The numerical simulations largely support the findings of the analytical solutions where an assessment of the numerical results gave no indications to suggest otherwise.

Acknowledgements

No man is an island entire of itself.

– John Donne

The completion of this thesis would not have been possible without the help of and presence of not only God, but the numerous extraordinary people I have encountered during these two years who have contributed to its success in many ways.

Firstly, I would like to express my utmost gratitude to my main supervisor, Dr Jessica Holierhoek. I am extremely fortunate to be your student. Your patience and guidance borne from your passion to teach has made a lasting impact on me for which I am very grateful.

I would also like to thank Prof Morten Hansen for agreeing to be my DTU supervisor. I always value the feedback that you are able to provide and only regret that I was not able to liaise with you more regularly as the process leading up to the completion of this thesis was not as smooth as I had hoped for it to be.

Mr Remco Brood and Koert Lindenburg from WMC were instrumental in not only giving me a better understanding of Focus, Phatas but also never seemed too busy to take the time and help me with menial tasks such as resetting the queue or answering simple questions. I thank your both for your consummate professionalism.

Coming to Europe to undertake this master's course has also afforded me the chance to meet new people and forge new friendships. I am grateful for the times we have shared and also the countless hours spent helping to get me across the finish line. It is my wish that we will be able to keep our friendship for a long time to come.

I would also like to thank Alex Chu, a former mentor in Singapore Technologies Aerospace, who challenged me to find my passion and pursue it fiercely.

Having the support of one's family can be a powerful thing and I am always truly grateful for mine for always being there for me and supporting my decisions and goals in life.

Finally, I would like to dedicate this thesis to my fiancée, Jasmine who has been the personification of patience and love especially during these two difficult years apart.

Table of Contents

Nomenclature

R, r - Radius of rotor blade in meters with a capitalized R denoting the radial length of the blade from root to tip

Ω - Angular velocity in radians per second

ψ - Rotor azimuth in degrees

γ - Nacelle yaw angle in degrees

α - Angle of attack in degrees

dL - Lift force per unit length in newtons

ρ - Air density in kgm^{-3}

c - Chord length in meters

$c_L(r, \alpha)$ - Lift coefficient at radius 'r' as a function of α

dD - Drag force per unit length in newtons

$c_D(r, \alpha)$ - Drag coefficient at radius 'r' as a function of α

F_{xR} - Force per unit length in the xR direction in newtons per meter

F_{yR} - Force per unit length in the yR direction in newtons per meter

θ_{sp} - Structural pitch angle in degrees

θ_p - Blade pitch angle in degrees

β - Blade twist in degrees

ϕ - Transformation angle in degrees

V_{rel} - Relative wind velocity in meters per second

V - Freestream velocity acting on a rotating turbine blade section in meters per second

$U_{iner,rot}$ - Longitudinal wind component in the inertial or rotated frame in meters per second

$V_{iner,rot}$ - Lateral wind component in the inertial or rotated frame in meters per second

$W_{iner,rot}$ - Vertical wind component in the inertial or rotated frame in meters per second

c_{xx}^{R} - Aerodynamic damping force in kilograms per meter seconds in the rotor plane, R, in the xx direction. The subscript and superscript are dependent on the direction along the axis as well as the definition of the plane respectively.

δ - Logarithmic decrement in percentage

ζ - Damping ratio in percentage

1. Introduction

1.1 Background

The effects of aeroelasticity, which is loosely defined as *the significant interaction between an elastic structure and an airflow,* has its roots in the aeronautical field where it has been studied since the birth of manned flight in the early 1900s (Garrick & Reed, 1981).

The study of aeroelastic instabilities in wind turbines by comparison is relatively new, starting as late as the 1990s (M. H. Hansen, 2007). This is attributed to the fact that the accumulation of knowledge in this field has been mainly consequence driven. The 1990s saw a large improvement in manufacturing processes and refinement of blade designs in order to produce increasingly efficient, state of the art stall regulated wind turbines, which was the dominant type of wind turbines at the time. However, these improvements also led to the introduction of excessive edgewise vibrations which had not been seen before. In trying to determine the root cause of these vibrations, huge strides were made in understanding the adverse effects of aeroelasticity in wind turbines. These include the development of models that could define the effective aerodynamic damping values with quasi steady aerodynamics as well as the inclusion of unsteady aerodynamics to simulate dynamic stall, both of which are still very much used in the current state of the art aeroelastic analyses of wind turbines (Riziotis, Voutsinas, Politis, & Chaviaropoulos, 2004).

In looking to the wind turbines of tomorrow, the next step forward in terms of blade design is a continual focus on developing increasingly longer and more slender blades in order to get round the square-cube law (where linearly upscaling wind turbines will roughly increase the cost by a factor of the cube of its radius, R^3, whilst the power only increases by a factor of R^2) and minimise the levelized cost of energy (LCoE).

With the knowledge gained in understanding aeroelasticity in wind turbines thus far, apart from edgewise vibrations still being an issue, two other major potential problems have been identified in the pursuit of this design trend. They are, classical flutter and idling instabilities (M. O. L. Hansen, Sørensen, Voutsinas, Sørensen, & Madsen, 2006).

With regards to the latter problem, little research has been done. This is partly due to the present limitations in the current state of the art aeroelastic tools in terms of being able to accurately model the aerodynamics in deep stall as well as due to the fact that many people do not believe that the risk of instabilities in idling is warranted.

However, what research that has been done on this topic (elaborated on in the following chapter) does indicate that idling instabilities will indeed be a problem. Despite the technological limitations, there is still meaningful work that can be done in order to provide a more complete understanding of the phenomenon.

1.2 Formulation of objective

The main goal of this thesis is twofold. The first, is an overarching goal of determining if the current state of the art tools are reasonable in identifying idling instabilities. The second goal is to determine how parameters relating to the local angle of attack of a wind turbine blade contribute towards inducing idling instabilities in large wind turbines and to subsequently identify the underlying mechanisms that drive such instabilities to occur in simulations.

In order to achieve this, analytical solutions based on Petersen (Petersen et al., 1998) were firstly used to derive equations for the aerodynamic damping values of a parked wind turbine blade.

Based on the trends seen in the analytical solutions, certain values for each parameter were identified after which numerical solutions were then performed using Focus 6, Phatas, which was kindly provided by The Knowledge Centre Wind Turbine Materials and Construction (WMC) using both quasi steady as well as unsteady aerodynamics with a dynamic stall model based on Snel (Snel, 1997).

Details of the findings will be discussed in further detail through the course of this thesis.

1.3 Description of reference wind turbine

The final section in this chapter aims to give a brief introduction to the reference wind turbine used throughout the duration of this thesis in both the analytical equations as well as the numerical simulations. The wind turbine chosen is the 5MW reference wind turbine developed by the National Renewable Energy Laboratory (NREL) in the United States of America (Jonkman, Butterfield, Musial, & Scott, 2009).

The design of NREL's wind turbine is a composite one that combines aspects from many existing models and wind turbines available at the time of its conception, especially the DOWEC project which most of the blade design was based on. The table below details some of the general properties of the wind turbine and is taken from NREL's report.

Table 1.1: Gross properties of the NREL 5MW reference wind turbine taken from (Jonkman et al., 2009)

Rating	5 MW
Rotor Orientation, Configuration	Upwind, 3 Blades
Control	Variable Speed, Collective Pitch
Drivetrain	High Speed, Multiple-Stage Gearbox
Rotor, Hub Diameter	126 m, 3 m
Hub Height	90 m
Cut-In, Rated, Cut-Out Wind Speed	3 ms^{-1}, 11.4 ms^{-1}, 25 ms^{-1}
Cut-In, Rated Rotor Speed	6.9 rpm, 12.1 rpm
Rated Tip Speed	80 ms^{-1}

Overhang, Shaft Tilt, Precone	5 m, 5°, 2.5°
Rotor Mass	110000 kg
Nacelle Mass	240000 kg
Tower Mass	347460 kg
Coordinate Location of Overall CM	(-0.2 m, 0.0 m, 64.0 m)

It should be noted that the rotor diameter shown in Table [1.1] excludes the effects of the precone. Apart from the general properties, of special interest for the purpose of this thesis are the aerodynamic properties of the blades as well as the natural frequencies of the turbine.

Table 1.2: Distributed blade aerodynamic properties of the NREL 5MW reference wind turbine taken from (Jonkman et al., 2009)

Node (-)	Rnodes (m)	AeroTwst (°)	DRNodes (m)	Chord (m)	Airfoil Table (-)
1	2.8667	13.308	2.7333	3.542	Cylinder1.dat
2	5.6000	13.308	2.7333	3.854	Cylinder1.dat
3	8.3333	13.308	2.7333	4.167	Dylinder2.dat
4	11.7500	13.308	4.1000	4.557	DU40_A17.dat
5	15.8500	11.480	4.1000	4.652	DU35_A17.dat
6	19.9500	10.162	4.1000	4.458	DU35_A17.dat
7	24.0500	9.011	4.1000	4.249	DU30_A17.dat
8	28.1500	7.795	4.1000	4.007	DU25_A17.dat
9	32.2500	6.544	4.1000	3.748	DU25_A17.dat
10	36.3500	5.361	4.1000	3.502	DU21_A17.dat
11	40.4500	4.188	4.1000	3.256	DU21_A17.dat
12	44.5500	3125	4.1000	3.010	NACA64_A17.dat
13	48.6500	2.319	4.1000	2.764	NACA64_A17.dat
14	52.7500	1.526	4.1000	2.518	NACA64_A17.dat
15	56.1667	8.863	2.7333	2.313	NACA64_A17.dat
16	58.9000	0.370	2.7333	2.086	NACA64_A17.dat
17	61.6333	0.106	2.7333	1.419	NACA64_A17.dat

Table [1.2] shows the discretization of the blade into 17 elements with the nodes located in the centre of each element. Rnodes denotes the radial position of the nodes and DRNodes denotes the length of each element. The two cylinders in elements 1 – 3 have a drag coefficient of 0.5 and 0.35 respectively.

The airfoil data used for the blade have been corrected for 3D effects in three ways.

1. The lift coefficients are corrected with the Du-Selig method (Du & Selig, 1998) and the drag coefficients are corrected with the Eggers method (Eggers, Chaney, & Digumarthi, 2003) for an angle of attack range from 0° to 90°.

2. The drag coefficients were further corrected in the same range via the Viterna method using an aspect ratio of 17 (Viterna & Janetzke, 1982).
3. Finally, the Beddoes-Leishman dynamic stall hysteresis parameters were estimated. However, since the dynamic stall model used later on is based on (Snel, 1997), this would be inconsequential.

Knowing the corrections used in the airfoil data is especially important later on when they are used in the numerical simulations in order to avoid double correcting of the data.

Lastly, the natural frequencies of the turbine are presented.

Table 1.3: Full system natural frequencies in Hz of the NREL 5MW reference wind turbine taken from (Jonkman et al., 2009)

Mode	Description	FAST	ADAMS
1	1st Tower Fore-Aft	0.3240	0.3195
2	1st Tower Side-to-Side	0.3120	0.3164
3	1st Drivetrain Torsion	0.6205	0.6094
4	1st Blade Asymmetric Flapwise Yaw	0.6664	0.6296
5	1st Blade Asymmetric Flapwise Pitch	0.6675	0.6686
6	1st Blade Collective Flap	0.6992	0.7019
7	1st Blade Asymmetric Edgewise Pitch	1.0793	1.0740
8	1st Blade Asymmetric Edgewise Yaw	1.0898	1.0877
9	2nd Blade Asymmetric Flapwise Yaw	1.9337	1.6507
10	2nd Blade Asymmetric Flapwise Pitch	1.9223	1.8558
11	2nd Blade Collective Flap	2.0205	1.9601
12	2nd Tower Fore-Aft	2.9003	2.8590
13	2nd Tower Side-to-Side	2.9361	2.9408

Table [1.3] shows the natural frequencies as calculated from both FAST and ADAMS from eigenvalue analyses setting the aerodynamic damping values to zero at 0° pitch and with the brake activated in order to avoid the rigid-body drivetrain mode.

2. Literature Review

This literature review expands on the various engineering concepts that were researched during the course of this thesis. The content in each of the subtopics presented in this literature review was pertinent in helping to meet the objectives as stated in the first chapter of this report.

2.1 Derivation of aerodynamic damping values with quasi steady aerodynamics

The aerodynamic damping equations derived for a parked wind turbine in the later portion of this thesis were adapted from existing aerodynamic damping models found in Petersen's *Prediction of Dynamic Loads and Induced Vibrations in Stall* (Petersen et al., 1998). In the aforementioned paper, Petersen derived linearized expressions for the aerodynamic damping values for 2-D quasi steady aerodynamics of an airfoil section that is free to translate in the edgewise and flapwise directions as well as rotate about its aerodynamic centre. Although such equations are simplified, they have proven to be useful and fairly accurate in looking at the damping characteristics of blades. Understanding how these equations are derived is fundamental before they can be adapted to suit the requirements of this thesis. As such, this section aims to provide a summary of Petersen's original derivations.

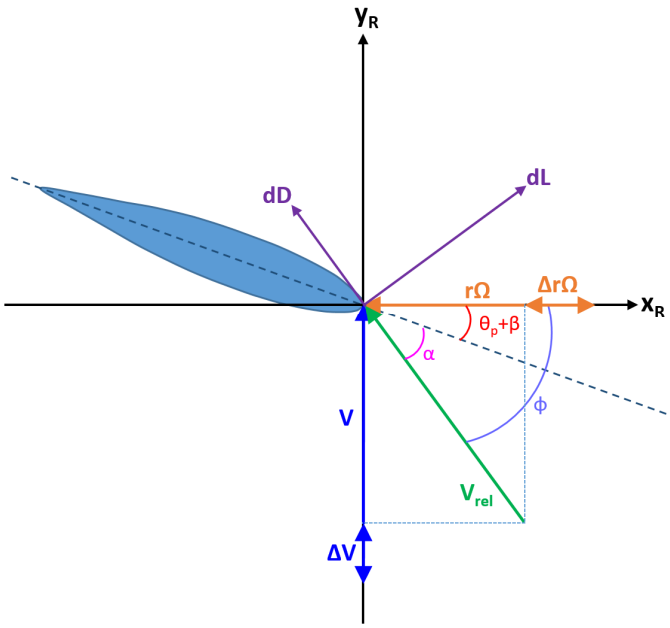

Figure 2.1: General components of the velocity triangle

The blade element theory is used as a starting point to express the lift and drag per unit length, dL and dD respectively as follows:

$$dL = \frac{1}{2}\rho V_{rel}(r)^2 c(r) c_L(r,\alpha) \qquad \text{Eqn 2.1}$$

$$dD = \frac{1}{2}\rho V_{rel}(r)^2 c(r) c_D(r,\alpha) \quad \text{Eqn 2.2}$$

Where V_{rel} is the relative wind speed and is determined by:

$$V_{rel} = \sqrt{V^2 + (r\Omega)^2} \quad \text{Eqn 2.3}$$

These forces can be projected into normal and tangential forces in the axes of the rotor plane, y_R and x_R respectively, via a transformation matrix as follows:

$$\begin{Bmatrix} {F_x}^R \\ {F_y}^R \end{Bmatrix} = \begin{bmatrix} \sin\phi & -\cos\phi \\ \cos\phi & \sin\phi \end{bmatrix} \begin{Bmatrix} dL \\ dD \end{Bmatrix} \quad \text{Eqn 2.4}$$

These forces are linearized at an arbitrary initial condition V_0 and $r\Omega_0$ as follows:

$$\begin{aligned} &{F_x}^R(V_0 + \Delta V, r\Omega_0 + \Delta r\Omega) \\ &\qquad = {F_x}^R(V_0, r\Omega_0) + \frac{\partial {F_x}^R(V_0, r\Omega_0)}{\partial V}\Delta V \\ &\qquad + \frac{\partial {F_x}^R(V_0, r\Omega_0)}{\partial r\Omega}\Delta r\Omega \end{aligned} \quad \text{Eqn 2.5}$$

$$\begin{aligned} &{F_y}^R(V_0 + \Delta V, r\Omega_0 + \Delta r\Omega) \\ &\qquad = {F_y}^R(V_0, r\Omega_0) + \frac{\partial {F_y}^R(V_0, r\Omega_0)}{\partial V}\Delta V \\ &\qquad + \frac{\partial {F_y}^R(V_0, r\Omega_0)}{\partial r\Omega}\Delta r\Omega \end{aligned} \quad \text{Eqn 2.6}$$

The equations can be arranged into matrix notation as follows:

$$\begin{Bmatrix} {F_x}^R \\ {F_y}^R \end{Bmatrix} = \begin{Bmatrix} {F_{x_0}}^R \\ {F_{y_0}}^R \end{Bmatrix} + \begin{bmatrix} \frac{\partial {F_{x_0}}^R}{\partial r\Omega} & \frac{\partial {F_{x_0}}^R}{\partial V} \\ \frac{\partial {F_{y_0}}^R}{\partial r\Omega} & \frac{\partial {F_{y_0}}^R}{\partial V} \end{bmatrix} \begin{Bmatrix} \Delta r\Omega \\ \Delta V \end{Bmatrix} \quad \text{Eqn 2.7}$$

The velocity increments ΔV and ΔrΩ can alternatively be expressed in terms of the rate of change in displacements in the rotor plane as follows:

$$\Delta V = -\dot{y}_R = \frac{dy_R}{dt} \quad \text{Eqn 2.8}$$

$$\Delta r\Omega = \dot{x_R} = \frac{dx_R}{dt} \quad \text{Eqn 2.9}$$

Hence, the forces can be rewritten as:

$$\begin{Bmatrix} {F_x}^R \\ {F_y}^R \end{Bmatrix} = \begin{Bmatrix} {F_{x_0}}^R \\ {F_{y_0}}^R \end{Bmatrix} - \begin{bmatrix} -\frac{\partial {F_{x_0}}^R}{\partial r\Omega} & \frac{\partial {F_{x_0}}^R}{\partial V} \\ -\frac{\partial {F_{y_0}}^R}{\partial r\Omega} & \frac{\partial {F_{y_0}}^R}{\partial V} \end{bmatrix} \begin{Bmatrix} \dot{x}_R \\ \dot{y}_R \end{Bmatrix} \quad \text{Eqn 2.10}$$

In a general form, this expression can be rewritten as follows:

$$\{F_\alpha^R\} = \{{F_{\alpha_0}}^R\} - [c_\alpha^R]\{\dot{u}^R\} \quad \text{Eqn 2.11}$$

Where the aerodynamic damping terms are:

$$[c_\alpha^R] = \begin{bmatrix} c_{xx}^R & c_{xy}^R \\ c_{yx}^R & c_{yy}^R \end{bmatrix} = \begin{bmatrix} -\frac{\partial {F_{x_0}}^R}{\partial r\Omega} & \frac{\partial {F_{x_0}}^R}{\partial V} \\ -\frac{\partial {F_{y_0}}^R}{\partial r\Omega} & \frac{\partial {F_{y_0}}^R}{\partial V} \end{bmatrix} \quad \text{Eqn 2.12}$$

From Eqn [2.12], the equations can be then worked out. Taking $c_{xx}{}^R$ as an example,

$$\begin{aligned} {c_{xx}}^R &= -\frac{\partial {F_x}^R}{\partial r\Omega} = -\frac{\partial}{\partial r\Omega}(\sin\phi\, dL - \cos\phi\, dD) \\ &= -\frac{\partial}{\partial r\Omega}\left[\sin\phi\left(\frac{1}{2}\rho c {V_{rel}}^2 cl\right) - \cos\phi\left(\frac{1}{2}\rho c {V_{rel}}^2 cd\right)\right] \\ &= -\frac{1}{2}\rho c\left[\frac{\partial}{\partial r\Omega}(V V_{rel} cl) - \frac{\partial}{\partial r\Omega}(r\Omega V_{rel} cd)\right] \\ &= -\frac{1}{2}\rho c\left[Vcl\frac{\partial V_{rel}}{\partial r\Omega} + V V_{rel} cl_\alpha \frac{\partial \alpha}{\partial r\Omega} - \left(V_{rel} cd + r\Omega cd\frac{\partial V_{rel}}{\partial r\Omega} + r\Omega V_{rel} cd_\alpha \frac{\partial \alpha}{\partial r\Omega}\right)\right] \end{aligned}$$

Where:

$$\frac{\partial V_{rel}}{\partial r\Omega} = \frac{r\Omega}{V_{rel}} \quad \text{and} \quad \frac{\partial \alpha}{\partial r\Omega} = \frac{\partial \sin^{-1}\frac{V}{V_{rel}}}{\partial r\Omega} = -\frac{V}{{V_{rel}}^2}$$

$$\begin{aligned} {c_{xx}}^R &= -\frac{1}{2}\rho c\frac{r\Omega}{V_{rel}}\left(Vcl - \frac{V^2}{r\Omega}cl_\alpha - \frac{{V_{rel}}^2}{r\Omega}cd - r\Omega cd + Vcd_\alpha\right) \\ \boldsymbol{{c_{xx}}^R} &= \boldsymbol{-\frac{1}{2}\rho c\frac{r\Omega}{V_{rel}}\left[\left(\frac{2r^2\Omega^2 + V^2}{r\Omega}\right)cd - Vcd_\alpha - Vcl + \frac{V^2}{r\Omega}cl_\alpha\right]} \end{aligned} \quad \text{Eqn 2.13}$$

The rest of the equations can be worked out similarly to give:

$$\boldsymbol{{c_{yy}}^R = \frac{1}{2}\rho c\frac{r\Omega}{V_{rel}}\left[\left(\frac{2V^2 + r^2\Omega^2}{r\Omega}\right)cd + Vcd_\alpha + Vcl + r\Omega cl_\alpha\right]} \quad \text{Eqn 2.14}$$

$$\boldsymbol{{c_{xy}}^R = \frac{1}{2}\rho c\frac{r\Omega}{V_{rel}}\left[\left(\frac{2V^2 + r^2\Omega^2}{r\Omega}\right)cl + Vcl_\alpha - Vcd - r\Omega cd_\alpha\right]} \quad \text{Eqn 2.15}$$

$$\boldsymbol{{c_{yx}}^R = \frac{1}{2}\rho c\frac{r\Omega}{V_{rel}}\left[\left(\frac{2r^2\Omega^2 + V^2}{r\Omega}\right)cl + Vcl_\alpha - Vcd + \frac{V^2}{r\Omega}cd_\alpha\right]} \quad \text{Eqn 2.16}$$

As a final step, if the structural properties of a blade's cross section is known, it is possible to determine the section's structural pitch angle, θ_{sp}. This angle defines the stiffest and most flexible directions of the section. By transforming the aerodynamic damping equations in the rotor plane about the structural pitch angle, one is able to determine a blade section's edgewise and flapwise aerodynamic damping values in its effective direction of vibration.

The transformation matrix is as follows:

$$\begin{bmatrix} c_{xx}^{B} & c_{xy}^{B} \\ c_{yx}^{B} & c_{yy}^{B} \end{bmatrix} = \begin{bmatrix} \cos\theta_{sp} & \sin\theta_{sp} \\ -\sin\theta_{sp} & \cos\theta_{sp} \end{bmatrix} \begin{bmatrix} c_{xx}^{R} & c_{xy}^{R} \\ c_{yx}^{R} & c_{yy}^{R} \end{bmatrix} \begin{bmatrix} \cos\theta_{sp} & -\sin\theta_{sp} \\ \sin\theta_{sp} & \cos\theta_{sp} \end{bmatrix} \quad \text{Eqn 2.17}$$

The edgewise and flapwise aerodynamic damping values are then respectively worked out to be:

$$c_{xx}{}^{B} = \cos^2\theta_{sp} c_{xx}{}^{R} + \sin^2\theta_{sp} c_{yy}{}^{R} + \sin\theta_{sp}\cos\theta_{sp}\left(c_{xy}{}^{R} + c_{yx}{}^{R}\right) \quad \text{Eqn 2.18}$$

$$c_{yy}{}^{B} = \sin^2\theta_{sp} c_{xx}{}^{R} + \cos^2\theta_{sp} c_{yy}{}^{R} - \sin\theta_{sp}\cos\theta_{sp}\left(c_{xy}{}^{R} + c_{yx}{}^{R}\right) \quad \text{Eqn 2.19}$$

2.2 State of the art on idling instabilities

This section of the chapter aims to detail the key literature that the thesis aims to build upon.

In 2007, the National Renewable Energy Laboratory (NREL) in the United States of America published a paper titled 'Aeroelastic Instabilities of Large Offshore and Onshore Wind Turbines' (Bir & Jonkman, 2007). In this paper, exploratory studies as well as numerical simulations of a 5MW reference wind turbine, also developed by NREL were performed. The numerical simulations were performed using the aeroelastic analysis tool FAST (Zandt, 2007) coupled with AeroDyn (Moriarty & Hansen, 2005). The loads used in the simulations were taken from the parked wind turbine design load cases as stipulated by edition 3 of The International Electrotechnical Committee's (IEC) document 61400-1 (International Eletrotechnical Commision, 2005). Eigenanalysis was performed after linearizing each simulation at different nacelle yaw angles about their mean rotor azimuth, or after multi blade coordinate transformation was done if the turbine was seen to be idling, to determine the flapwise and edgewise damping values. The results revealed that at certain yaw angles, the edgewise modes were negatively damped. This is, to the knowledge of the author, the first paper that would highlight the potential problem of idling instabilities in larger wind turbines and their sensitivity to nacelle yaw angles as well as rotor azimuths.

The next work would analyse parked turbine blades. Published in 2009, the paper is titled 'Stability analysis of parked wind turbine blades' (Politis & Chaviaropoulos, 2009). Led by Gamesa in Spain, numerical simulations were performed for a parked reference blade of 40m (designed within the framework of Work Package 1B1 of the UpWind project) using both quasi steady aerodynamics as well as unsteady aerodynamics (dynamic stall model), within a limited range of angle of attack from -15° to 30° using the ONERA model (as beyond this range, the dynamic stall model is not validated). This paper aimed to explore how the damping

characteristics would behave when dynamic stall was employed. However to that end, there were limitations in the analyses where the calculations were only valid in a small range of nacelle yaw and the blade was not allowed to idle. Still, the results from both quasi steady as well as unsteady aerodynamics seem to be in rather good agreement with NREL's paper by qualitatively show that idling instabilities seem to be a concern for larger wind turbines in certain yaw angles.

While these first two papers served to establish the possibility of idling instabilities occurring in larger wind turbines, Skrzypiński and his team at the Technical University of Denmark (DTU), was interested in finding the potential cause of such instabilities in their publication 'Self-induced vibrations of a DU96-W-180 airfoil in stall' (Skrzypiński, Gaunaa, Sørensen, Zahle, & Heinz, 2014) by more accurately modelling the airflow in deep stall for a 2D airfoil. To that end, they would first derive an analytical solution for the aerodynamic damping of a DU96-W-180 airfoil to determine the range of angle of attack where idling instabilities due to stall induced vibrations are the most pronounced. From the results of the analytical solution, detailed 2D Reynolds Averaged Navier Stokes (RANS) and 3D Detached Eddy Simulations (DES) solutions were performed at chosen angle of attack values of 24° and 26°. The conclusions drawn from the 3D DES simulations found that stall induced vibrations were not as likely to occur in real life as, from the calculations, for a blade chord of 2m and a 1st edgewise frequency of 1Hz, the wind speed would have to be in excess of 88m/s to observe stall induced vibrations (SIVs). The paper found that the frequency of the stationary vortex shedding was close to the 1st edgewise frequency and hence suggested that vortex induced vibrations (VIVs) are a more likely cause of idling instabilities. However, the results from the 2D RANS drew an almost opposite conclusion suggesting that SIVs were still very much a possibility. Since this paper is the only one that has been found to attempt to more accurately model the airflow around an airfoil in relatively high angles of attack and also noting that the simulations presented therein were only for a single airfoil type, angle of attack and direction of rectilinear vibration, the results must be investigated further in order to be more definitive. Such analyses however lies outside the scope of this thesis and regardless, the results do show that idling instabilities are once again likely to be seen in real life.

The latest paper that was found dealing with the topic of aeroelasticity in idling wind turbines was published in 2016 in a joint effort between Huazhong University of Science and Technology and the National Technical University of Athens titled 'Aeroelastic Stability of Idling Wind Turbines' (Wang, Riziotis, & Voutsinas, 2016). In this paper, the goal was to ascertain if linear eigenvalue stability tools are able to accurately represent the aerodynamic damping values of wind turbines in idling. First, non-linear analysis to determine the stability of the DTU 10MW reference wind turbine in slow idling was assessed between yaw angles of -60° and 60° using the aeroelastic tool hGAST (Manolas, Riziotis, & Voutsinas, 2016) (as this is the range where their dynamic stall model is valid). After identifying the yaw angles that would induce the greatest instabilities, eigenvalue analyses were performed using GAST_lin (Riziotis et al., 2004). The eigenvalue analyses were then compared against the power spectral density (PSD) plots of the time domain analyses. The results seem to agree fairly well, where the lowest

damping values calculated were found in the edgewise modes and the frequencies of these edgewise modes corresponded to peaks in the PSD plots. Finally, aerodynamic work computations were performed in order to further verify the results from the eigenvalue analyses. Forced harmonic oscillations corresponding to the shape and frequency of the turbine modes were imposed onto the blades and the work done was extracted. Qualitative comparisons between the work computations as well as the eigenvalue analyses yielded good agreements.

The four papers discussed present a rather persuasive case for the plausibility of idling instabilities to occur in larger wind turbines. However, there are still many aspects that can be explored that will aid in further understanding of such instabilities. The proposed thesis aims to contribute to the body of knowledge in a small area by exploring what effect changing the angle of attack of the blades may have in terms of mitigating idling instabilities in larger wind turbines.

2.3 Dynamic Stall

In the later portions of the simulations performed in this thesis, unsteady aerodynamics will be implemented through the use of a dynamic stall model. Unlike in quasi steady aerodynamics where once an airfoil exceeds the maximum lift coefficient it immediately enters into stall, the dynamic stall phenomena takes into account the time dependency for an airfoil to fully enter into stall as the vortex causing flow separation travels from the leading edge to the trailing edge. As such, this results in a hysteresis or lag effect where the airfoil stalls at a lift coefficient and angle of attack higher than in the quasi steady case.

According to (McCroskey, 1981), the entire phenomenon can be separated into 6 points seen in Fig [2.2].

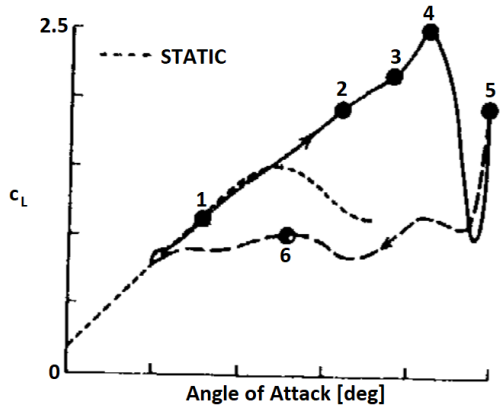

Figure 2.2: The effect of dynamic stall on the lift coefficient on an airfoil taken from (McCroskey, 1981)

Starting from attached flow at point 1, the onset of stall starts at point 2 where a leading edge vortex is created causing a reversal in the airflow. This leading edge vortex moves along the suction side of the airfoil past the mid chord at point 3 and reaches the trailing edge at point 4 after which there is a sudden drop in the lift coefficient as the airflow is fully seperated. Point 5 is due to secondary vortices contributing to a fluctuation in the loads. It can be seen that these

occur at levels lower than the maximum lift coefficient at point 4. As the angle of attack is reduced, point 6, the flow eventually reattaches and follows the linear portion of the AoA vs Cl curve (quasi steady aerodynamics).

There are several engineering models that have been developed to replicate the dynamic stall effect so that they may be applied in aeroelastic load calculations. The basis of the model that is implemented in the aeroelastic tool that will be used in this thesis, Focus 6, Phatas is from (Snel, 1997).

Snel's dynamic stall model

The semi empirical model was formulated based on the results from experiments conducted by the Ohio State University (OSU) in 1994 on two of the three airfoil types tested, the NACA 4415 and the S809 airfoil. The chord length of the airfoils tested was 0.457m in a wind tunnel with wind speeds of around 37 to 42ms^{-1} with a Reynolds number of 1.2x10^{6} at reduced (pitching) frequencies, k, of about 0.022, 0.044 and 0.066. The results of the lift coefficients against the angle of attack for different k values are shown in Fig [2.3].

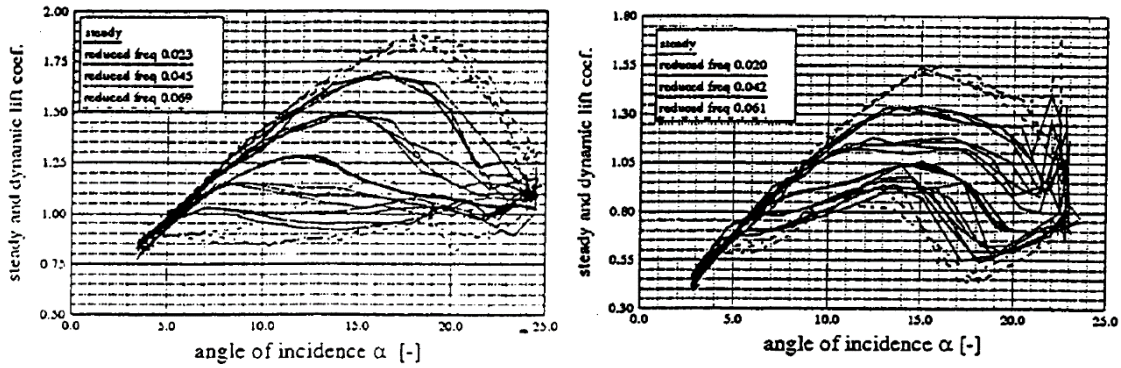

Figure 2.3: Dynamic stall loops of a) NACA 4415 and b) S809 airfoils taken from OSU experiments as presented in (Snel, 1997)

The basis of the model was to define a formulation for the dynamic lift coefficient based on (V.K.Truong, 1993) who suggested that it is the sum of the forcing frequency response, made up of the static Cl and a change in the steady state, as well as higher frequency dynamics as shown in Eqn [2.20].

$$\mathrm{cl}_{\mathrm{dyn}} = cl_{steady} + \Delta cl_1 + \Delta cl_2 \qquad \textbf{Eqn 2.20}$$

For Δcl_1, the "simple" model as an initial point where a first order Ordinary Differential Equation (ODE) is used following the form:

$$\tau \frac{d\Delta cl_1}{dt} + cf_{10}\Delta cl_1 = ft_1 \qquad \textbf{Eqn 2.21}$$

In Eqn [2.21] Δcl_1 follows the frequency of the forcing term, ft_1. The coefficient of the time derivative of Δcl_1, τ, is taken to be the length of the chord divided by two times of the wind speed, c/2U. The forcing term in turn is expressed as the time derivative of Δcl_{pot} which is the

difference between the potential flow lift coefficient and the steady lift coefficient shown in Eqn [2.22].

$$\Delta cl_{pot} = cl_{pot} - cl_{steady} = 2\pi \sin(\alpha - \alpha_0) - cl_{steady} \quad \text{Eqn 2.22}$$

Finally, the coefficient cf_{10} is seen to act as a spring to reduce Δcl_1 to zero when there is no forcing. From the "simple" model, it is shown that this coefficient is higher when $d\alpha/dt$ is negative and when α is increasing. This is expressed in the model as:

$$cf_{10} = \frac{1 + 0.5\Delta cl_{pot}}{1 + 60\pi\left(d\alpha/_{dt}\right)} \quad \text{Eqn 2.23}$$

The term Δcl_2 is expressed as a second order ODE as follows:

$$\tau^2 \frac{d^2\Delta cl_2}{dt^2} + cf_{21}\frac{d\Delta cl_2}{dt} + cf_{20}\Delta cl_2 = ft_2 \quad \text{Eqn 2.24}$$

The coefficients were obtained through experimentation as well as with comparisons against the OSU measurements and were determined to be:

$$cf_{20} = {k_s}^2[1 + 3(\Delta cl_2)^2]\left[1 + 3\left(d\alpha/_{dt}\right)^2\right] \quad \text{Eqn 2.25}$$

$$cf_{21} = \begin{cases} 60\tau k_s\left[-0.01\left(\Delta cl_{pot} - 0.5\right) + 2(\Delta cl_2)^2\right] & if\ \left(d\alpha/_{dt} \geq 0\right) \\ 2\tau k_s & if\ \left(d\alpha/_{dt} < 0\right) \end{cases} \quad \text{Eqn 2.26}$$

Where k_s is the basis reduced Strouhal frequency chosen to be 0.2.

The forcing term was also determined after many iterations and is expressed as:

$$ft_2 = 0.12\left(-0.15\Delta cl_{pot} + 0.05\frac{d\Delta cl_{pot}}{dt}\right) \quad \text{Eqn 2.27}$$

The following figure shows an example of the dynamic stall loops as modelled by another dynamic stall model, the Beddoes-Lieshman model following the method detailed in (Morten Hartvig Hansen, Gaunaa, & Madsen, 2004) by modelling the dynamic stall phenomemon in 4 steps.

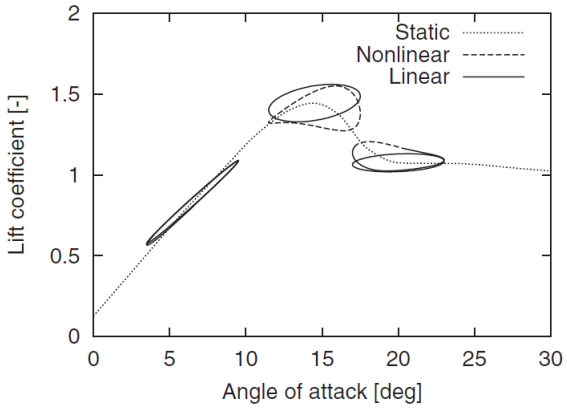

Figure 2.4: Linear and nonlinear unsteady lift coefficients plotted against AoA taken from (M. H. Hansen, 2004) with model parameters and reduced frequencies typical for wind turbine blades

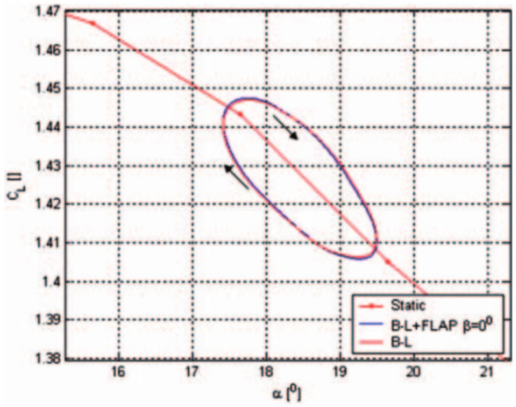

Figure 2.5: Dynamic stall loop of an airfoil shown in pink with arrows denoting the direction of the loops taken from (Andersen, Gaunaa, Bak, & Hansen, 2009)

Fig [2.5] shows another example of a dynamic stall loop of an airfoil calculated once again using the Beddoes-Leishman model detailed in (Morten Hartvig Hansen et al., 2004) with a reduced frequency of 0.15. Fig [2.5] was presented in order to show that the direction of the loop, denoted by the arrows, is in the clockwise direction.

3. Analytical Equations for Aerodynamic Damping of a Parked Turbine Blade

In order to define a theoretical basis from which to build upon in the later portions of this thesis, analytical equations for the aerodynamic damping values were derived for a wind turbine blade section.

The equations derived in this chapter were adapted from Petersen's equations for the local aerodynamic damping of a wind turbine blade section (detailed in chapter 2.1) and were formulated in a way where it was possible to observe how varying the nacelle yaw angle, rotor azimuth as well as pitch would affect the aerodynamic damping values of a blade section.

3.1 Methodology to adapt Petersen's equations from rotating to parked blade

Easily, one of the more important and larger aspects in adapting the equations is to understand how the velocity components will change for a parked blade and subsequently how these changes will affect Petersen's equations for the aerodynamic damping in the rotor coordinate system. Even though rΩ is zero because the blade is at standstill it does not mean that the in plane velocity seen by the blade is zero.

The figure below shows how the velocity components are expressed when changing from a rotating blade to one at standstill at a representative position with a rotor azimuth of 0° (blade at 12 O'clock), a (nacelle) yaw angle of -30° and blade pitch of 90°.

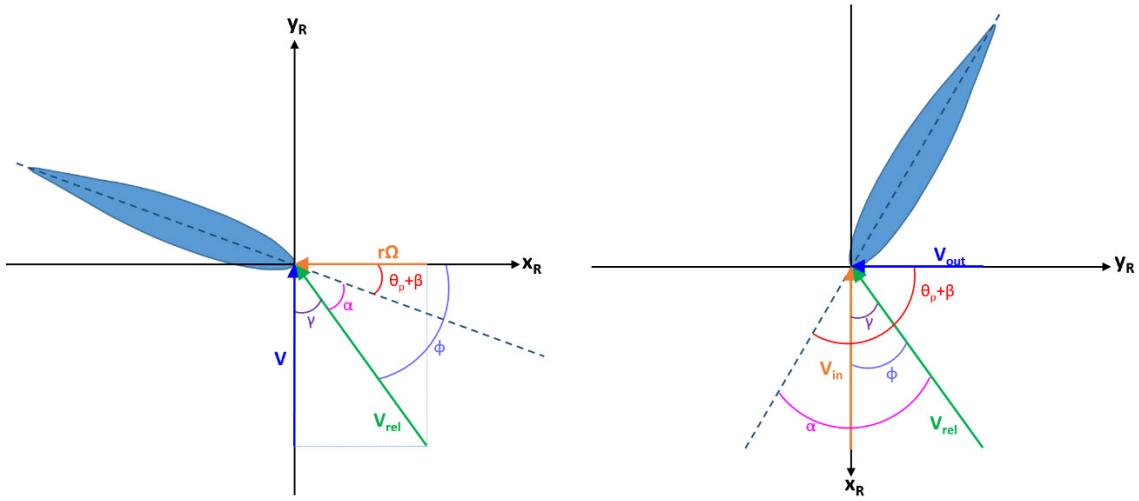

Figure 3.1: Velocity triangle of a blade section a) that is rotating b) at standstill

From Fig [3.1] it can be seen that for a blade at standstill, rΩ and V are now expressed in terms of an in plane and out of plane velocity, V_{in} and V_{out} respectively. Fig [3.1b] also shows how the axes have been swapped. This is due to the pitching of the blade section at 90°. The rationale for this as well as a more detailed explanation as to how the velocity triangle is affected by the pitch of a blade will be discussed further in section 3.4.

However for now, from Fig [3.1b], it can be seen that

$$\mathrm{V_{rel}} = \sqrt{V_{in}^2 + V_{out}^2} \qquad \text{Eqn 3.1}$$

$$\cos\phi = \frac{V_{in}}{V_{rel}} \qquad \text{Eqn 3.2}$$

$$\sin\phi = \frac{V_{out}}{V_{rel}} \qquad \text{Eqn 3.3}$$

$$\partial\alpha = \partial \sin^{-1}\frac{V_{out}}{V_{rel}} \qquad \text{Eqn 3.4}$$

Applying this to Petersen's equation for projecting the normal and tangential forces along the transformation angle φ (rewritten again for convenience),

$$\begin{Bmatrix} {F_x}^R \\ {F_y}^R \end{Bmatrix} = \begin{bmatrix} \sin\phi & -\cos\phi \\ \cos\phi & \sin\phi \end{bmatrix} \begin{Bmatrix} dL \\ dD \end{Bmatrix} \quad \text{Eqn 3.5}$$

The aerodynamic damping equations along the newly defined rotor coordinate system can then be worked out to give:

$${c_{xx}}^R = \frac{1}{2} c\rho \frac{V_{in}}{\mathrm{w}} \left[\left(\frac{2{V_{in}}^2 + {V_{out}}^2}{V_{in}} \right) C_d - V_{out} C_{d_\alpha} - V_{out} C_l + \frac{{V_{out}}^2}{V_{in}} C_{l_\alpha} \right] \quad \text{Eqn 3.6}$$

$${c_{yy}}^R = \frac{1}{2} c\rho \frac{V_{in}}{\mathrm{w}} \left[\left(\frac{2{V_{out}}^2 + {V_{in}}^2}{V_{in}} \right) C_d + V_{out} C_{d_\alpha} + V_{out} C_l + V_{in} C_{l_\alpha} \right] \quad \text{Eqn 3.7}$$

$${c_{xy}}^R = \frac{1}{2} c\rho \frac{V_{in}}{\mathrm{w}} \left[\left(\frac{2{V_{out}}^2 + {V_{in}}^2}{V_{in}} \right) C_l + V_{out} C_{l_\alpha} - V_{out} C_d - V_{in} C_{d_\alpha} \right] \quad \text{Eqn 3.8}$$

$${c_{yx}}^R = \frac{1}{2} c\rho \frac{V_{in}}{\mathrm{w}} \left[\left(\frac{2{V_{in}}^2 + {V_{out}}^2}{V_{in}} \right) C_l + V_{out} C_{d_\alpha} - V_{out} C_l + \frac{{V_{out}}^2}{V_{in}} C_{d_\alpha} \right] \quad \text{Eqn 3.9}$$

These aerodynamic equations are then used to determine the in plane and out of plane aerodynamic damping values in the rotor plane.

However, since this thesis looks at a wide range of pitch and yaw angles, looking at the aerodynamic damping values along the rotor coordinate system might not give the most representative results as, at certain pitch angles, the main direction of vibration may be very far off from vibrating along the x and y directions and as such, the aerodynamic damping values along the rotor coordinate system maybe not be reflective of what will be seen in a realistic mode shape.

Hence, it would be more useful to align the aerodynamic damping values in the rotor plane along the chord direction. This can be done by using the same transformation matrix previously used in Petersen's equations to determine the edgewise and flapwise aerodynamic damping values, Eqn [2.17].

Looking back again at Fig [3.1b], because the pitch angle is 90°, in order to align the aerodynamic damping equations along the blade chord, one has to simply transform the equations about the twist angle, β. As such, the chordwise and flatwise aerodynamic damping values aligned along the chord direction can be determined from the following equations.

$$\mathrm{c}_{\mathrm{chordwise}} = \cos^2\beta {c_{xx}}^R + \sin^2\beta {c_{yy}}^R + \sin\beta\cos\beta \left({c_{xy}}^R + {c_{yx}}^R \right) \quad \text{Eqn 3.10}$$

$$\mathrm{c}_{\mathrm{flatwise}} = \sin^2\beta {c_{xx}}^R + \cos^2\beta {c_{yy}}^R - \sin\beta\cos\beta \left({c_{xy}}^R + {c_{yx}}^R \right) \quad \text{Eqn 3.11}$$

Similarly, if the structural pitch angle is known, it can be added to the equations to give the edgewise and flapwise aerodynamic damping values in the direction of vibration of the blade from the following equations.

$$c_{\text{edgewise}} = \cos^2(\theta_{sp}+\beta){c_{xx}}^R + \sin^2(\theta_{sp}+\beta){c_{yy}}^R + \sin(\theta_{sp}+\beta)\cos(\theta_{sp}+\beta)\left({c_{xy}}^R + {c_{yx}}^R\right) \quad \text{Eqn 3.12}$$

$$c_{\text{flapwise}} = \sin^2(\theta_{sp}+\beta){c_{xx}}^R + \cos^2(\theta_{sp}+\beta){c_{yy}}^R - \sin(\theta_{sp}+\beta)\cos(\theta_{sp}+\beta)\left({c_{xy}}^R + {c_{yx}}^R\right) \quad \text{Eqn 3.13}$$

These equations will be revisited again for a case where the pitch angle is varied.

Next, in order to account for the effects that varying the yaw angle, rotor azimuth as well as blade pitch angle have on the aerodynamic damping values, one must determine how these parameters define the local angle of attack. The following sections detail how the chordwise, flatwise, edgewise and flapwise aerodynamic damping values are determined from varying each parameter and presents the respective aerodynamic damping values within a specified range of values.

3.2 Analytical aerodynamic damping values at varying nacelle yaw angles

The first parameter to look at is the effect of varying the nacelle yaw angle. The sign convention used to define the yaw angle follows that used in Focus 6, Phatas as shown in the following figure.

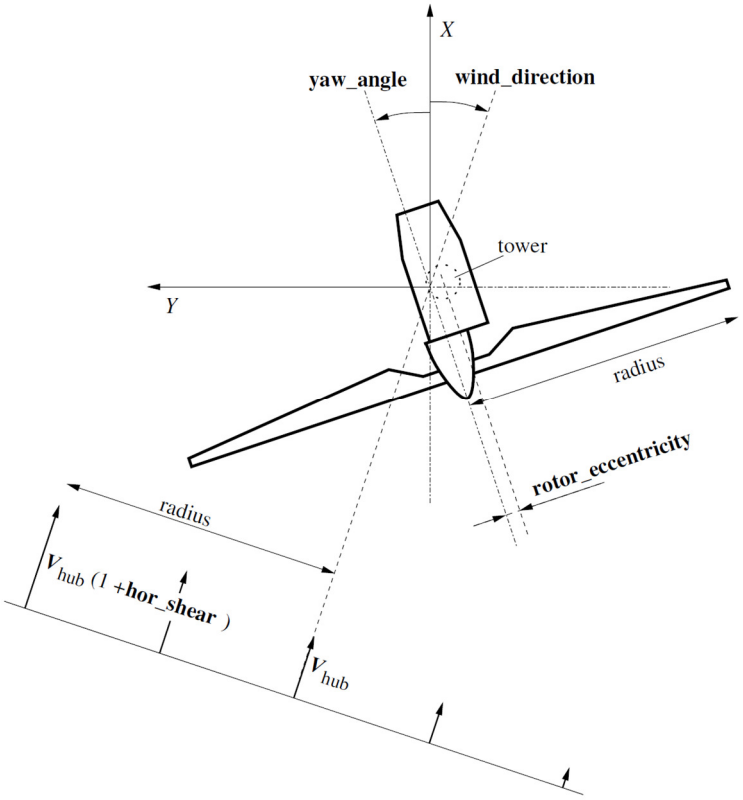

Figure 3.2: Orientation of a wind turbine with respect to the wind loading (Lindenburg, 2014)

For this study, the blade section was pitched at an angle of 90° at a rotor azimuth of 0° (12 o'clock position) with the yaw angle varying from -170° to 170°. The following figure shows the velocity triangle with a positive and negative yaw.

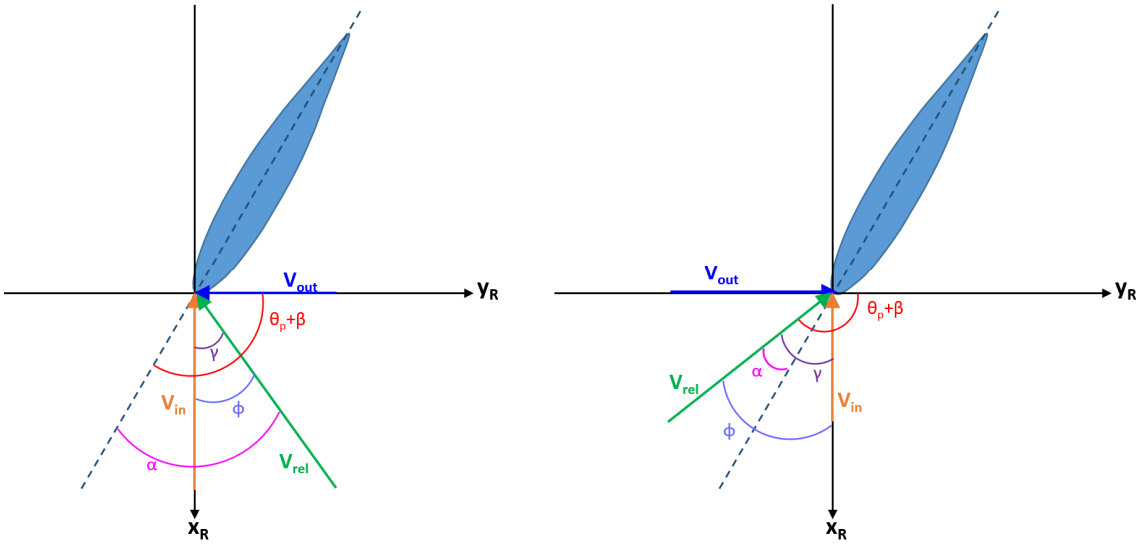

Figure 3.3: Velocity triangle of a blade section pitched at 90°, 0° rotor azimuth and a) a negative yaw angle and b) a positive yaw angle

From Fig [3.3] there are a couple of things to take notice of. Firstly, once again how the axes are defined is of importance. It can also be observed that the transformation angle, ϕ, is defined as the angle between the x axis and the incoming wind. Doing so ensures that Eqns [3.2] and [3.3] remain valid. Eqn [3.4] also remains valid for this particular case where the pitch is 90°. This will be explained in section 3.4 where the effects on the velocity triangle from a varying pitch angle are discussed.

As such, by correctly defining γ, ϕ and α, Eqns [3.6] to [3.13] remain valid and can be used as is without further modifications to determine the aerodynamic damping values. Looking at Fig [3.3] once more, it can be seen that regardless of the yaw direction, the local angle of attack can be calculated as follows:

$$\alpha = \gamma - \beta \qquad \textbf{Eqn 3.14}$$

After determining the local angle of attack, the aerodynamic damping values according to Eqns [3.10] to [3.13] can be calculated for each yaw angle through the use of a simple MATLAB script which runs according to the following flowchart.

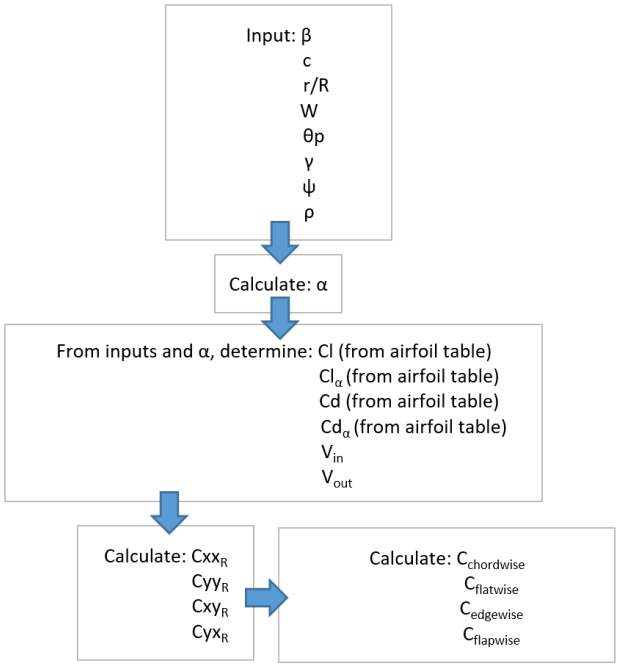

Figure 3.4: General flowchart for generating aerodynamic damping values for different parameters in MATLAB

For a blade section of the NREL 5MW ref wind turbine at r/R=0.75 in standstill with the above parameters with an incoming wind speed of 50ms^{-1} and a yaw angle ranging from -170° to 170°, the chordwise and flatwise aerodynamic damping values aligned along the chord direction for all three blades are shown in the following figures by setting the structural pitch angle to zero.

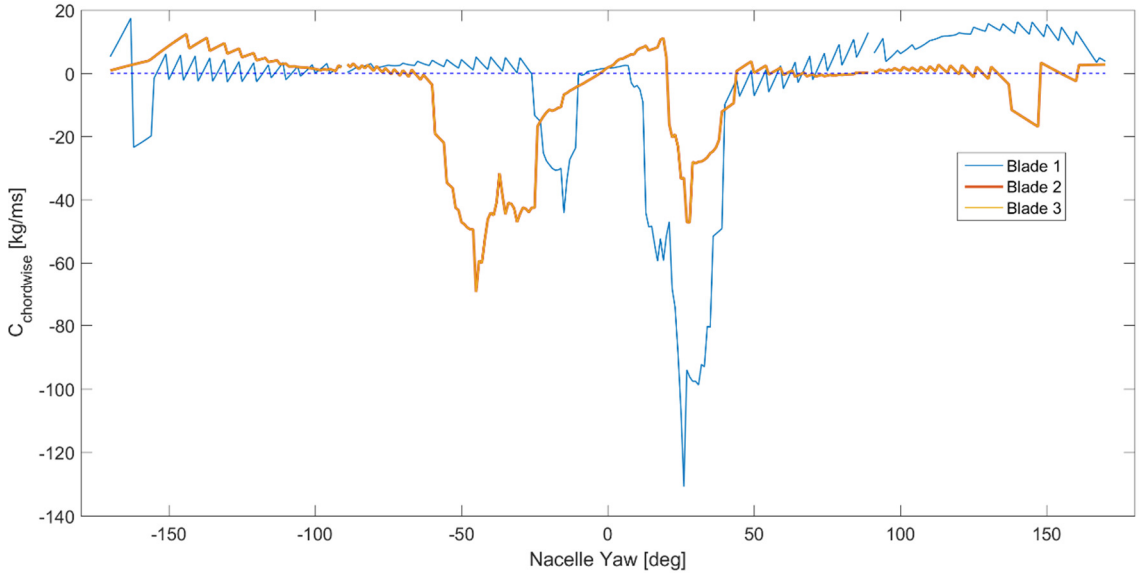

Figure 3.5: Chordwise aerodynamic damping values aligned along the chord direction for all three blades at different yaw angles

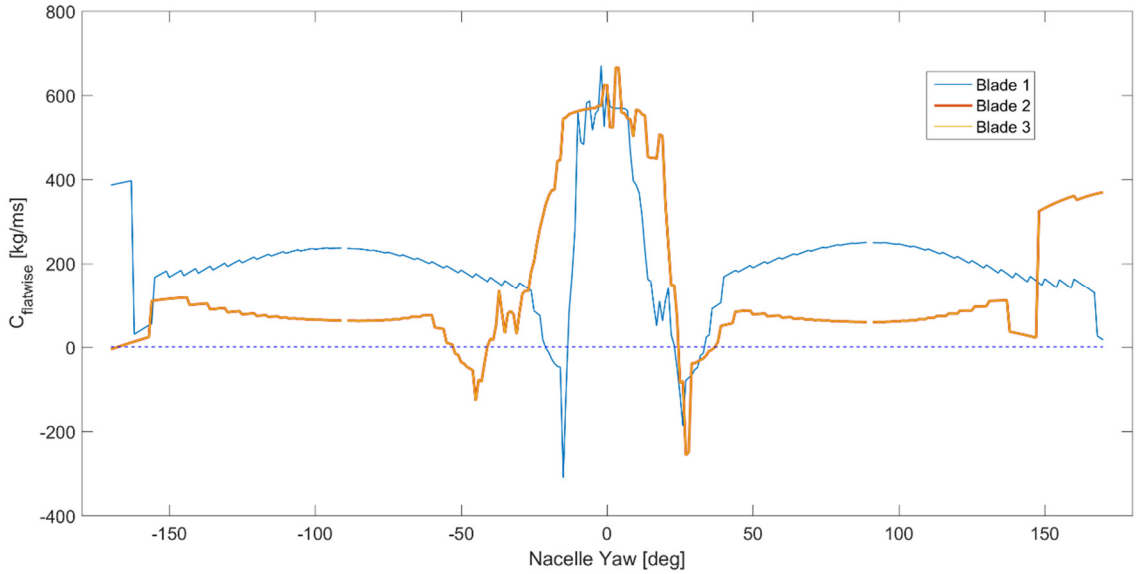

Figure 3.6: Flatwise aerodynamic damping values aligned along the chord direction for all three blades at different yaw angles

The aerodynamic damping values for blades 2 and 3 were obtained through the use of a transformation matrix for rotor azimuths of 120° and 240° respectively (this will be explained in greater detail in the following section).

Before moving on into a detailed look at the results, it is of importance to be able to validate the method used to obtain the aerodynamic damping values above with results from existing literature as the same method will be used throughout the rest of this chapter.

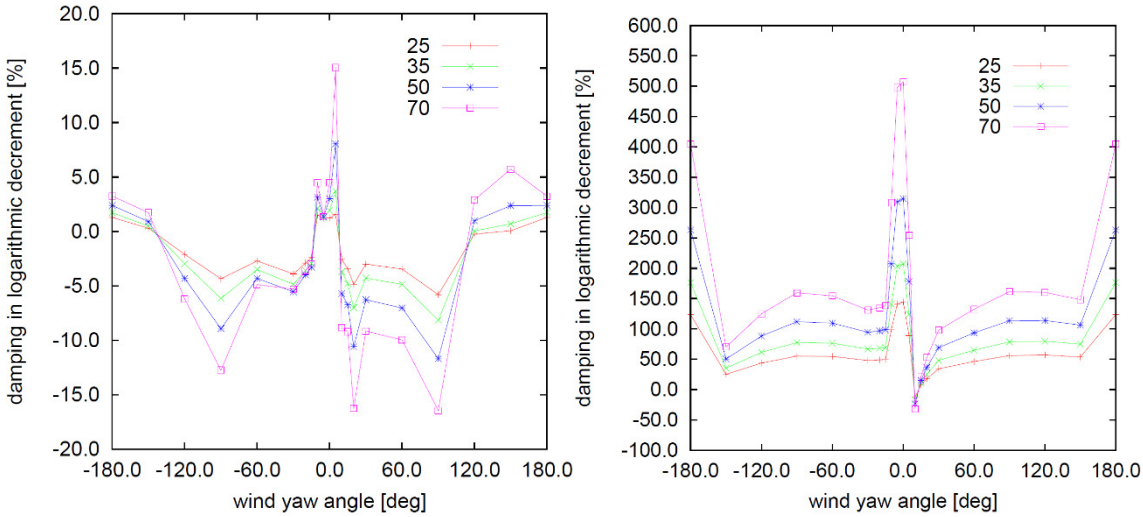

Figure 3.7: a) First edgewise and b) first flapwise aerodynamic damping in logarithmic decrement of a parked blade at 0° rotor azimuth, 90° blade pitch, varying wind yaw angles and varying wind speeds of 25ms^{-1}, 35ms^{-1}, 50ms^{-1} and 70ms^{-1} as taken from figure 6, chapter 4.1 of (Politis & Chaviaropoulos, 2009).

Figs [3.5] and [3.6] can be compared to the first flapwise and edgewise results of the 40m blade designed in the Upwind project which was also analysed at 0° rotor azimuth and a blade pitch angle of 90° at varying yaw angles and zero structural damping detailed in (Politis & Chaviaropoulos, 2009) and reproduced in Fig [3.7]. Because the geometry of the blades to be compared as well as the calculation of the aerodynamic damping values are different, only a qualitative comparison can be made.

Comparing the flatwise aerodynamic damping values obtained in this report against the first flapwise aerodynamic damping values obtained by Politis and Chaviaropoulos, it can be seen that the trends in both results are very similar. The aerodynamic damping values in both cases are largely positive except for a very small region near zero yaw where there is a dip and negative damping values are obtained. The results from this thesis also shows a dip in the negative yaw angle which is not seen in Politis' and Chaviaropoulos' paper. This could be due to the resolution used to obtain their results and is not seen as a critical difference resulting from the use of either method.

Similarly, the trends in the results between the chordwise aerodynamic damping values obtained in this report and the first edgewise aerodynamic damping values obtained by Politis and Chaviaropoulos are in generally good agreement with each other. In both cases, there is a small region near zero yaw where positive aerodynamic damping values are seen and enter negative values moving outwards. However, from the results in this thesis, the aerodynamic damping values are seen to recover back to the positive region earlier than shown in the results obtained by Politis and Chaviaropoulos.

Noting once again that it is not possible to obtain exactly the same results and from assessing the similarities in the trends, it was deemed that the results obtained through the method described earlier in this chapter have been correctly determined.

Moving on into a more detailed look at the results obtain in this chapter, Fig [3.5] shows that the lowest chordwise damping value for blade 1 occurs at yaw angles of -15° and 26°. There is also a small region of positive damping between -7° and 7° yaw. From yaw angles of -26° and 44° moving outwards towards -170° and 170°, the chordwise aerodynamic damping is seen to be marginally positive or negative although from positive yaw angles of 74° onwards, the aerodynamic damping values are constantly positive.

For blades 2 and 3, a similar trend is seen. However, the minimum damping peaks have been shifted to -45° and 28° yaw angle. The range with positive chordwise aerodynamic damping near zero yaw is also different and is now between -2° and 20°. The regions where marginal positive and negative chordwise aerodynamic damping are seen now start from -63° and 44°. However, for blades 2 and 3, from -76° onwards, it can be seen that the aerodynamic damping values are constantly positive.

Looking at the flatwise aerodynamic damping values in Fig [3.6], it can be seen that the minimum damping values occur at the same yaw angles as Fig [3.5]. It can also be seen that negative damping values are only observed in a small range of yaw angles near the minimum aerodynamic damping values, with a spread of about +/- 3.5° to 6°.

By including a structural pitch angle, the edgewise aerodynamic damping values can be determined. The edgewise aerodynamic damping values of blade 1 for different structural pitch angles is shown in the following figure.

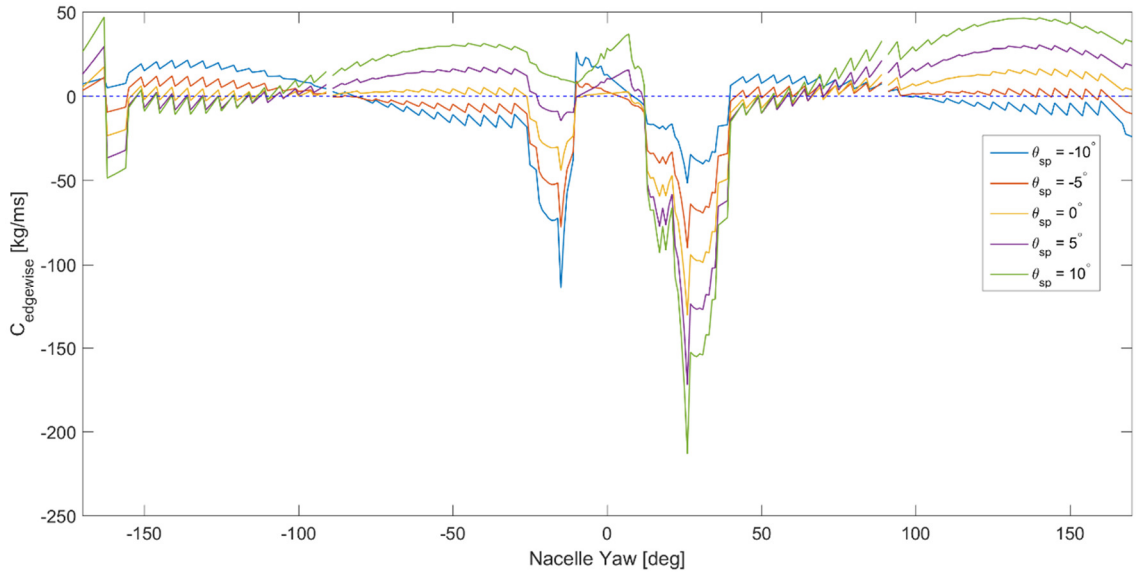

Figure 3.8: Edgewise aerodynamic damping values of blade 1 aligned along the blade chord direction at different yaw angles over several structural pitch angles

In looking at Fig [3.8], increasing the structural pitch angle is seen to increase the severity of the minimum damping value but does not shift the point where the minimum damping is seen. Between a yaw angle of -10° and 12°, it can be seen that for positive structural pitch angles the aerodynamic damping is higher for positive yaw angles. The opposite is true for negative structural pitch angles. From yaw angles of -26° and 40° moving outwards, it can now be seen that the structural pitch angle greatly affects the aerodynamic damping values.

Based on the observations made in the above plots, apart from very small angles close to zero yaw, nacelle yaw greatly affects the aerodynamic damping of the wind turbine blades. For larger yaw angles, structural pitch angles may play an important role in determining the regions where the wind turbine blades would tend to be more stable.

3.3 Analytical aerodynamic damping values at varying rotor azimuths

The second parameter that was looked at was the effect of varying the blade's rotor azimuth. This was also used to determine the aerodynamic damping values of all three blades as mentioned previously.

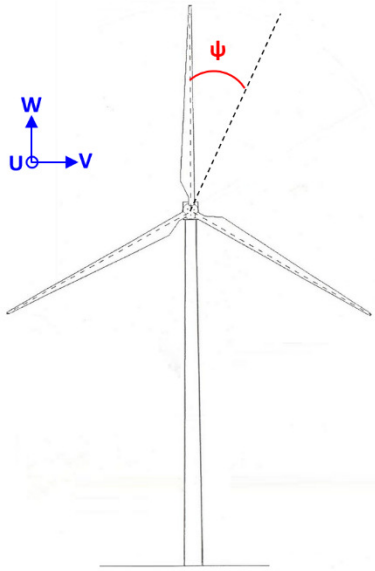

Figure 3.9: Front view of wind turbine with sign convention for positive rotor azimuth and wind components

In order to account for the change in rotor azimuth in Petersen's equations, the wind velocity components must first be transformed from the inertial frame to the rotated blade frame. This is done via a rotation matrix shown in the following equation.

$$(U_{iner} \quad V_{iner} \quad W_{iner}) \begin{bmatrix} 1 & 0 & 0 \\ 0 & \cos\psi & \sin\psi \\ 0 & -\sin\psi & \cos\psi \end{bmatrix} = (U_{rot} \quad V_{rot} \quad W_{rot}) \qquad \text{Eqn 3.15}$$

For a yawed flow assuming blades are pitched at 90° and also assuming that there is no vertical wind component,

$$(U_{iner} \quad V_{iner} \quad W_{iner}) = (\mathrm{V_{rel}} \cos\gamma \quad \mathrm{V_{rel}} \sin\gamma \quad 0) = (V_{in} \quad V_{out} \quad 0) \qquad \text{Eqn 3.16}$$

After transforming the wind components, the local angle of attack can then be determined as shown in the following equation.

$$\alpha = \tan^{-1}\left(\frac{V_{rot}}{U_{rot}}\right) - \beta \qquad \text{Eqn 3.17}$$

Tan^{-1} returns the four quadrant inverse tangent for values between -180° and 180°. It can be seen that this transformation is essentially performing a correction of the yaw angle. After determining the angle of attack, the same flow chart as shown in Fig [3.4] is followed to determine how the chordwise and flatwise aerodynamic damping values of a blade vary over one revolution by setting the structural pitch angle to be zero. Again, by including a structural pitch angle, the edgewise and flapwise (not shown) aerodynamic damping values of blade 1 in the chord direction can be determined over several structural pitch angles. The following figures are for the same blade section used in the previous section, pitched at 90° with an incoming windspeed, V_{rel}, of 50ms^{-1} and a yaw angle of 30°.

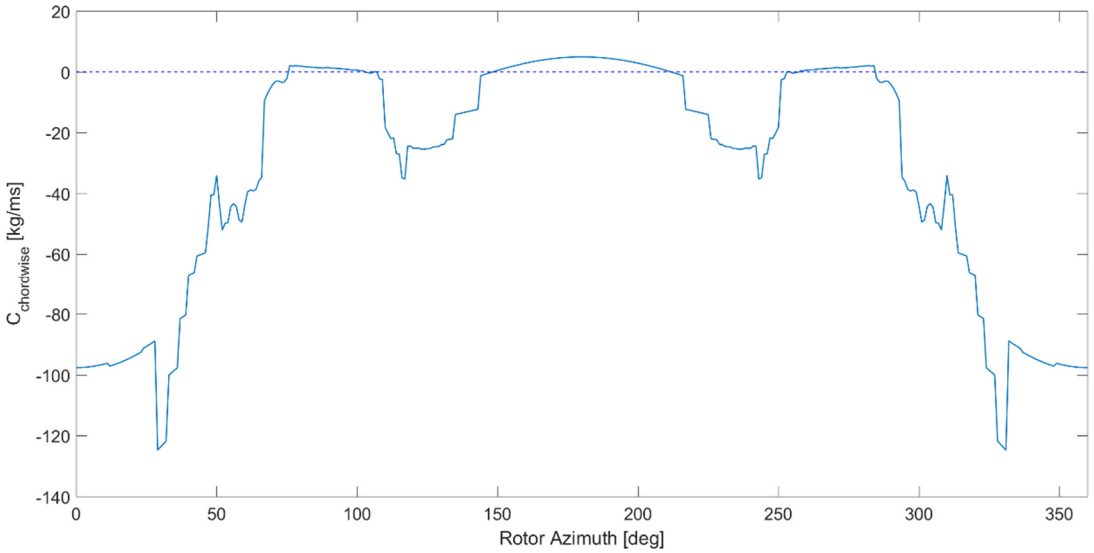

Figure 3.10: Chordwise aerodynamic damping values aligned along chord direction for blade 1 at different rotor azimuths

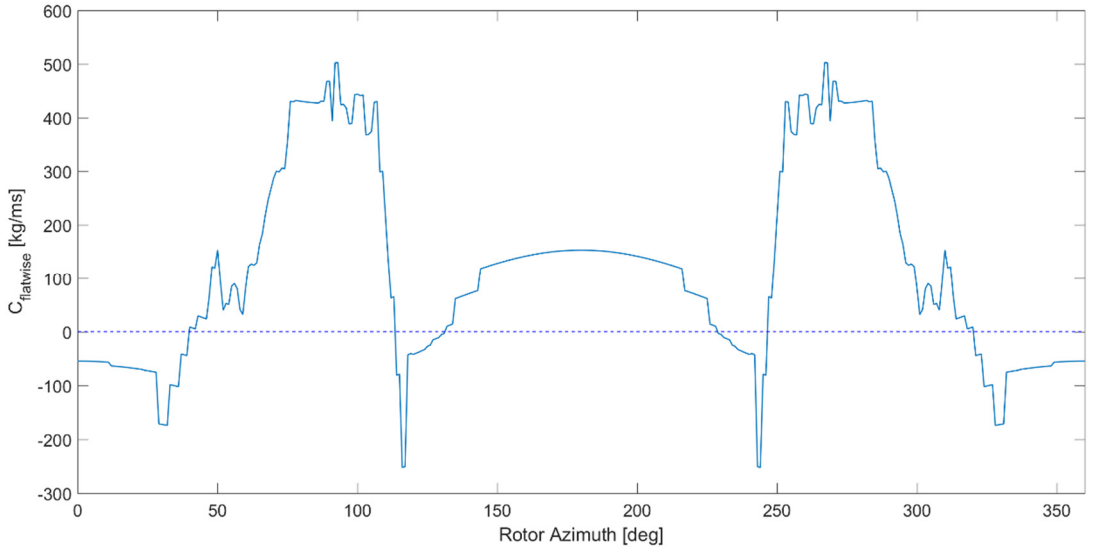

Figure 3.11: Flatwise aerodynamic damping values aligned along chord direction for blade 1 at different rotor azimuths

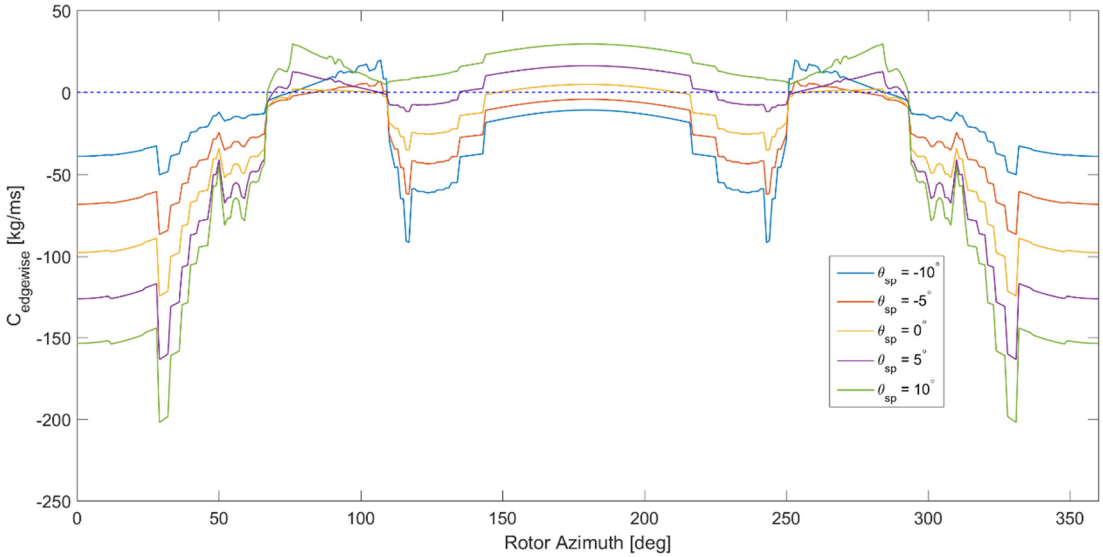

Figure 3.12: Edgewise aerodynamic damping values aligned along chord direction of blade 1 at different rotor azimuths over several structural pitch angles

The chordwise and flatwise aerodynamic damping values are calculated for one blade over a full revolution of 360° as this is the same as calculating the aerodynamic damping values of all three blades over a 120° range of rotor azimuth each.

In looking at the chordwise aerodynamic damping values in Fig [3.10], it can be seen that except for three regions from 76° to 102°, 149° to 211° and 258° to 284° azimuth, the aerodynamic damping values remain largely negative.

Conversely, the flatwise aerodynamic damping values shown in Fig [3.11] are largely positive except for three small regions from 40° to 113°, 132° to 228° and 247° to 320°.

Looking at Fig [3.12], between 67° and 293° azimuth, it can be seen that positive aerodynamic damping values can be achieved by having a large structural pitch angle. Conversely, from 0° to 67° and from 293° to 360° azimuths it is shown that the edgewise instability is made more severe by increasing the structural pitch angle.

From these observations, it can be seen that at such an unstable setting according to the analytical equations and also bearing in mind that each blade operates in an azimuth range of 120 degrees, it may be difficult to vary the azimuth such that at any one time all three blades exhibit a positive edgewise aerodynamic damping.

3.4 Analytical aerodynamic damping values at varying pitch angles

The last parameter explored in this thesis is the effect of varying the blade pitch angle. As mentioned earlier, when varying the pitch angle, of particular importance is to define the axes and transformation angle, ϕ, in such a way as to ensure that Eqns [3.2] and [3.3] remain true.

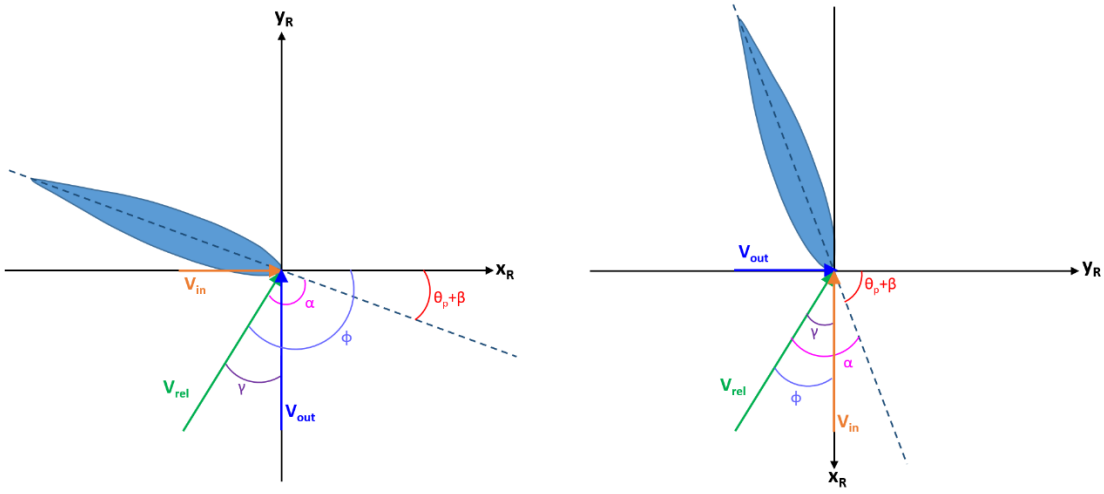

Figure 3.13: Velocity triangle of a blade section at 0° rotor azimuth and 30° yaw angle with a blade pitch angle and twist a) less than 45° b) more than 45°

From Fig [3.13], it can be seen that as the pitch angle and twist of the blade increase from 0° to more than 45° from the horizontal, the axes change in accordance to how V_{in} and V_{out} are defined, where V_{in} is always along the x axis and V_{out} is always along the y axis. Again as stated in section 3.2, the transformation angle, ϕ, is always measured from the x axis. In order for Eqn [3.4] to remain valid, the slope of the angle of attack is always measured against the airfoil aligned along the x axis as well. Finally, it can also be seen that regardless of the pitch angle, for a blade section where the rotor azimuth is 0° and the yaw angle is 30°, the local angle of attack can be determined as follows.

$$\alpha = 90° - (\theta_p + \beta) + \gamma \qquad \textbf{Eqn 3.18}$$

By defining the aforementioned variables, Eqns [3.6] to [3.9] can once again be used as is. However, because of the way the axes definition changes with the pitch, Eqns [3.10] to [3.13] cannot be universally applied to all pitch angles from 0° to 90°.

As such, the approach was taken to go back to Peterson's transformation matrix for aligning the aerodynamic damping equations in the rotor plane about a transformation angle, θ_{RB}, shown in Eqn [2.17] and rewritten here again for convenience.

$$\begin{bmatrix} c_{xx}^B & c_{xy}^B \\ c_{yx}^B & c_{yy}^B \end{bmatrix} = \begin{bmatrix} \cos\theta_{RB} & \sin\theta_{RB} \\ -\sin\theta_{RB} & \cos\theta_{RB} \end{bmatrix} \begin{bmatrix} c_{xx}^R & c_{xy}^R \\ c_{yx}^R & c_{yy}^R \end{bmatrix} \begin{bmatrix} \cos\theta_{RB} & -\sin\theta_{RB} \\ \sin\theta_{RB} & \cos\theta_{RB} \end{bmatrix} \qquad \textbf{Eqn 3.19}$$

Where the sum of the blade pitch angle and the twist is less than 45°, θ_{RB}, is defined as:

$$\theta_{RB} = \theta_{sp} + \theta_p + \beta \qquad \textbf{Eqn 3.20}$$

Where the sum of the blade pitch angle and the twist is greater than 45°, θ_{RB}, is defined as:

$$\theta_{RB} = \theta_{sp} + \theta_p + \beta - 90 \qquad \textbf{Eqn 3.21}$$

After determining θ_{RB}, the edgewise and flapwise aerodynamic damping values can be determined by the following equations:

$$c_{\text{edgewise}} = \cos^2\theta_{RB} {c_{xx}}^R + \sin^2\theta_{RB} {c_{yy}}^R + \sin\theta_{RB}\cos\theta_{RB}\left({c_{xy}}^R + {c_{yx}}^R\right) \quad \text{Eqn 3.22}$$

$$c_{\text{flapwise}} = \sin^2\theta_{RB} {c_{xx}}^R + \cos^2\theta_{RB} {c_{yy}}^R - \sin\theta_{RB}\cos\theta_{RB}\left({c_{xy}}^R + {c_{yx}}^R\right) \quad \text{Eqn 3.23}$$

By using a structural pitch angle of 0°, the respective chordwise and flatwise aerodynamic damping values can also be determined by once again using the same basic script that can be run in MATLAB following the flowchart seen in Fig [3.4].

Again, the chordwise aerodynamic damping values for all three blades at r/R=0.75 with an incoming windspeed, V_{rel}, of 50ms^{-1} is determined by using the method described in section 3.3 at azimuth angles of 120° and 240°.

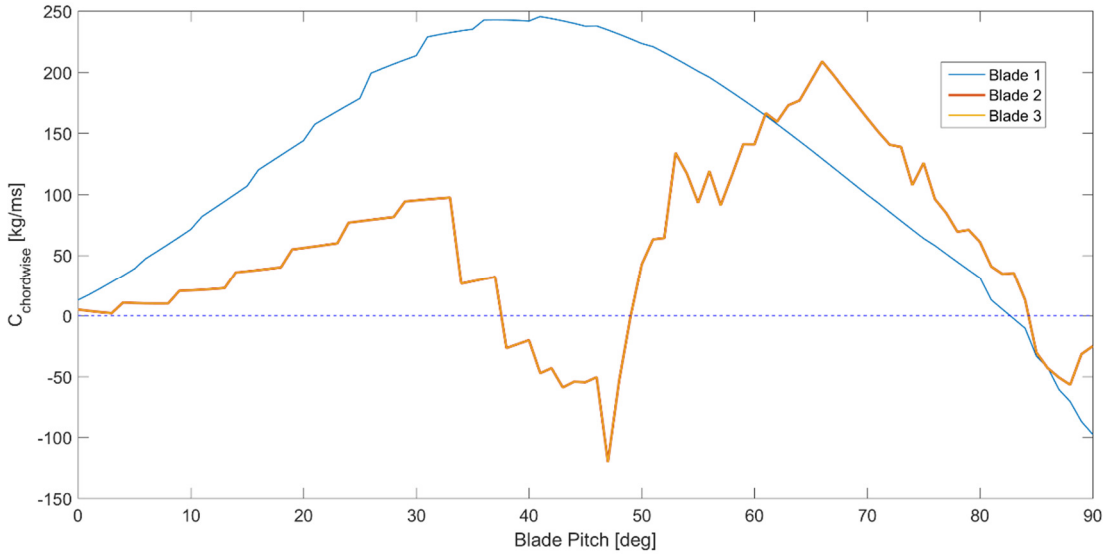

Figure 3.14: Chordwise aerodynamic damping values aligned along chord direction for all three blades at different pitch angles

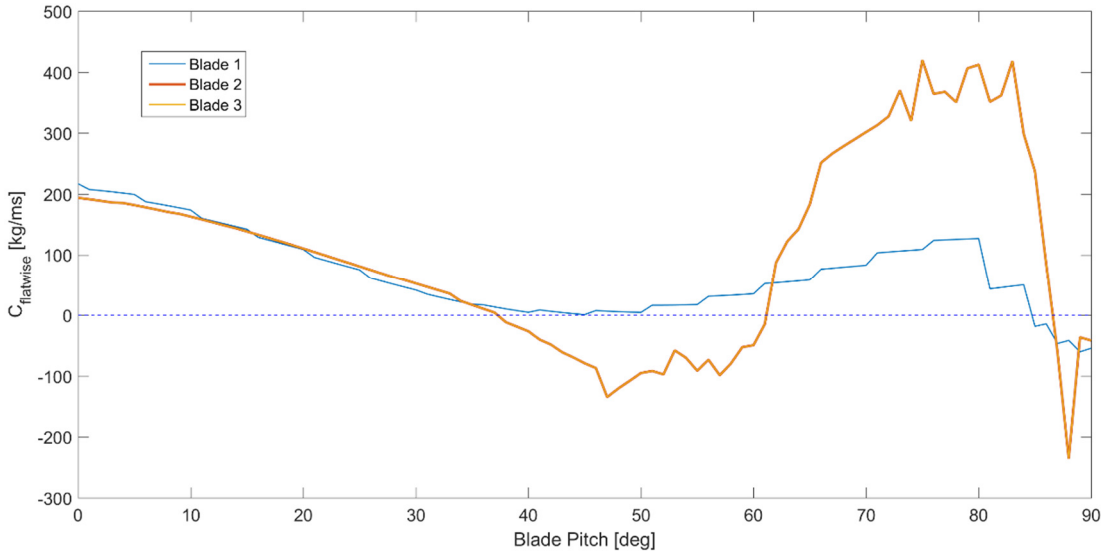

Figure 3.15: Flatwise aerodynamic damping values aligned along chord direction for all three blades at different pitch angles

In looking at Fig [3.14], it can be seen that at up to a certain point, having a blade pitch less than 90° is beneficial in achieving positive aerodynamic damping values for a blade in a parked condition.

For blade 1, starting from a minimum at 90° pitch, the aerodynamic damping values are seen to increase until it peaks at 41° pitch after which the aerodynamic damping values are seen to decline until zero pitch.

For blades 2 and 3 however, it can be observed that after a small dip in the chordwise aerodynamic damping values from 90° to 88° pitch, the aerodynamic damping values steadily increase until the peak value is reached at 66°. From there, a rather sharp decline can be seen until 47° where the aerodynamic damping values are at a minimum. From there, there is an increase again until 33° after which there is a steady decrease until zero pitch, where the aerodynamic damping values are close to blade 1.

The flatwise aerodynamic damping values for all three blades as shown in Fig [3.15] almost follow a similar trend.

For blade 1, it can be seen that the aerodynamic damping values also see it's minimum value at 90° pitch. Again, it increases from there however this time the values start to decrease again much earlier, at 80° pitch. The gradual decline continues all the way until 45° after which it is seen to increase again all the way until zero pitch, where it peaks.

For blades 2 and 3, again, a sharp drop can be seen between 90° and 88° pitch. Again from here, the aerodynamic damping values increase until the peak values are reached between 75° and 83°. From there, the values decline again until the same pitch angle as seen in Fig [3.14] of 47° after which, the values increase all the way until zero pitch where the aerodynamic damping values are once again close to blade 1.

The edgewise aerodynamic damping values aligned along the chord direction for blade 1 is calculated by adding a structural pitch angle. The following figure shows the edgewise aerodynamic damping values for several structural pitch angles plotted against varying blade pitch angles.

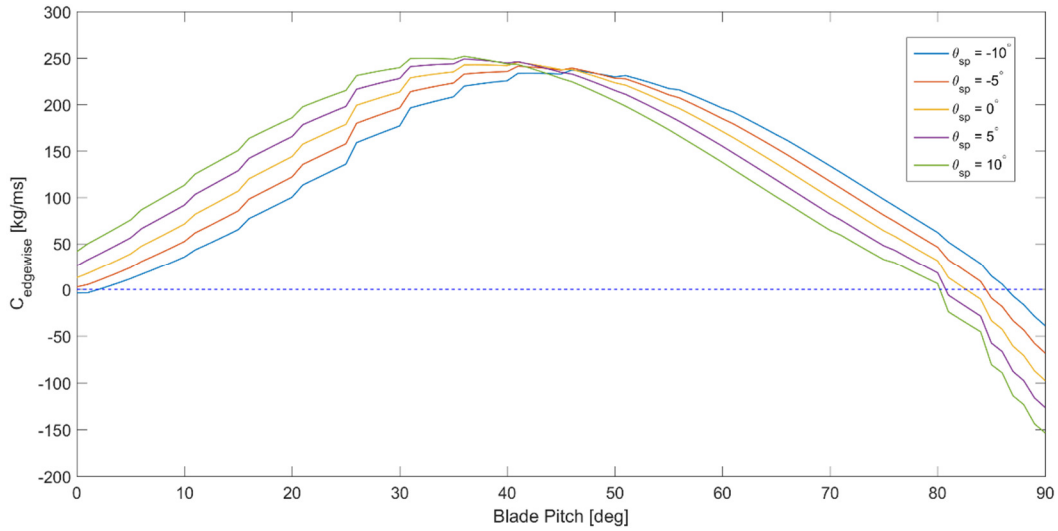

Figure 3.16: Edgewise aerodynamic damping values aligned along chord direction of blade 1 at different blade pitch angles over several structural pitch angles

From Fig [3.16], it is observed that increasing the structural pitch angle not only delays the point where the peak value is reached but also increases the peak aerodynamic damping value as well. However, having a negative structural pitch angle is beneficial in the regions between 50° and 90° pitch.

From looking at the results of Petersen's equations and studying how each parameter affects the chordwise, flatwise and edgewise aerodynamic damping values, it can be concluded from this chapter that at moderate nacelle yaw angles, there is a large risk in inducing idling instabilities. It can also be seen that for the settings chosen in this chapter, lowering the pitch by at least 10° will indeed help to achieve a positive damping whilst it may be difficult to achieve positive chordwise and edgewise aerodynamic damping values by adjusting the rotor azimuth in unstable conditions.

4. Numerical Simulations for Aerodynamic Damping of a Parked Wind Turbine with Quasi Steady Aerodynamics and Constant Wind

This chapter presents the results of numerical simulations performed in Focus 6, Phatas with load cases that resemble the settings used in the analytical equations in the previous chapter.

Utilizing an aeroelastic tool like Phatas allows for the calculation of the aeroelastic response of a complete wind turbine. The model for the NREL 5MW turbine used in this thesis, consisting mainly of the blade structural and aerodynamic properties, tower properties, drive train properties and controller, was kindly provided by The Knowledge Centre WMC from which only minor changes, detailed in the later part of this chapter, were made.

From the results of the simulations summarised in this chapter, one is also able to determine how well the 2D analytical predictions at r/R=0.75 hold up against a fully modelled wind turbine. If the agreement between both sets of results are good, they also serve to validate each other.

In order to have as fair a comparison as possible and to fully visualize the effects that each parameter would have on the aerodynamic damping values, the following table details the more critical settings used in Phatas for this chapter.

Table 4.4: Critical settings in Phatas for simulations in theoretical conditions

Setting	Value	Remarks
Flap/Edge/Torsion/Support Damping	0	Structural damping values
Dynamic stall	0	Quasi-steady airfoil properties are used
Tower dynamics	OFF	Tower structural deformation is not solved
Wind option	0	Wind speed is constant with time
Shear type	0	No vertical shear is specified
Control type	0	Controller is not called and pitch is fixed
Brake time	1	Time at which the stop action (brake and pitch) is activated
Maximum time	800	Simulation time in seconds
Wind speed	50	Wind speed in ms^{-1}

4.1 Aerodynamics modelling in Phatas

Before being able to compare the results between the numerical simulations performed in this chapter and the analytical solutions in the previous chapter, it is beneficial to understand some of the fundamental principles behind the calculations employed by Phatas.

The backbone of Phatas' aerodynamic modelling is based on the BEM theory with extensions included to account for non-linear effects such as dynamic inflow and the effects of rotation amongst others.

As such, it should be noted that for simulations involving a non-rotating rotor, theoretically, the BEM theory breaks down because the disk actuator assumption is not true anymore. However, if one still chooses to apply the BEM theory as in Phatas, it can be seen that because the thrust force for a non-rotating rotor is small, the induction factors will also be small. This results in a small error and as such, the outputs calculated from Phatas for the purpose of this thesis is still acceptable.

Yawed flow in Phatas is modelled based on Glauert's autogyro theory [ref]. Essentially, the theory corrects the formulations of the thrust and thrust coefficient for an oblique flow. Again, since for a non-rotating rotor, the errors from the induction factors are small, the outputs from Phatas remain acceptable.

The last factor that was considered in assessing how reasonable the results from Phatas are expected to be is the formulation of the tip and root losses. Because of the usage of BEM theory, a Prandtl-type model is applied to correct for tip and root losses where the Prandtl factor has been derived for a semi-infinite row of parallel trailing vortex sheets. Again, this mostly works well for high tip speed ratios. Again because the induction factors are small, the tip losses calculated can be said to be very small.

For a non-rotating rotor, the tip losses can be more accurately described by induced velocities on a fixed wing in an airflow. In such conditions, because the chord length near the tip of a wind turbine as well as the wind speeds seen are relatively small, the induced velocities can also be said to be small. As such, even though the use of calculating tip losses according to Prandtl's method is not theoretically the most appropriate approach, the results are still deemed to be appropriate to be used for the purpose of this thesis.

As a final note, it must be stated that the Focus 6 package is continuously being updated. As such, two versions of Phatas were utilised in the calculations in this thesis. Version 9083 was used for the simulations in chapter 4 and version 10041 of Phatas was utilized in the simulations in chapters 5 and 6. The later version included improvements made on the model for blade bending. This was done within the scope of the IRP-Wind project and the changes to the model may influence the structural dynamic loads for blade vibrations.

4.2 Initial inspection of data

From the outputs of the simulations in Phatas, it was decided that the tip displacements would be used to give an indication of the aerodynamic damping values of the turbine. However, an initial inspection of the tip displacements revealed the difficulty in definitively ascertaining the aerodynamic damping values of the blades in the time domain.

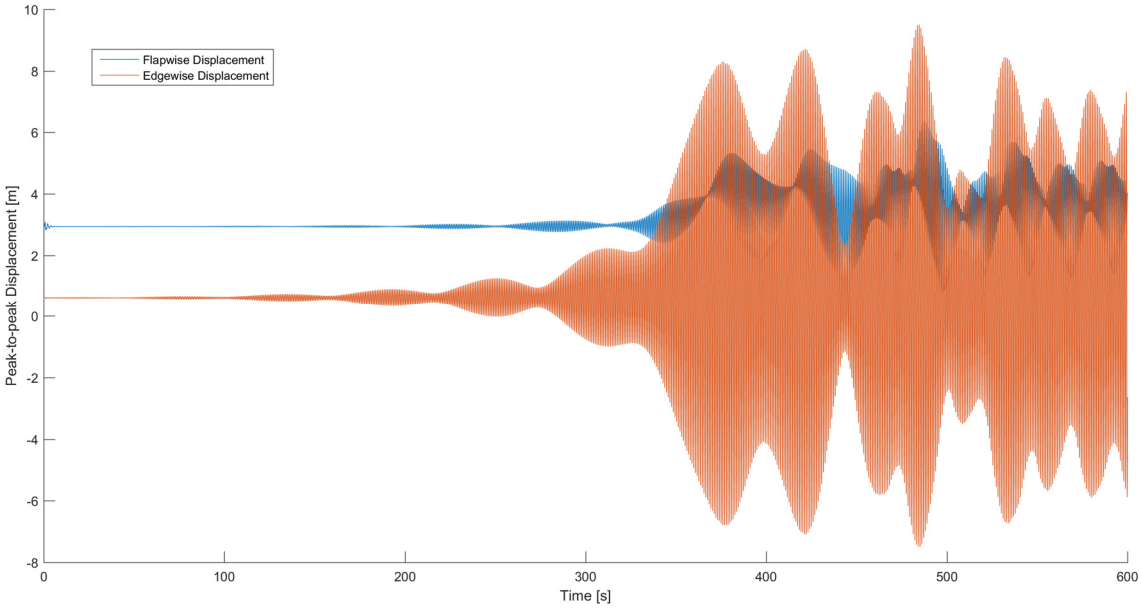

Figure 4.1: Blade 1 flapwise and edgewise peak-to-peak tip displacements at 0° rotor azimuth, 90° blade pitch and 60° yaw

Fig [4.1] is an example of a typical output that was analysed and shows the peak-to-peak tip displacements in both the edgewise as well as flapwise directions in the blade reference system for blade 1 at a setting of 0° rotor azimuth, 90° blade pitch angle and 60° nacelle yaw angle.

In looking at the tip displacements, two major difficulties in determining the aerodynamic damping values can be seen:

1. The response is highly non-linear and the characteristics of each response differs greatly between simulations. As such, the aerodynamic damping values are always changing.
2. The maximum peak-to-peak tip displacement is unrealistically large. After a certain threshold, the blade would have already failed in actuality and at such large deformations, the code is not valid anymore.

It was decided that even though a definitive aerodynamic damping value cannot be obtained in the time domain, approximating the aerodynamic damping value is a reasonable alternative approach.

But before this can be done however, a spectral analysis of the outputs of the simulations were performed to see if there were any significant driving frequencies which could then be isolated from the responses.

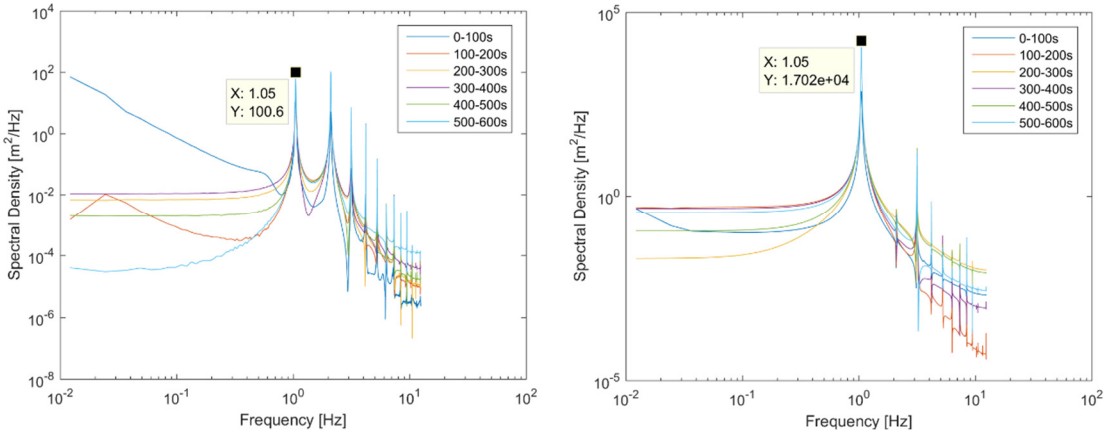

Figure 4.2: FFT of tip displacements blade 1 at 0° rotor azimuth, 90° blade pitch and -15° nacelle yaw in a) flapwise direction and b) edgewise direction

Fig [4.2] shows the fast fourier transform (FFT) of the tip displacement output of blade 1 for a simulation at 0° rotor azimuth, 90° blade pitch and -15° yaw in the flapwise and edgewise directions respectively. From Fig [4.2], it can be seen that the first major peak in both directions are at 1.05Hz.

Referring back to Table [1.3], it can be seen that this frequency is very close to the first asymmetric edgewise modes of the turbine. This suggests that the instabilities are driven by the edgewise modes.

Due to the sheer number of simulations run, FFTs were performed for only certain critical load cases taken from the outputs in this chapter. For these critical load cases, the first or second significant peaks of the FFTs in both the flapwise and edgewise directions are consistently similar to each other and close to the first asymmetric edgewise modes of the wind turbine. As the number of critical cases are also numerous, it was decided only several of such FFTs were chosen to be shown in the Appendix of this report.

After determining that the edgewise modes are driving the instabilities, an approach was then developed in order to estimate the edgewise damping ratios from the response of all the simulations undertaken in this thesis. The method used must be both flexible such that it can be applied to all types of responses as well as be reasonable enough such that the aerodynamic damping values estimated are fairly accurate.

4.3 Approach to determine the aerodynamic damping ratios

The general method used to determine the damping ratio from the response of a simulation can be broken down into three major steps.

Step 1: Inspect the data

The raw data of tip displacement versus time was firstly plotted in order to get a feel of what the response was like. From the plots, one can note if the simulations are stable or unstable and also one can see how irregular the data is.

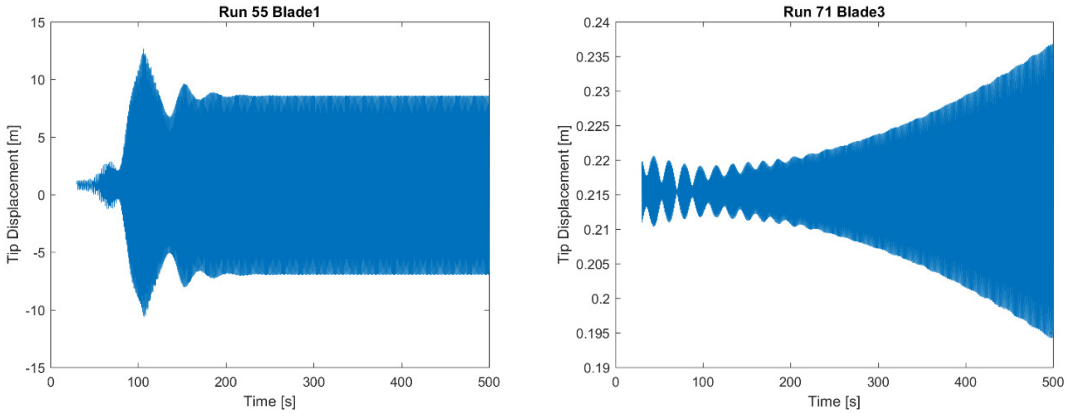

Figure 4.3: Edgewise tip displacement time series output for a) blade 1 at 26° nacelle yaw, 0° rotor azimuth (blade 1), 90° pitch, 50m/s wind speed and b) blade 3 at -70° nacelle yaw, 0° rotor azimuth (blade 1), 90° pitch, 50m/s wind speed

Just from inspecting the data, we can already see that in Fig [4.3a]:

- We can expect quite a large negative damping ratio because of the rate of increase in the tip displacement*.

*It is noted once again that at very large tip displacements, the simulation results are not valid. This will be taken into account in later steps.

From Fig [4.3b] we can see that:

- The tip displacements are very small.
- However, we can also expect to see a slight negative damping ratio.
- It can also be seen that the time series response below 100 seconds is highly irregular.

Step 2: Apply a bandpass filter

In order to clean up the signals, especially those that are highly irregular, a bandpass filter is applied to the responses through the following steps:

- Determine the mean of the raw data series
- Correct the data series such that the mean is zero
- Apply a 4th order butterworth bandpass filter for a lower and upper threshold of 20% from the averaged 1st edgewise frequency (taken from NREL 5MW reference)
- Add back the mean to the filtered data series

The averaged 1st edgewise frequency is calculated by taking the average of both the 1st blade asymmetric edgewise pitch and yaw frequencies calculated in FAST and ADAMS as shown in Table [1.3] and is as follows:

$$Ave\ 1st\ edgewise\ freq = \frac{1.0793 + 1.074 + 1.0898 + 1.0877}{4} = 1.0827\text{Hz} \qquad \text{Eqn 4.1}$$

Below are examples of an irregular and a relatively clean data series before and after the application of the bandpass filter between 30s and 70s into the simulations.

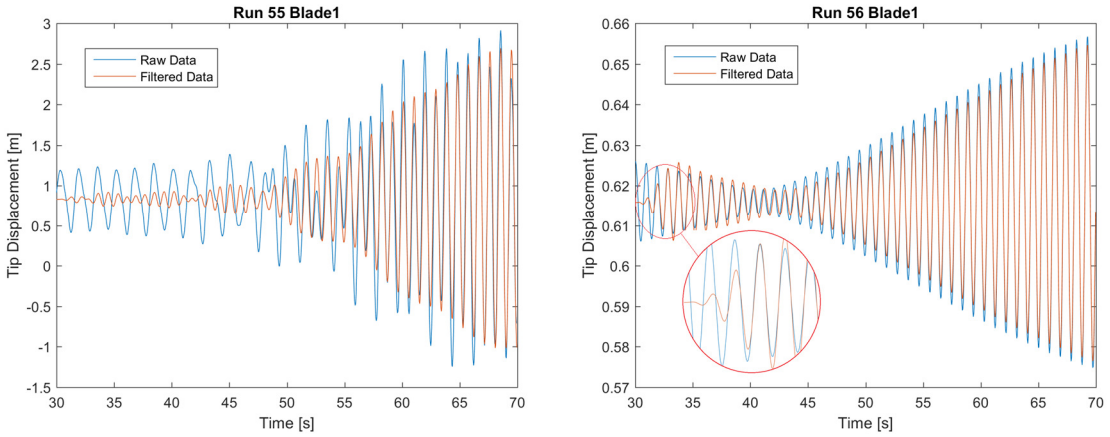

Figure 4.4: Filtered and unfiltered edgewise tip displacement time series output for a) blade 1 at 26° nacelle yaw, 0° rotor azimuth (blade 1), 90° pitch, 50m/s wind speed and b) blade 1 at 60° nacelle yaw, 0° rotor azimuth (blade 1), 90° pitch, 50m/s wind speed

One thing to note is that the filtered series always starts out 'flat' as can be seen by the zoom in of Fig [4.4b]. This is an inherent phenomenon in applying a filter but was pointed out as care should be taken not to use this part of the signal in further steps.

Step 3: Apply a curve fit to the filtered series and calculate the damping ratio

After filtering the time series output, as shown in Fig [4.4], the data must be appropriately reduced where the response (be it decaying or growing) is still accurately captured. A rule of thumb was to focus on the data between 30s and 70s into the simulation.

A script was subsequently written to identify the peaks and apply a fitted curve through the peaks corresponding to:

$$y_{fit} = ae^{bx} + ce^{dx} \qquad \text{Eqn 4.2}$$

A two term exponential fit was chosen as the fit was seen to be cleaner than when a one term exponential fit was applied.

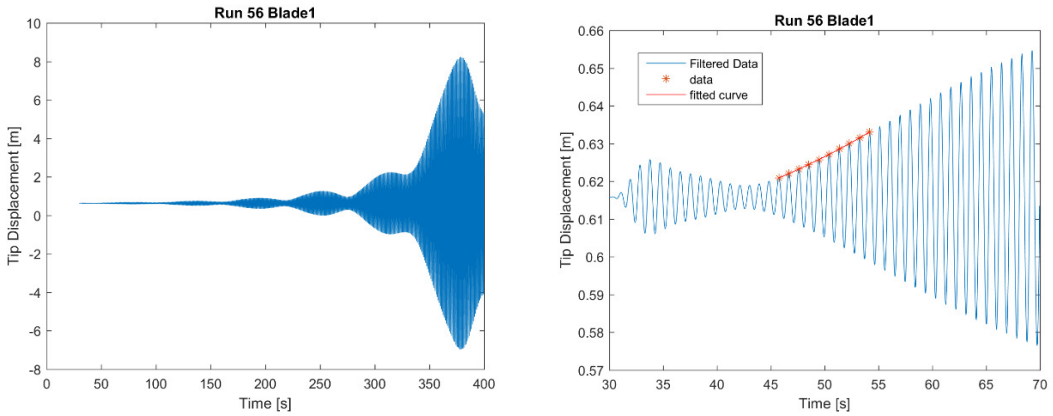

Figure 4.5: a) Filtered time series and b) Zoom in of filtered time series with peaks identified and curve fit for the edgewise tip displacement time series output of blade 1 at 60° nacelle yaw, 0° rotor azimuth (blade 1), 90° pitch, 50m/s wind speed

Fig [4.5b] shows an example of the reduced data with the peaks identified and recorded between 45s and 55s into the simulation. A curve was fitted through the data points and the logarithmic decrement was determined from the values of the fitted curve at the time of the first two peaks.

$$\delta = \ln\left(\frac{y_{fit@1^{st}\ peak\ from\ 45s}}{y_{fit@2^{nd}\ peak\ from\ 45s}}\right) \qquad \textbf{Eqn 4.3}$$

The damping ratio was then calculated from the approximate logarithmic decrement.

$$\zeta = \frac{{}^{\delta}/_{2\pi}}{\sqrt{1 + \left({}^{\delta}/_{2\pi}\right)^2}} \qquad \textbf{Eqn 4.4}$$

In order to correctly calculate the damping ratio in time series with negative displacements, for runs where the mean displacement is less than zero, the peak points and fitted curve were performed for the lower part of the oscillation as shown below in Fig [4.6].

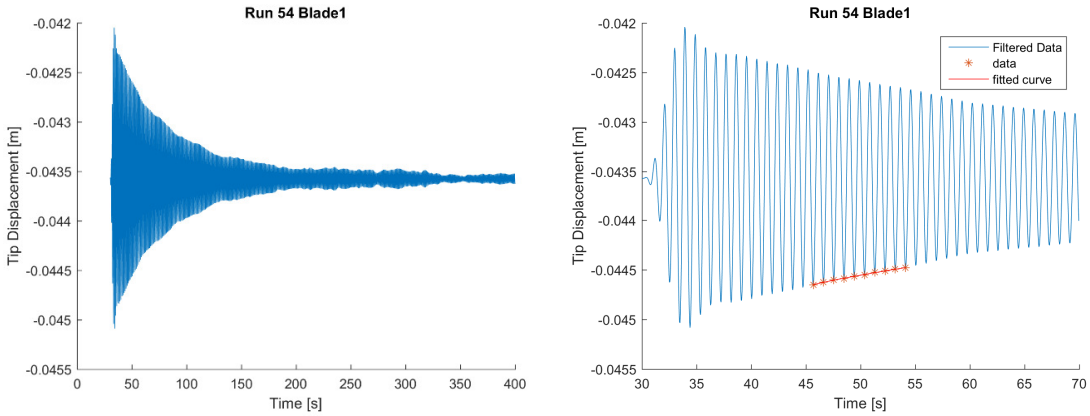

Figure 4.6: a) Filtered time series and b) Zoom in of filtered time series with peaks identified and curve fit for the edgewise tip displacement time series output of blade 1 at 0° nacelle yaw, 0° rotor azimuth (blade 1), 90° pitch, 50m/s wind speed

However, once again, because of the difference in the responses between simulations, fitting the points between 45s and 55s will not yield a reasonable approximation of the damping ratio for every simulation. Cases that are not able to follow this standard approach have been grouped into two main sets and the method to determine the damping ratio is described in two examples shown below.

Example case 1: Erratic signal but with clear trend

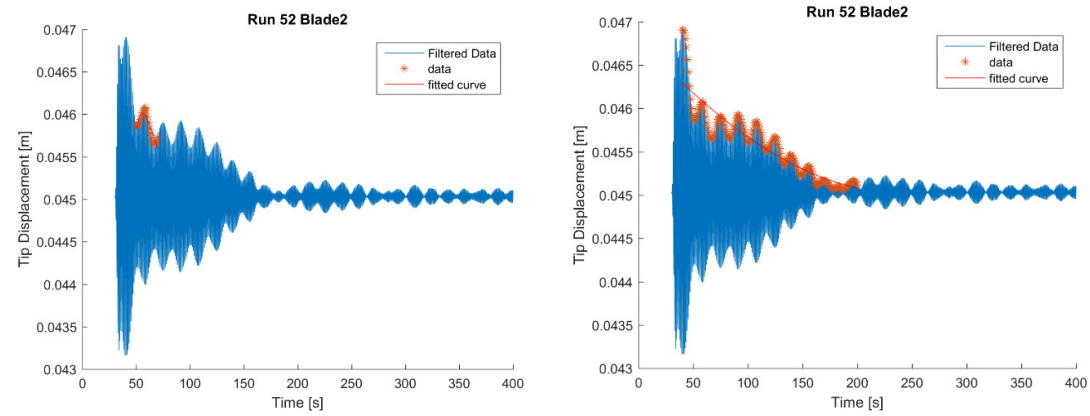

Figure 4.7: a) Filtered time series with default curve fit and b) Filtered time series with extended curve fit for the edgewise tip displacement time series output of blade 2 at -90° nacelle yaw, 0° rotor azimuth (blade 1), 90° pitch, 50m/s wind speed

From Fig [4.7a] it can be seen that not only is the response erratic but the default range is plotted over a peak. Since the displacements are small and there is clearly a quick decay until 200s, it was decided to fit a curve over the peaks between 40s and 200s.

Example case 2: Continuously growing and decaying signal

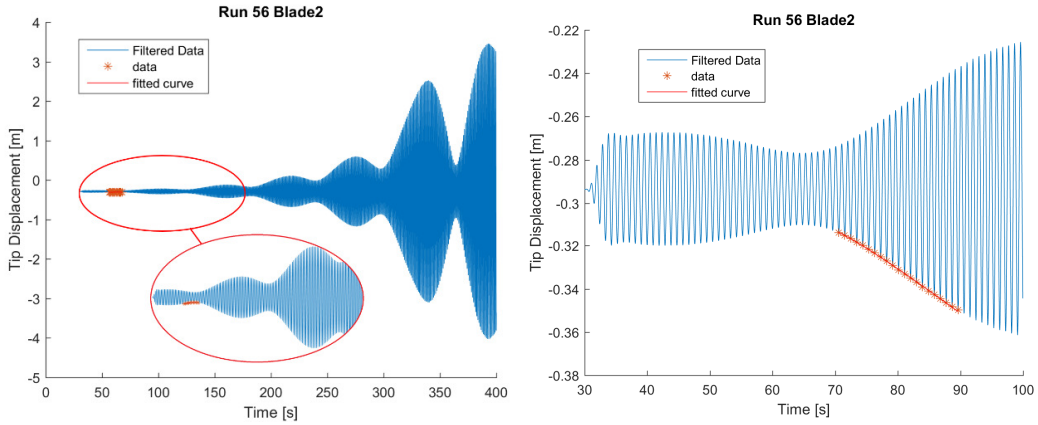

Figure 4.8: a) Filtered time series with default curve fit and b) Filtered time series with shifted curve fit for the edgewise tip displacement time series output of blade 2 at 90° nacelle yaw, 0° rotor azimuth (blade 1), 90° pitch, 50m/s wind speed

In this second case, it can be seen in Fig [4.8a] that even at the start of the simulation, the signal already grows and decays several times. The decision for these types of situations was to just take the points at the initial growth, in this case, from 70s to 90s seen in Fig [4.8b].

4.4 Analysis of outputs from Phatas simulations at varying yaw angles with quasi steady aerodynamics and constant wind

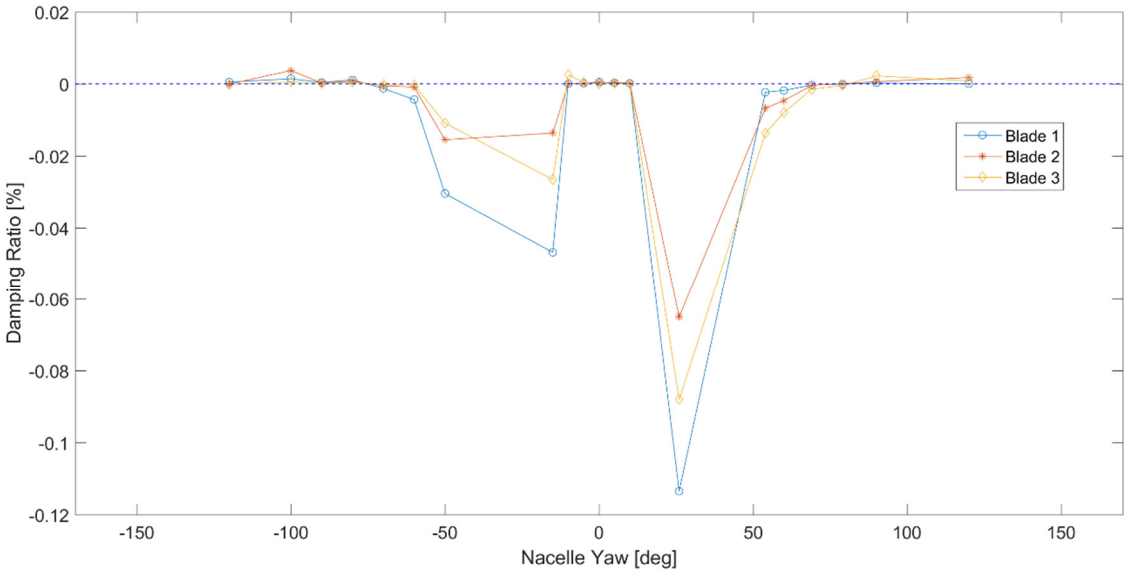

Figure 4.9: Edgewise damping ratios for all 3 blades at 0° rotor azimuth (blade 1), 90° blade pitch and varying nacelle yaw angles

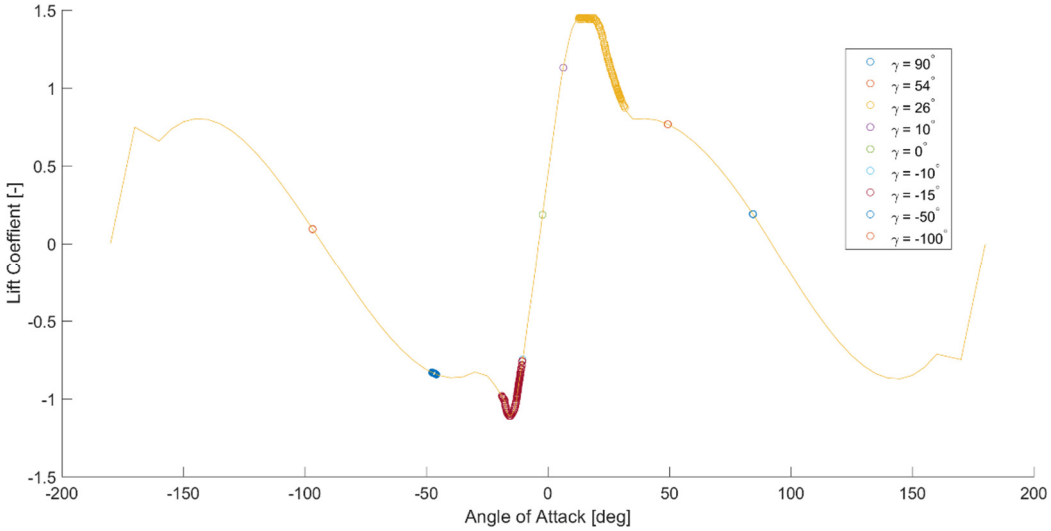

Figure 4.10: Simulation AoA vs Cl output between 45s and 55s at r/R=0.86 for various yaw angles

From Fig [4.9], a couple of observations can be made. First, it can be seen that at yaw angles between -10° and 10° and at yaw angles -70° and 69° moving outwards, the damping ratios are very close to zero. This suggests that within these regions, the wind turbine is (marginally) stable.

In contrast, between -70° and -10° and 10° to 69°, the damping ratio drops into the negative region. This shows that at these yaw angles, the wind turbine is unstable.

Comparing these results to the analytical solutions for the edgewise and chordwise aerodynamic damping values at r/R=0.75, Fig [3.5], shows that the general trends are in good agreement with each other in terms of the regions where instabilities are seen. From this comparison, apart from intrinsically showing that the numerical results also match well against the first edgewise aerodynamic damping values of (Politis & Chaviaropoulos, 2009) shown in Fig [3.7]. In addition, the results from the numerical simulations shown in Fig [4.9] were also compared against the results of the modal damping ratios of the 1st edgewise mode presented in (Bir & Jonkman, 2007). To note once again, the damping ratios in (Bir & Jonkman, 2007) were determined by an eigenanalysis performed after either linearizing the wind turbine about the mean azimuth where the blades vibrate about (since it is allowed to idle in their simulations), or after a multi blade coordinate transformation is performed if the turbine is seen to rotate slowly. Comparison of the results between those shown in Fig [4.9] and those obtained in (Bir & Jonkman, 2007) were of interest as they both analyse the same reference wind turbine, the NREL 5mW turbine, in wind speeds of 50ms^{-1}, although turbulence is present in the simulations performed by (Bir & Jonkman, 2007). The results taken from table 4 of (Bir & Jonkman, 2007) are presented in graphical format in the following figure.

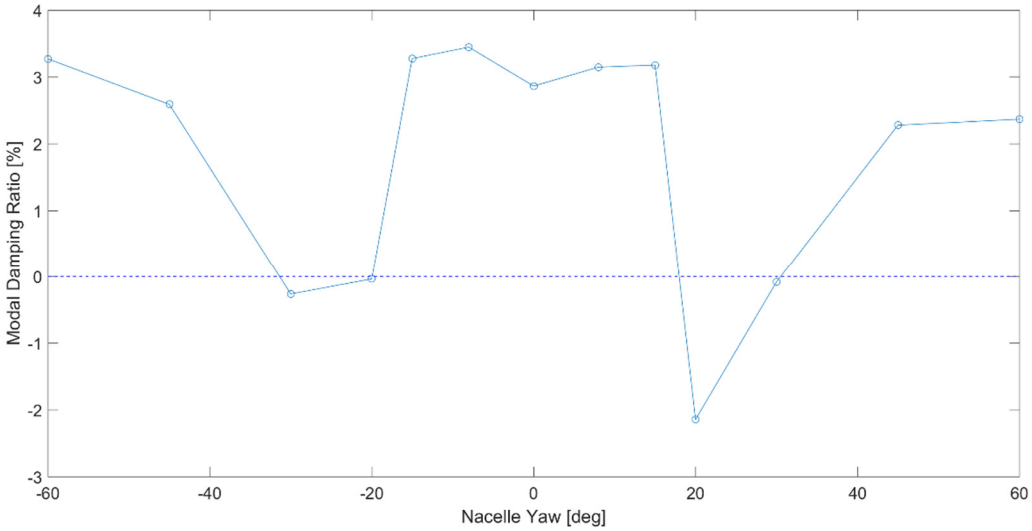

Figure 4.11: Modal damping ratios of NREL 5mW turbine idling at difference nacelle yaw settings subjected to DLC6.1 & DLC6.2 as stipulated in (International Eletrotechnical Commision, 2005) taken from (Bir & Jonkman, 2007)

Comparing the results shown in Fig [4.11] against the results obtained from Phatas in Fig [4.9] shows a good agreement in terms of the regions where instabilities are seen. It can also be noticed that the regions where positive damping ratios are seen in Fig [4.11] is higher than those in Fig [4.9]. One possible reason for this is that by letting the wind turbine idle, more damping may be added to the system. Also, it can be noted that the damping ratios in Fig [4.11] were determined by linearizing the non linear aeroelastic model about a steady state condition and performing eigenanalysis whilst the results in Fig [4.9] were obtained directly in the time domain. This could also be another possible reason for the differences in results.

Fig [4.10] shows the AoA vs Cl points of certain simulations at various yaw angles taken between 45s and 55s of each simulation superimposed over the quasi steady table values of the airfoil section at r/R=0.86 (NACA61-A17). Apart from being able to visualise where some of these simulations lie on the AoA vs Cl curve, since quasi steady aerodynamics are used in the simulations, it can be seen that the angle of attack values match very well with how the angle of attack was defined in the analytical solutions for varying yaw angles, Eqn [3.14]. It can also be seen that the AoA vs Cl points of the simulations at the yaw angles that exhibit the lowest edgewise aerodynamic damping values, 26° and -15° yaw, lie on the steepest portions of the curve in the post stall region. It can also be seen that as the angles of attack increase more than +/- 50°, the damping ratios are seen to be getting more stable.

It is also noticed from the results of the numerical simulations, the trends in the damping ratio for all three blades are the same whereas in the analytical solutions, blades 2 and 3 tend to have a different trend from blade 1.

The reason for this is that in the numerical simulations, the complete wind turbine is analysed instead of each individual blade. As such, each edgewise or flapwise mode seen on a blade translates to three different modes on a turbine, two asymmetric and one symmetric. As the

rotor speed is increased from zero, the asymmetric modes become whirling modes. An instability in any one of these modes translates to an instability in the entire turbine which will be seen by all three blades and this is observed in the numerical results. In the analytical solutions however, each blade is analysed individually with no interactions accounted for.

4.5 Analysis of outputs from Phatas simulations at varying rotor azimuths with quasi steady aerodynamics and constant wind

The following figures summarize the approximate damping ratios for all three blades at 90° blade pitch and 30° nacelle yaw for a range of rotor azimuths from 0° to 360°.

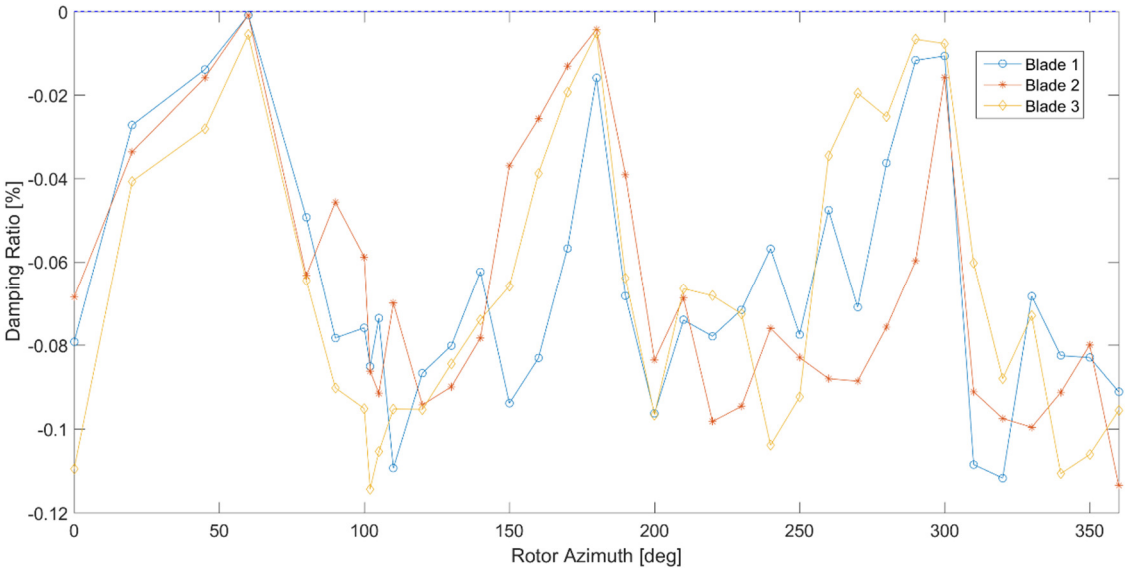

Figure 4.12: Edgewise damping ratios for all 3 blades at 90° blade pitch, 30° nacelle yaw and varying rotor azimuths

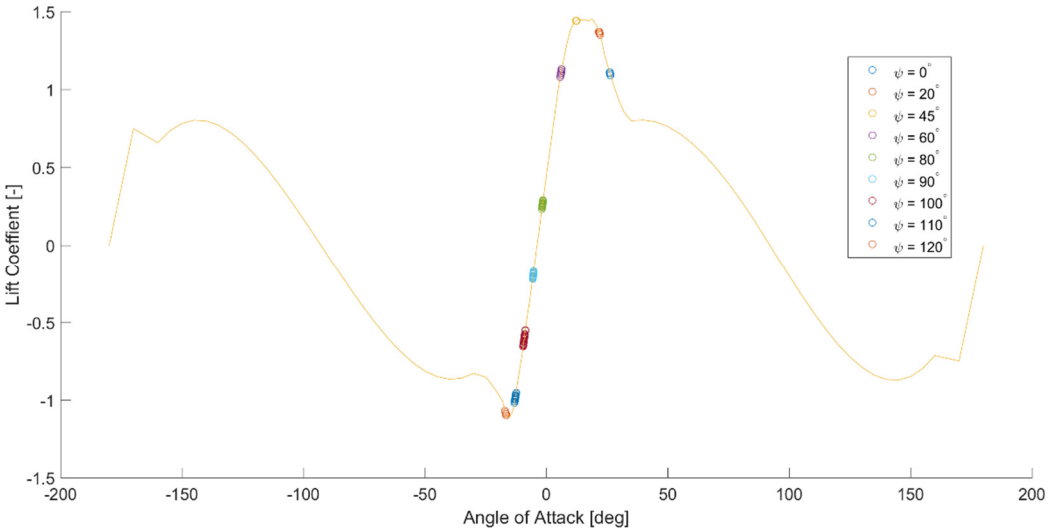

Figure 4.13: Simulation AoA vs Cl output between 45s and 55s at r/R=0.86 for various rotor azimuths

From Fig [4.12], it can be seen that the response follows a somewhat sinusoidal pattern repeating itself at roughly every 120°. This is to be expected for a wind turbine with a three

bladed configuration where each blade is 120° apart from each other. As such, it can be noted that at an originally unstable setting, rotating the blades 60° from the 12 o'clock position seems to improve the damping ratio quite significantly. It can also be seen that conversely, the default setting of parking blade 1 in the 12 o'clock position seems to induce the highest instabilities. Again, the trend in these results agree relatively well with the first 120 degrees of the analytical solutions in Figs [3.9] and [3.11], where the aerodynamic damping is seen to generally increase from 0° until a certain point (around 70° in the analytical solutions) where it decreases again.

Fig [4.13] presents the AoA vs Cl points of certain simulations at various rotor azimuths taken between 45s and 55s of each simulation superimposed over the quasi steady table values of the airfoil section at r/R=0.86 (NACA61-A17). In looking at Fig [4.13] it can be seen that the azimuths where the lowest damping ratios are seen are in the post stall regions of the curve.

4.6 Analysis of outputs from Phatas simulations at varying pitch angles with quasi steady aerodynamics and constant wind

Finally, the following figures summarize the approximate damping ratios for all three blades at 0° rotor azimuth (for blade 1) and 30° yaw for a range of blade pitch angles from 0° to 90°.

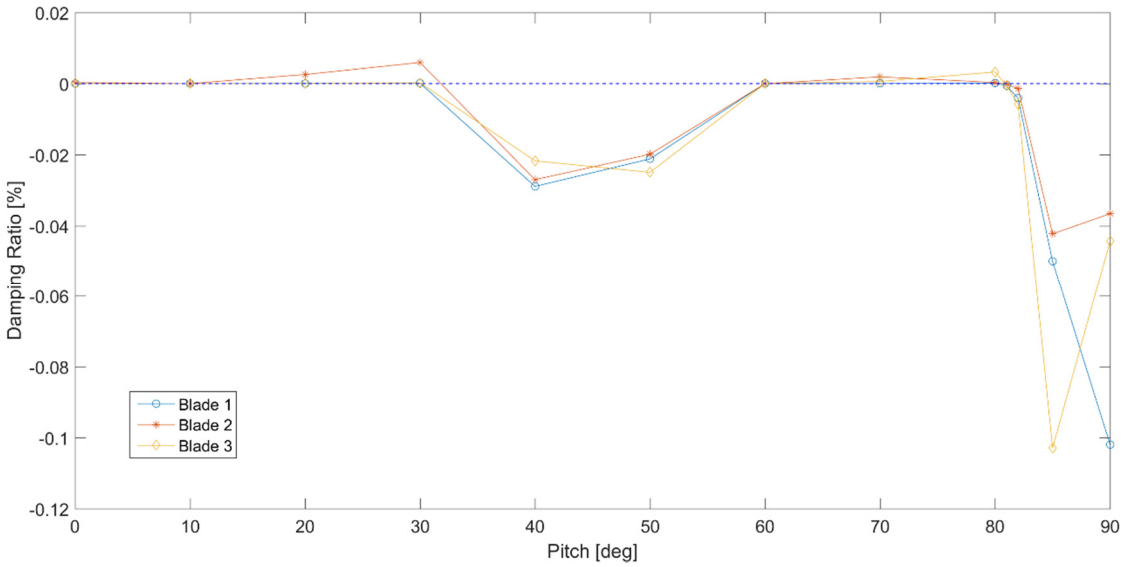

Figure 4.14: Edgewise damping ratios for all 3 blades at 0° rotor azimuth (blade 1), 30° nacelle yaw and varying blade pitch angles

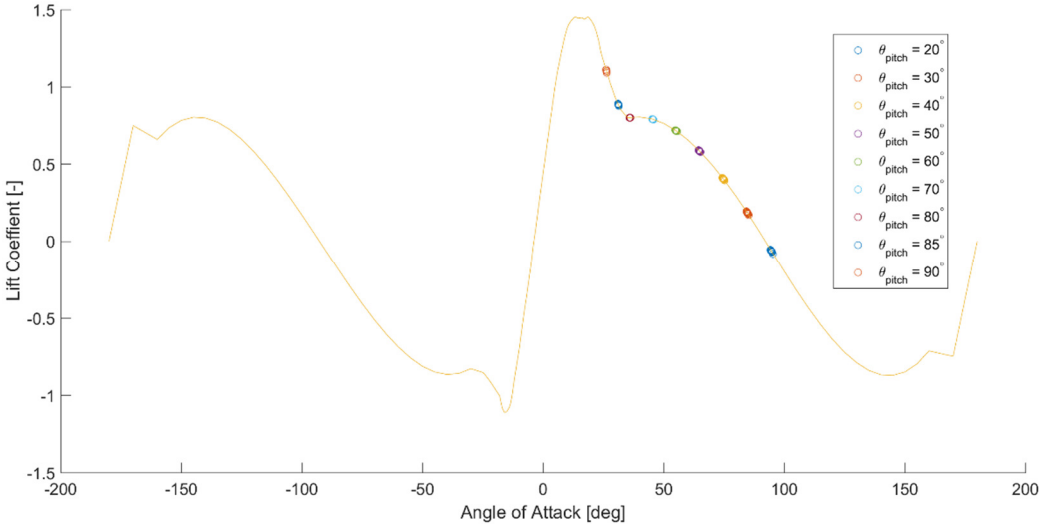

Figure 4.15: Simulation AoA vs Cl output between 45s and 55s at r/R=0.86 for various pitch angles

From Fig [4.14] it can be seen that the damping ratios are the lowest from 90° to roughly 80° after which near zero damping ratios are seen until 60° pitch. From there, the damping ratios drop again until 30° pitch where they return to near zero values (after a slight overshoot for blade 3 in the edgewise direction). This trend once again generally matches well with the analytical solutions shown in Fig [3.13]. In both figures, negative aerodynamic damping values are seen from 90° to 80° pitch for all three blades. The region between 60° and 30° in the numerical solutions that sees a negative damping ratio in Fig [4.14] may be caused by instabilities from blades 2 and 3, as shown in Fig [3.13], that excite the turbine's asymmetric edgewise modes.

Fig [4.15] shows the AoA vs Cl points taken from a few of the numerical simulations at various rotor azimuths captures between 45s and 55s of each simulation superimposed over the quasi steady table values of the airfoil section at r/R=0.86 (NACA61-A17). Again, it can be consistently observed that the pitch angles where the lowest damping ratios are observed lie on the steepest portion of the curve in the post stall region. Increasing the angle of attack past this region seems to help in improving the aerodynamic damping. However, at very high angles of attack, roughly more than 50°, a drop in the damping ratio is seen again.

From these results, it can be seen that there is a benefit to feathering the blades at angles below 90° when the wind turbine is parked.

From these initial simulations in Phatas, it can be seen that the conclusions drawn from the results gathered are very much in line with what was predicted in chapter 3. It can also be seen that many of the instabilities are found at angles of attack that are just in the post stall region of the AoA vs Cl curve. As stated at the start of this chapter, the settings used in these simulations are for ideal conditions, and as such, it will be useful to see how these characteristic responses differ when more complex models are employed in the simulations.

5. Numerical Simulations for Aerodynamic Damping of a Parked Wind Turbine with Dynamic stall and Constant Wind

This chapter focuses on assessing how the inclusion of unsteady aerodynamics affects the characteristics of the wind turbine's response in certain cases where instabilities were seen previously.

Although it is difficult to further investigate the validity of the aerodynamic damping results at very high angles of attack, it is possible to further analyse the results in several of the post stall regions with the inclusion of a dynamic stall model.

The dynamic stall model employed in Phatas is based on Snel and models the time delay in the detachment and re-attachment of the flow around the airfoil in terms of an additional component to the static lift coefficient (as detailed in chapter 2). The dynamic stall model is applied in its full effect at angles of attack between -45° and 45° after which the model slowly reduces the corrections until +/-90° angle of attack where the calculation of the lift coefficient reduces to quasi steady values.

This chapter aims to determine if the dynamic stall model when applied in Phatas indeed works as intended and thereby show whether or not current state of the art aeroelastic tools are able to identify idling instabilities in their current form.

5.1 Analysis of outputs from Phatas simulations at varying yaw angles with dynamic stall and constant wind

From Fig [4.9], it can be seen that at a constant wind speed of 50ms^{-1}, a blade pitch angle of 90° and rotor azimuth of 0° (for blade 1), the minimum damping ratio is seen at 26° yaw.

Therefore in this section, simulations at yaw angles close to 26° were run with both quasi steady aerodynamics as well as with the dynamic stall model employed by Phatas. The subsequent damping ratios were then calculated once again in accordance with section 4.2.

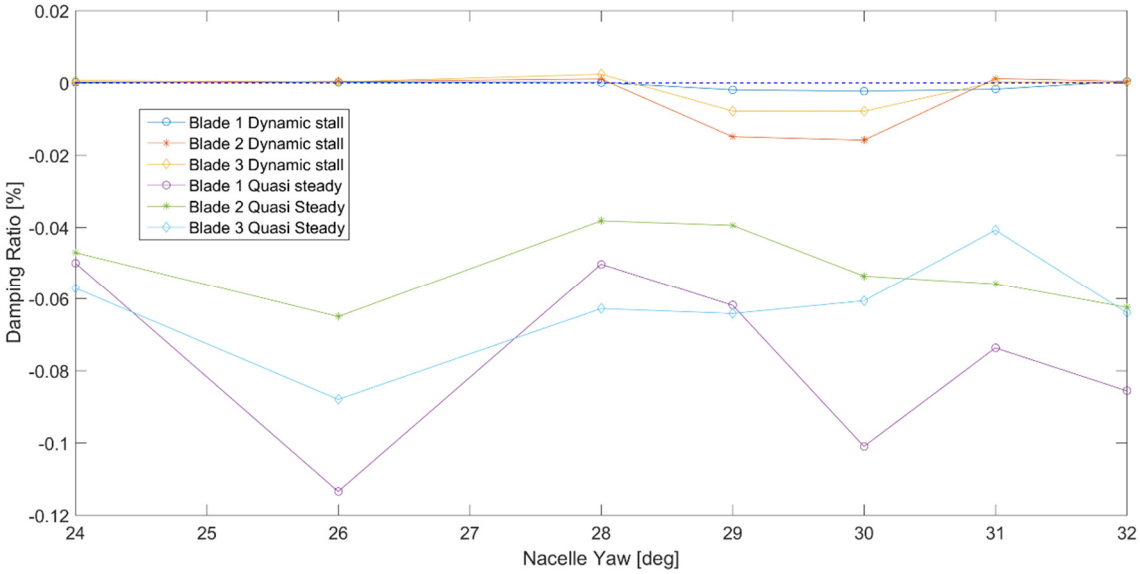

Figure 5.1: Edgewise damping ratios for all 3 blades at 0° rotor azimuth (blade 1), 90° blade pitch and varying nacelle yaw angles with quasi steady aerodynamics as well as with the dynamic stall model

Fig [5.1] presents the results of the edgewise damping ratios at various yaw angles. A quick assessment of the damping ratios of all three blades with quasi steady aerodynamics shows that the minimum damping ratio is still seen at 26° yaw for all three blades. Apart from only the yaw angle at which the minimum damping ratio is seen, it can also be seen that for the entire range of yaw angles simulated, from 24° to 32°, all three blades exhibit negative damping ratios.

Looking at the results of all three blades when the dynamic stall model is activated, it can be seen that the yaw angle at which the minimum damping ratio is seen is now at 30° for all three blades (although the damping ratios at 29° are very close to the minimum as well). It can also be noticed that for the same range of yaw angles, the simulations that were run with the dynamic stall model resulted in higher damping ratios. This subsequently also translates into a smaller range where the instabilities are seen, which is now between 28° and 31°.

In order to fully appreciate the effects of the dynamic stall model and also to determine if the corrections to the lift coefficients from the dynamic stall model are reasonable, the AoA vs Cl plots are looked at.

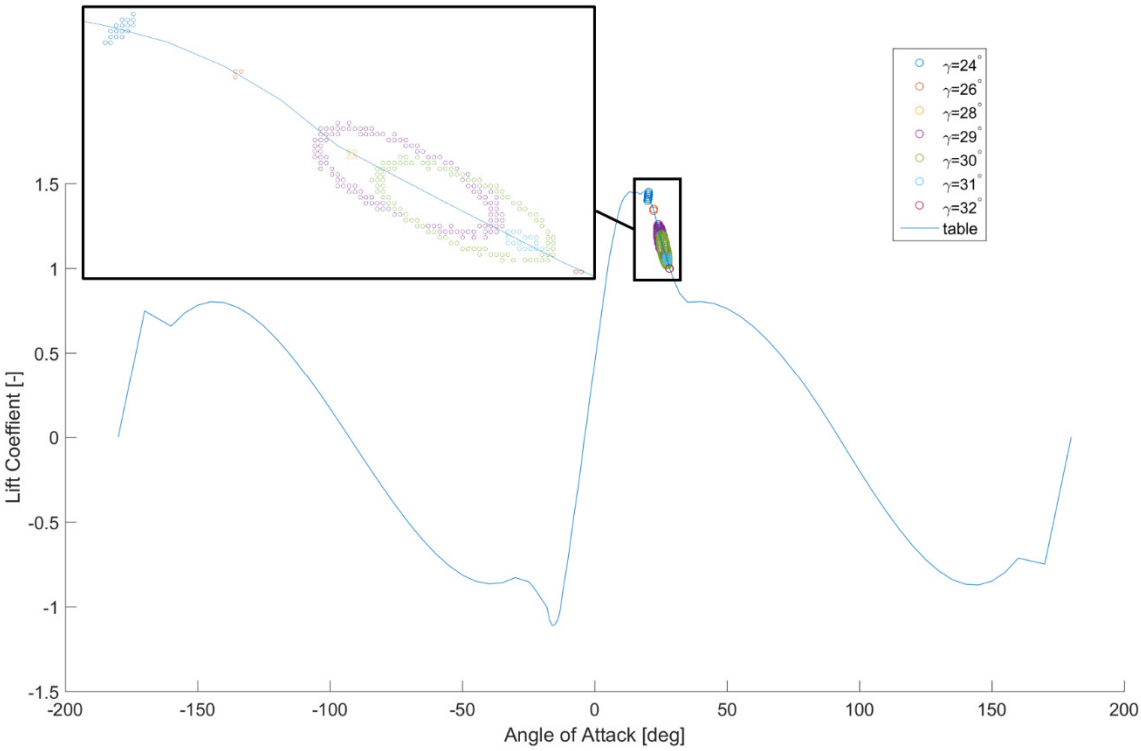

Figure 5.2: Simulation AoA vs Cl output between 45s and 55s at r/R=0.86 for various yaw angles with dynamic stall model

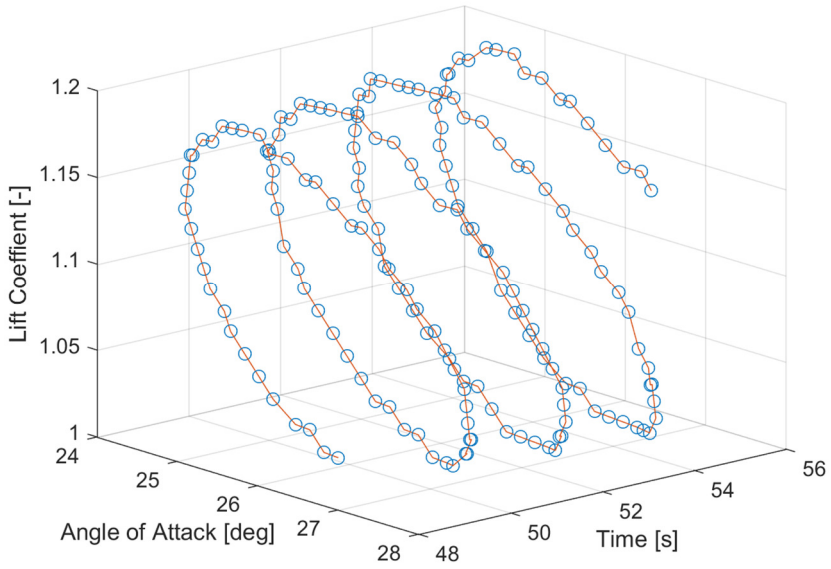

Figure 5.3: AoA vs Cl vs Time output between 45s and 55s at r/R=0.86 at 30° yaw with dynamic stall model

From Fig [5.2] it can be seen that the loops generated from the application of the dynamic stall model are rather smooth, with no sudden spikes in the lift coefficients. The loops as calculated in Phatas based on (Snel, 1997) were not validated but qualitatively compared to the loops calculated by the Beddoes-Leishman model presented in Figs [2.4] and [2.5]. In comparing the loops generated by both models, it can be seen that the range of Cl values are similar. From this, it is inferred that the dynamic stall loops calculated in Phatas are reasonable.

Fig [5.3] shows the variation of Cl values against time for the loop at 30° yaw. In this figure, the loop is seen to be moving in the clockwise direction. This is in line with what is to be expected and agrees well with the loop calculated with the Beddos-Leishman model in Fig [2.5].

The increased damping when the dynamic stall model is employed shown in Fig [5.1] can be attributed to the effects of the dynamic stall loops created. For a pitching airfoil, aerodynamic damping is present when a normal change in lift counteracts against the velocity of the pitching. When dynamic stall is present, the aerodynamic damping is increased due to an additional change in lift when the AoA is increasing.

From these results, it shows that the inclusion of the dynamic stall model produces reasonable results and also shows that although the instabilities are reduced in magnitude and are seen in a smaller range, they are still very much present.

5.2 Analysis of outputs from Phatas simulations at varying rotor azimuths with dynamic stall and constant wind

In this section, simulations are run at the same conditions as in section 4.5 except now, the dynamic stall model is included. Noting again that the outputs roughly repeat themselves every 120° azimuth, the simulations in this section have been only performed between 0° to 120° rotor azimuth.

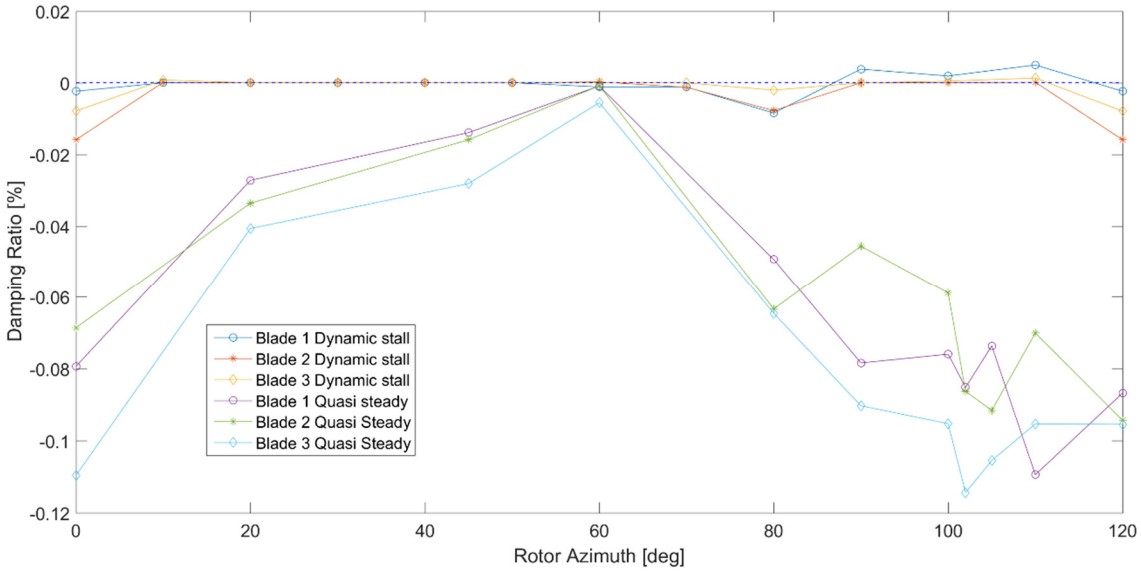

Figure 5.4: Edgewise damping ratios for all 3 blades at 30° yaw, 90° blade pitch and varying nacelle rotor azimuths with quasi steady aerodynamics as well as with the dynamic stall model

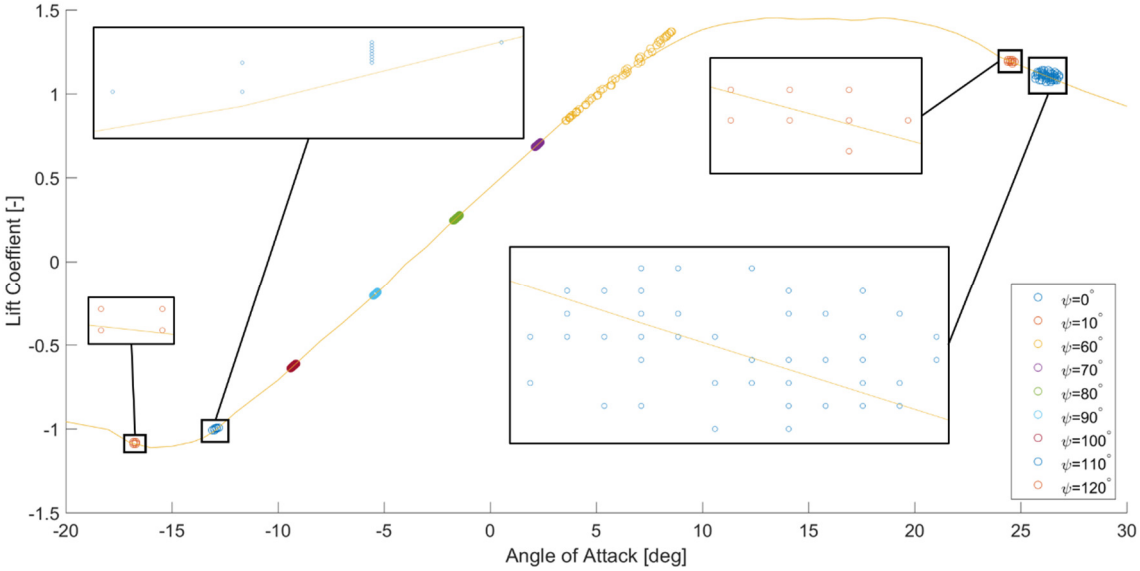

Figure 5.5: Simulation AoA vs Cl output between 45s and 55s at r/R=0.86 at various rotor azimuths with dynamic stall model

From Fig [5.4], there are a couple of observations that can be made. First, it can be seen that the damping ratios for all 3 blades are much higher when the dynamic stall model is activated. Next, the lowest damping ratios are still found at 0° and 120° azimuth. Finally, it can be seen that the range in which instabilities are found is greatly reduced. This once again shows that the dynamic stall model is seen to add damping to the system.

The dynamic stall loops are shown in Fig [5.5]. Once again, qualitative comparisons done against other simulations show that the dynamic stall model works as intended. Of particular notice, one can see that for the simulation at 60° azimuth, the maximum lift coefficient is seen to increase past the quasi steady values.

5.3 Analysis of outputs from Phatas simulations at varying pitch angles with dynamic stall and constant wind

Finally, the last section in this chapter shows the effects of the dynamic stall model applied to the simulations with varying pitch angles. Because the range where the dynamic stall model is fully activated is between -45° and 45° angle of attack, not all of the simulations previously performed in section 4.6 were repeated here.

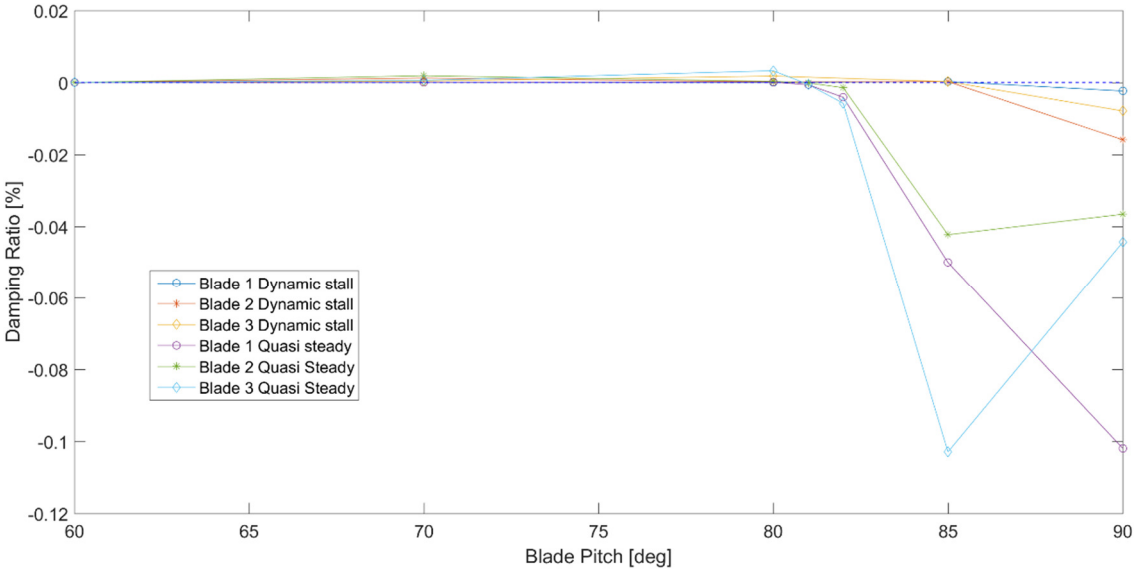

Figure 5.6: Edgewise damping ratios for all 3 blades at 30° yaw, 0° rotor azimuth (blade 1) and varying blade pitch angles with quasi steady aerodynamics as well as with the dynamic stall model

Comparing the edgewise damping ratios of all three blades with the dynamic stall model activated against the damping ratios determined from the simulations with quasi steady aerodynamics, shown in Fig [5.6], it can once again be consistently seen that not only are the damping ratios higher when the dynamic stall model is used, but also that the region where instabilities are seen have also been reduced to a smaller range, between 85° and 90° (this range might even be smaller with a higher resolution in the simulation runs).

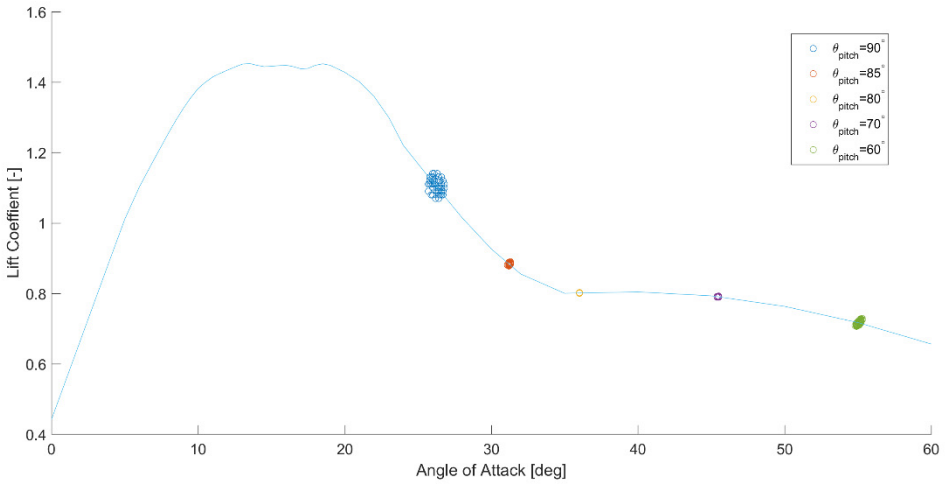

Figure 5.7: Simulation AoA vs Cl output between 45s and 55s at r/R=0.86 at various pitch angles with dynamic stall model

The AoA vs Cl plots in Fig [5.7] again shows reasonably generated dynamic stall loops. It can also be noted that angles of attack past 45°, which is the limit where the dynamic stall model is applied in its full extent, reasonable loops are still generated.

From the results gathered in this chapter, it can be concluded that the inclusion of the dynamic stall model produces results that are well in line with what should be expected where the dynamic stall loops are seen to:

1. Be generated reasonably with no unexpected fluctuations or spikes seen in the loops.
2. Shift the region where instabilities are seen.

It is also noted that although the dynamic stall loops are shown to add damping, instabilities are still seen in certain cases.

6. Numerical Simulations for Aerodynamic Damping of a Parked Wind Turbine with Dynamic stall and Turbulent Wind

In this chapter, turbulence is added to simulate what can be expected from a more realistic load case.

The parameters for the turbulent wind conditions were determined in accordance with Design Load Case (DLC) 6.2 stipulated in chapter 7, table 2 of the IEC61400-1 Edition 3 document (International Eletrotechnical Commision, 2005). This DLC calls for the use of the turbulent Extreme Wind Model (EWM) which utilizes a power law vertical shear with a power exponent of 0.11 for 10 minute average wind speeds with a 50 year reoccurrence period and a longitudinal turbulence standard deviation of 0.11.

From the previous chapter, it can be seen that the setting which is most unstable is for a wind turbine at a yaw angle of 30°, a rotor azimuth (blade 1) of 0° and with all the blades pitched at 90°. As such, these settings will be used once again in the simulation in this chapter with the average wind speed remaining at 50ms^{-1}.

A plot of the wind profile generated for the simulations in this thesis is shown below in Fig [6.1].

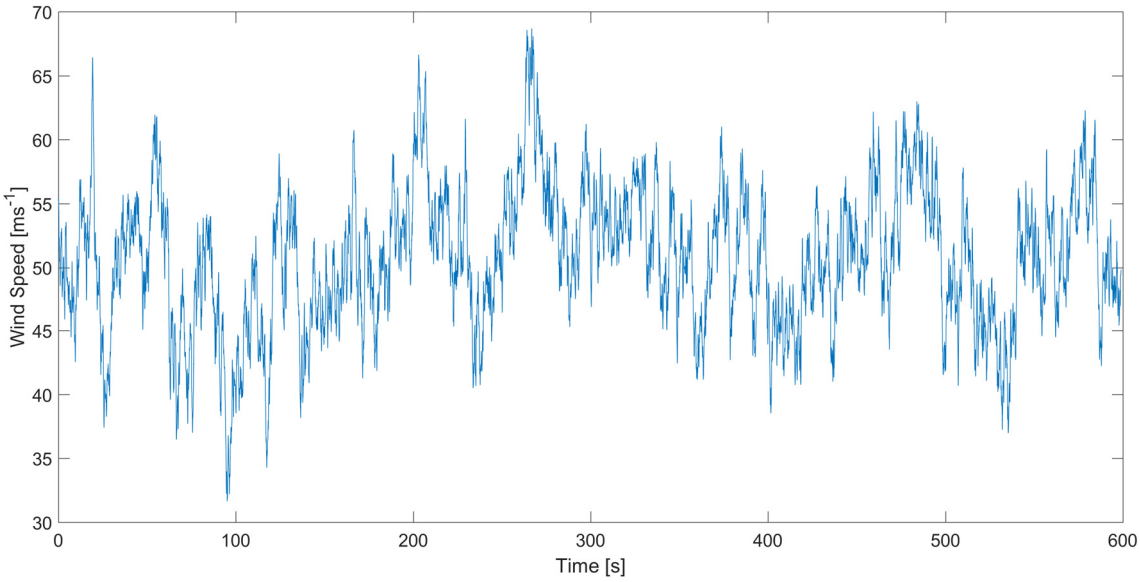

Figure 6.1: Hub wind speed profile generated by Phatas in accordance with the requirements for DLC 6.2 at a mean wind speed of 50ms^{-1} for a wind turbine at 30° yaw, 0° rotor azimuth (blade 1) and 90° pitch

6.1 Fast Fourier Transform of outputs from Phatas simulations at varying yaw angles with dynamic stall and constant wind

The fluctuating profile can be expected to affect the modal responses of the wind turbine throughout the simulation. As such, FFTs of the tip displacements in the flapwise and edgewise directions in the blade reference frame were once again generated and are shown below in Fig [6.2].

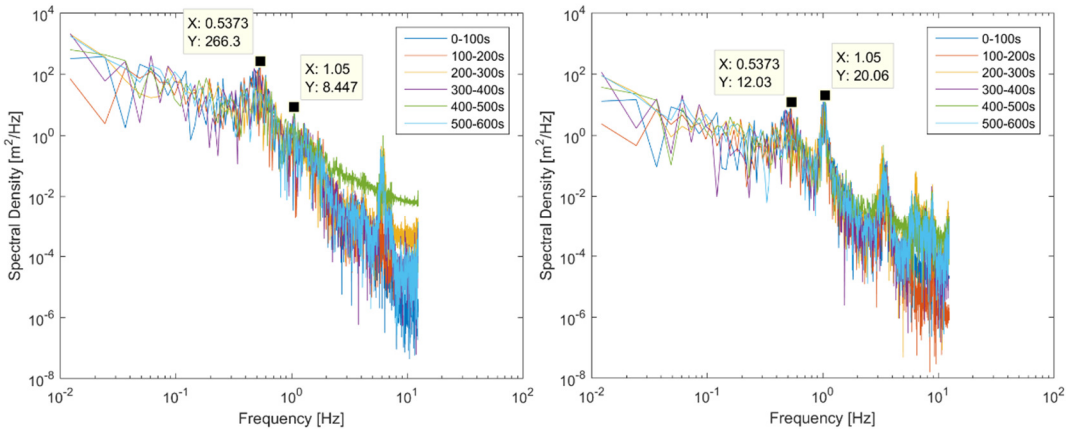

Figure 6.2: FFT of blade 1 at 0° rotor azimuth, 90° blade pitch and 30° yaw in a) flapwise direction and b) edgewise direction when subjected to the wind profile in Fig [6.1] and with the dynamic stall model activated

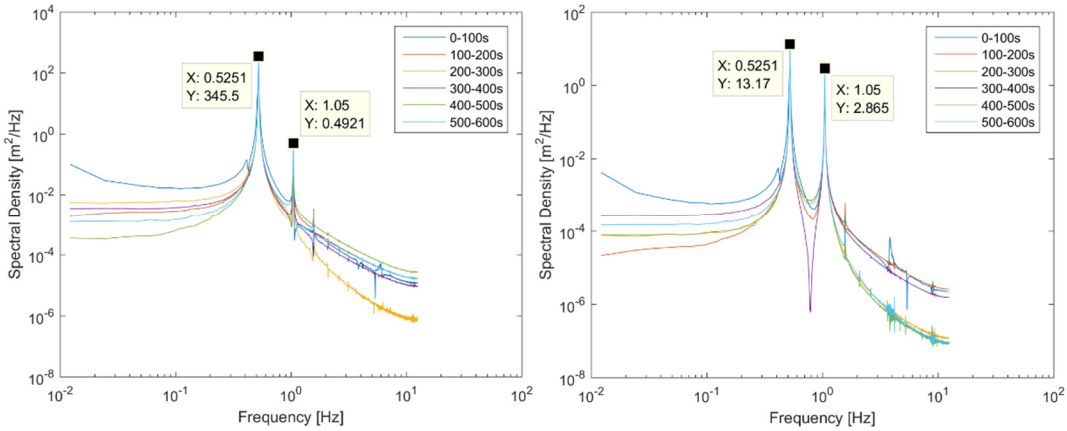

Figure 6.3: FFT of blade 1 at 0° rotor azimuth, 90° blade pitch and 30° yaw in a) flapwise direction and b) edgewise direction with constant wind speed of 50ms^{-1} and with the dynamic stall model activated

Fig [6.3] shows the FFT of the flapwise and edgewise tip displacements for a turbine at the same settings but with a constant wind speed of 50ms^{-1}. Taking the values of the spectral density to give an indication of the 'energy levels' of the responses, it can be seen that when turbulence is added, the peaks seen in the first asymmetric edgewise modes (seen at 1.05Hz) are higher. This suggests that the fluctuations in the wind speed due to the presence of turbulence adversely affects the aerodynamic damping characteristics of the first asymmetric edgewise modes.

6.2 Analysis of outputs from Phatas simulations with dynamic stall and turbulent wind

Because the wind profile is not constant, every fluctuation and small gust acts as an excitation and causes a change in the aerodynamic damping characteristics seen in the blade. As such, calculating the damping ratio from the responses is not a reasonable approach. However, it is still useful to observe the response of the wind turbine blades from the tip displacements as some insights can still be drawn in terms of assessing how each excitation from the fluctuating wind speeds contribute to the instabilities.

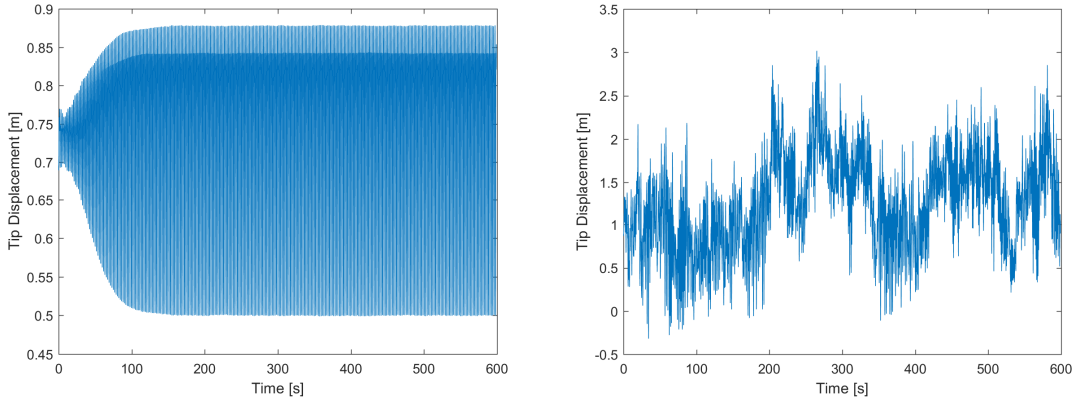

Figure 6.4: Unfiltered edgewise tip displacement time series output of blade 1 at 30° yaw, 0° rotor azimuth (blade 1), 90° pitch with dynamic stall and a) constant 50ms^{-1} wind profile b) turbulent profile according to Fig [6.1]

Fig [6.4] shows the raw output of the edgewise tip displacements of blade 1 at 30° yaw, 0° rotor azimuth, 90° blade pitch with the dynamic stall activated in both a constant wind speed of 50ms^{-1} and in a turbulent wind profile with a mean wind speed of 50ms^{-1} as per Fig [6.1]. Just from looking at the responses one can already see that when turbulence is added, the tip displacements fluctuate about a larger range, between -0.3m and 3m as compared to the simulation in a constant wind profile where the range is only from 0.5m to 0.88m.

Next, as was done in chapters 4 and 5, the edgewise tip displacements for all 3 blades in constant and turbulent wind profiles were filtered about the averaged 1st blade asymmetric edgewise pitch and yaw frequencies calculated in Eqn [4.1].

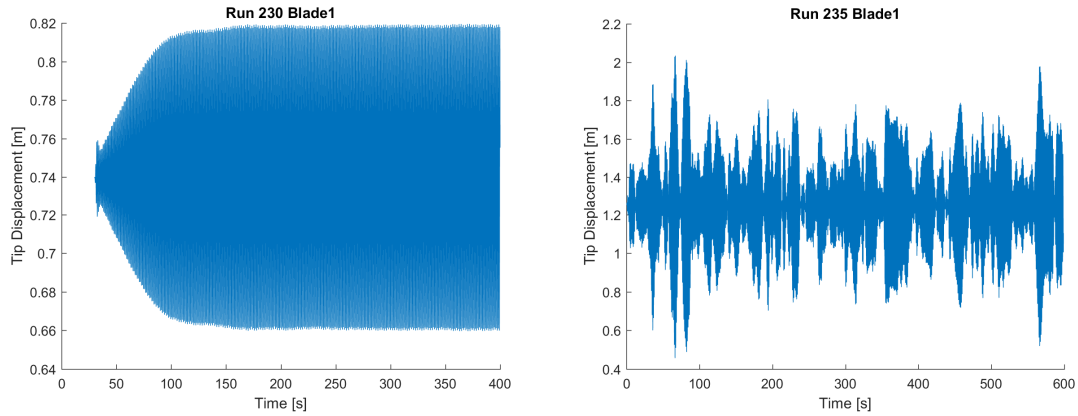

Figure 6.5: Filtered edgewise tip displacement time series output of blade 1 at 30° yaw, 0° rotor azimuth (blade 1), 90° pitch with dynamic stall and a) constant 50ms^{-1} wind profile b) turbulent wind profile according to Fig [6.1]

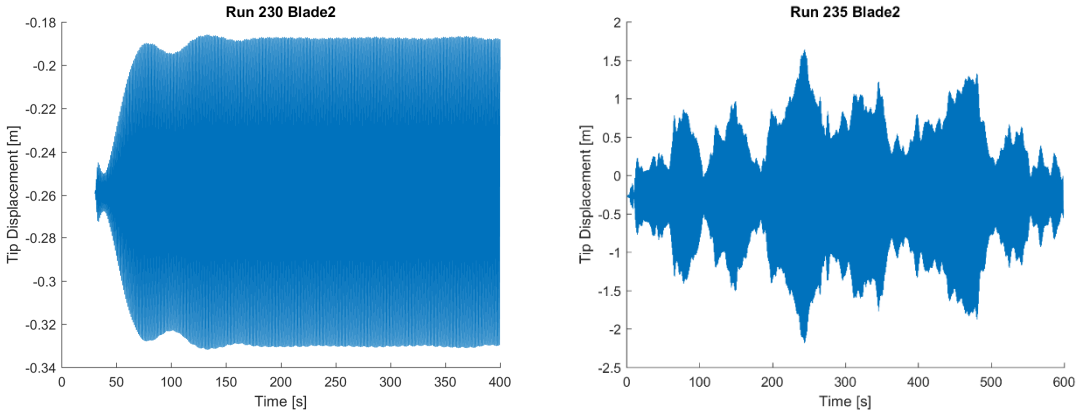

Figure 6.6: Filtered edgewise tip displacement time series output of blade 2 at 30° yaw, 0° rotor azimuth (blade 1), 90° pitch with dynamic stall and a) constant 50ms^{-1} wind profile b) turbulent wind profile according to Fig [6.1]

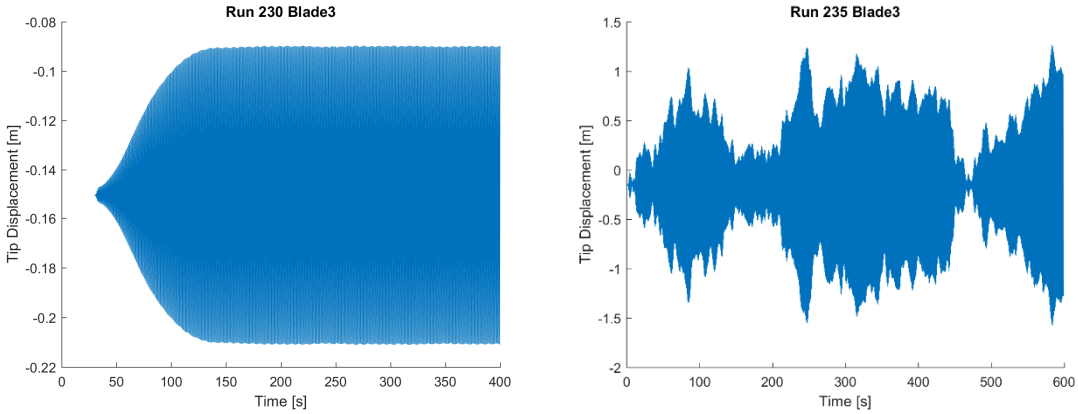

Figure 6.7: Filtered edgewise tip displacement time series output of blade 3 at 30° yaw, 0° rotor azimuth (blade 1), 90° pitch with dynamic stall and a) constant 50ms^{-1} wind profile b) turbulent wind profile according to Fig [6.1]

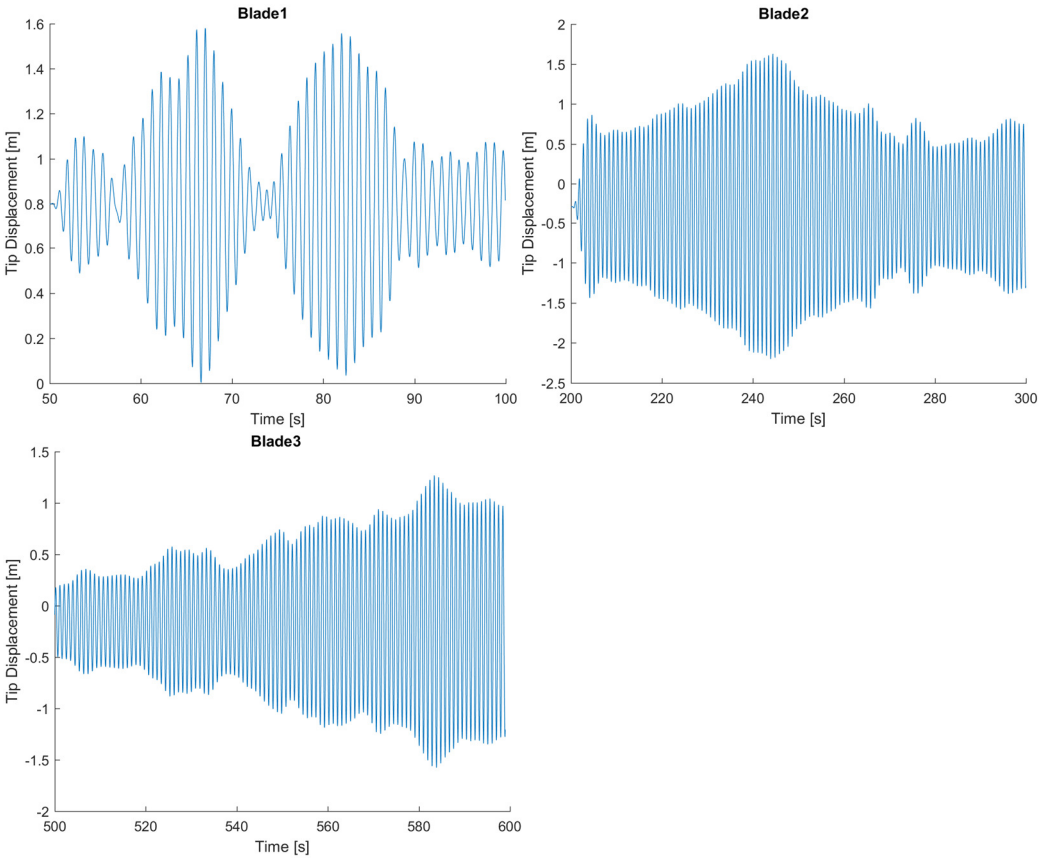

Figure 6.8: Zoomed in edgewise tip displacement time series output of a) blade 1, b) blade 2 and c) blade 3 at 30° yaw, 0° rotor azimuth (blade 1), 90° pitch with dynamic stall and turbulent wind profile as per Fig [6.1]

Figs [6.5] to [6.7] show the filtered edgewise tip displacements of all three blades of the turbine in both a constant wind speed and turbulent wind profile and Fig [6.8] shows zoomed in portions of the filtered edgewise tip displacements in a turbulent wind profile.

From these figures, it can be seen that the maximum peak to peak tip displacements of blades 1 to 3 in a turbulent wind profile are, 1.6m, 3.8m and 2.845m respectively. These are much larger than the peak to peak tip displacements of the blades when subjected to a constant wind speed.

These observations are in line with what was inferred from the assessment of the FFTs of the tip displacements where once again, it was suggested that the fluctuations in the wind speeds when turbulence is added adversely enhances the instabilities by a large factor.

7. Conclusion and Future Work

This chapter summarizes the conclusions drawn from the results of the analytical and numerical solutions performed and also details how the work presented in this report may be further expanded on.

7.1 Conclusion

Firstly, the method used to obtain the results in the analytical solutions can be said to agree well with existing literature performed for a parked blade at various yaw angles. The analytical solutions were then expanded to capture the effects of the aerodynamic damping values due to a variation in the rotor azimuths as well as pitch angles. The overall results obtained were first validated against existing simulations performed in (Politis & Chaviaropoulos, 2009) and showed from a theoretical perspective the possibility of idling instabilities in certain conditions.

Numerical simulations were then performed using the aeroelastic tool Focus, Phatas. First, the simulations were run with quasi steady aerodynamics as well as in a constant wind profile to assess the differences between numerical and analytical methods. The results obtained were in good agreement with each other by virtue of the fact that very similar trends were seen in both cases. It was noted however, that there were differences in the fact that with the use of Phatas, the responses of all three blades were very similar to each other unlike in the analytical solutions where blades 2 and 3 generally differed in results from blade 1. This was attributed to the fact that in Phatas, the turbine was modelled as a whole and the first edgewise blade mode in this case translates to a symmetrical and two asymmetrical edgewise mode on the turbine. As such, when one blade experiences an instability, the corresponding turbine mode is excited. Comparing the analytical results against existing simulations performed on the same reference wind turbine detailed in (Bir & Jonkman, 2007) revealed that the regions where instabilities were seen were consistent. However, differences in the damping ratios calculated were seen. These may be attributed to the fact that the turbine in (Bir & Jonkman, 2007) was allowed to idle and also due to the fact that a different method was utilized in order to determine the aerodynamic damping ratios.

Next, simulations were run with the dynamic stall model used by Phatas based on (Snel, 1997). An assessment of the dynamic stall loops generated from the simulations showed that the dynamic stall model worked as intended and not only reduced the range where instabilities were seen, but also served to add damping to the responses. It was also seen that at certain conditions, instabilities although small, with most of the cases going to limit cycle, were still present.

The final addition to the numerical simulations was to add turbulence. The simulation with turbulence was run at the most critical setting as determined by the simulations run with the dynamic stall model implemented in a constant wind profile. The conclusion drawn from the simulation run with turbulence showed that the fluctuations in the wind speeds excited the

instabilities more than in previous simulations where a constant wind speed was used as shown by the increase in both the peak to peak tip displacements as well as the spectral density values of the first asymmetric edgewise modes.

It must be noted that the simulations in this thesis were performed with the parking brake turned on and without structural damping. The parking brake was engaged in order to be able to assess the effects of using various rotor azimuths and structural damping was removed in order purely study the aerodynamic damping values. By adding structural damping and letting the turbine idle, it is expected that the instabilities will be alleviated to some degree.

Overall, this thesis showed that there is a strong theoretical basis to support the possibility of idling instabilities to occur in large wind turbines in high wind speeds. The results from the numerical simulations performed with a current state of the art aeroelastic tool with its limitations still largely supported the findings of the analytical solutions as well as existing literature and this indicates that they may be able to calculate for idling instabilities in certain conditions.

7.2 Future Work

The limited time taken to perform the analyses and simulations throughout the duration of this thesis revealed areas in which many of the ideas utilized may be expanded on in the future.

Wind Tunnel Testing

It can be said that none of the papers published that deal with the topic of idling instabilities in large wind turbines have measured values from an instance where such instabilities were seen in actuality. As such, the next best thing might be to develop a scaled model and subject it to tests in the wind tunnel in order to validate the conclusions drawn from these papers. In order to simulate the airflow over the model accurately, the size of the model must be limited to minimize tunnel effects. Also, at a critical size of the model, the sensors, assuming piezoelectric accelerometers are used, will also have an effect on the accuracy of the results as they may influence both the airflow around the blades as well as provide an additional loading on the blades.

Aerodynamics at very high angles of attack

This area encompasses several topics that may be explored. Firstly, it is known that the dynamic stall model employed in Phatas slowly reduces to quasi steady values from 45° to 90° and beyond. It may be of interest however, to observe the effects of the dynamic stall model still being applied in its full extent at higher angles of attack.

It was also noted from the literature review portion of this thesis that there has been one paper that has attempted to accurately model the airflow around an airfoil in standstill at an angle of attack of roughly 25° using 2D and 3D Computational Fluid Dynamics (CFD)

calculations. It was observed that the results between the 2D and 3D models differed greatly. Performing further simulations in order to resolve the discrepancies in results is beneficial in providing a more complete understanding of the air flow in such conditions.

Bibliography

Andersen, P. B., Gaunaa, M., Bak, C., & Hansen, M. H. (2009). A dynamic stall model for airfoils with deformable trailing edges. *Wind Energy*, *12*(8), 734–751. https://doi.org/10.1002/we.326

Bir, G., & Jonkman, J. M. (2007). Aeroelastic Instabilities of Large Offshore and Onshore Wind Turbines. *Journal of Physics: Conference Series*, *75*(August), 12069. https://doi.org/10.1088/1742-6596/75/1/012069

Du, Z., & Selig, M. (1998). A 3-D stall-delay model for horizontal axis wind turbine performance prediction. *1998 Asme Wind Energy Symposium*, 9–19. Retrieved from http://findit.dtu.dk/en/catalog?utf8=✓&search_field=all_fields&q=A+3-D+Stall-Delay+Model+for+Horizontal+Axis+Wind+Turbine+Performance+Prediction

Eggers, A. J., Chaney, K., & Digumarthi, R. (2003). An Assessment of Approximate Modeling of Aerodynamic Loads on the UAE Rotor. *Asme 2003 Wind Energy Symposium, Wind2003*, 283–292. Retrieved from http://findit.dtu.dk/en/catalog?utf8=✓&locale=en&search_field=all_fields&q=An+Assessment+of+Approximate+Modeling+of+Aerodynamic+Loads+on+the+UAE+Rotor

Garrick, I. E., & Reed, W. H. (1981). Historical Development of Aircraft Flutter. *Journal of Aircraft*, *18*(11), 897–912. https://doi.org/10.2514/3.57579

Hansen, M. H. (2004). Aeroelastic stability analysis of wind turbines using an eigenvalue approach. *Wind Energy*, *7*(2), 133–143. https://doi.org/10.1002/we.116

Hansen, M. H. (2007). Aeroelastic instability problems for wind turbines. *Wind Energy*, *10*(6), 551–577. https://doi.org/10.1002/we.242

Hansen, M. H., Gaunaa, M., & Madsen, H. A. (2004). *A Beddoes-Leishman type dynamic stall model in state-space and indicial formulations*. Risø National Laboratory. Retrieved from http://findit.dtu.dk/en/catalog?utf8=✓&locale=en&search_field=all_fields&q=Beddoes-Leishman+type+dynamic+stall+model+in

Hansen, M. O. L., Sørensen, J. N., Voutsinas, S., Sørensen, N., & Madsen, H. A. (2006). State of the art in wind turbine aerodynamics and aeroelasticity. *Progress in Aerospace Sciences*, *42*(4), 285–330. https://doi.org/10.1016/j.paerosci.2006.10.002

International Eletrotechnical Commision. (2005). IEC 61400-1 Wind Turbines - Part 1: Design requirements. *Wind Turbines – Part 1: Design Requirements*, *2005*, 1–92. https://doi.org/10.1055/s-2007-985912

Jonkman, J., Butterfield, S., Musial, W., & Scott, G. (2009). *Definition of a 5-MW reference wind turbine for offshore system development*. https://doi.org/10.1002/ajmg.10175

Lindenburg, C. (2014). *PHATAS Release "JAN-2014a" USER'S MANUAL*.

Manolas, D. I., Riziotis, V. A., & Voutsinas, S. G. (2016). Assessing the Importance of Geometric Nonlinear Effects in the Prediction of Wind Turbine Blade Loads. *Journal Pf Computational and Nonliear Dynamics*, *10*(July 2015), 1–15. https://doi.org/10.1115/1.4027684

McCroskey, W. J. (1981). The Phenomenon of Dynamic Stall. *NASA Technical Memorandum 81264*, 1–28. https://doi.org/10.1080/6008555886

Moriarty, P. J., & Hansen, a C. (2005). AeroDyn Theory Manual. *Renewable Energy*, *15*(January), 500–36313. https://doi.org/10.1146/annurev.fl.15.010183.001255

Petersen, J. T., Madsen, H. A., Björck, A., Enevoldsen, P., Øye, S., Ganander, H., & Winkelaar, D. (1998). *Prediction of Dynamic Loads and Induced Vibrations in Stall* (Vol. 1045).

Politis, E. S., & Chaviaropoulos, P. K. (2009). Stability analysis of parked wind turbine blades. *Scientific Proceedings of the European Wind Energy Conference 2009*, (November), 59–63.

Riziotis, V. A., Voutsinas, S. G., Politis, E. S., & Chaviaropoulos, P. K. (2004). Aeroelastic stability of wind turbines: The problem, the methods and the issues. *Wind Energy*, *7*(4), 373–392. https://doi.org/10.1002/we.133

Skrzypiński, W. R., Gaunaa, M., Sørensen, N., Zahle, F., & Heinz, J. (2014). Self-induced vibrations of a DU96-W-180 airfoil in stall. *Wind Energy*, *17*(June 2013), 641–655. https://doi.org/10.1002/we

Snel, H. (1997). Heuristic Modelling of Dynamic Stall Characteristics. *European Wind Energy Conference, Dublin Castle, Ireland*, 429–433.

V.K.Truong. (1993). A 2-D Dynamic Stall Model Based on Hopf Bifurcation. *Nineteenth European Rotorcraft Forum*.

Viterna, L. A., & Janetzke, D. C. (1982). Theoretical and experimental power from large horizontal-axis wind turbines, *82944*, 19. https://doi.org/10.2172/6763041

Wang, K., Riziotis, V. A., & Voutsinas, S. G. (2016). Aeroelastic Stability of Idling Wind Turbines. *Journal of Physics: Conference Series*, *753*, 42008. https://doi.org/10.1088/1742-6596/753/4/042008

Zandt, T. Van. (2007). FAST User's Guide. *Acta Psychiatrica Scandinavica*, *123*(6), 407–8. https://doi.org/10.2172/15020796

Appendix

FFTs at certain cases calculated from the edgewise and flapwise tip displacements in the blade reference frame in both quasi steady and unsteady aerodynamics (dynamic stall) with a constant wind speed of 50ms^{-1}.

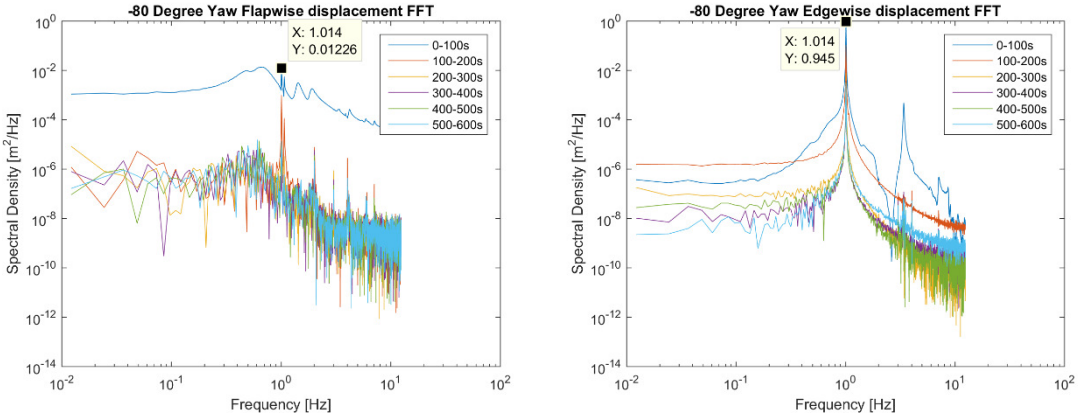

Figure A1: FFT of tip displacements blade 1 at 0° rotor azimuth, 90° blade pitch and -80° nacelle yaw in a) flapwise direction and b) edgewise direction with quasi steady aerodynamics

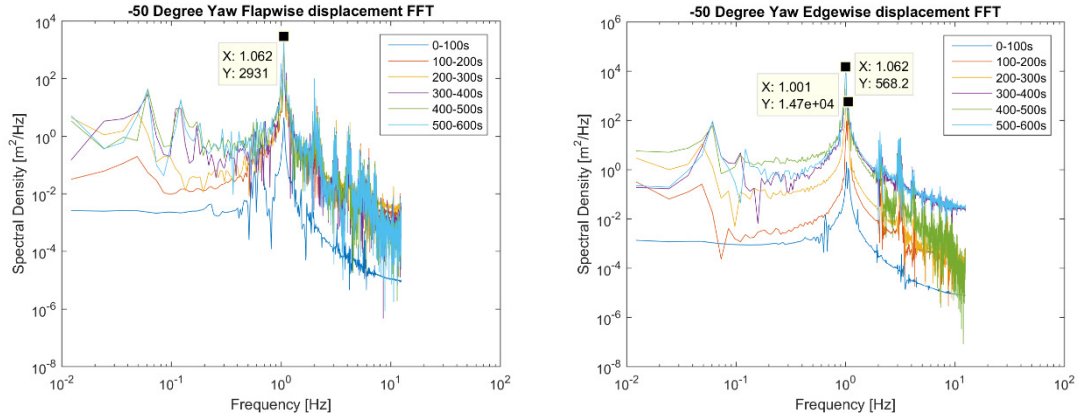

Figure A2: FFT of tip displacements blade 1 at 0° rotor azimuth, 90° blade pitch and -50° nacelle yaw in a) flapwise direction and b) edgewise direction with quasi steady aerodynamics

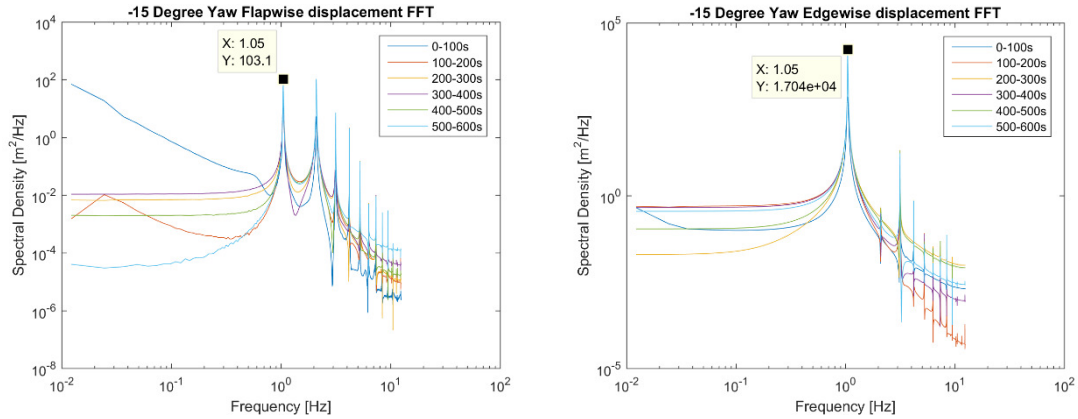

Figure A3: FFT of tip displacements blade 1 at 0° rotor azimuth, 90° blade pitch and -15° nacelle yaw in a) flapwise direction and b) edgewise direction with quasi steady aerodynamics

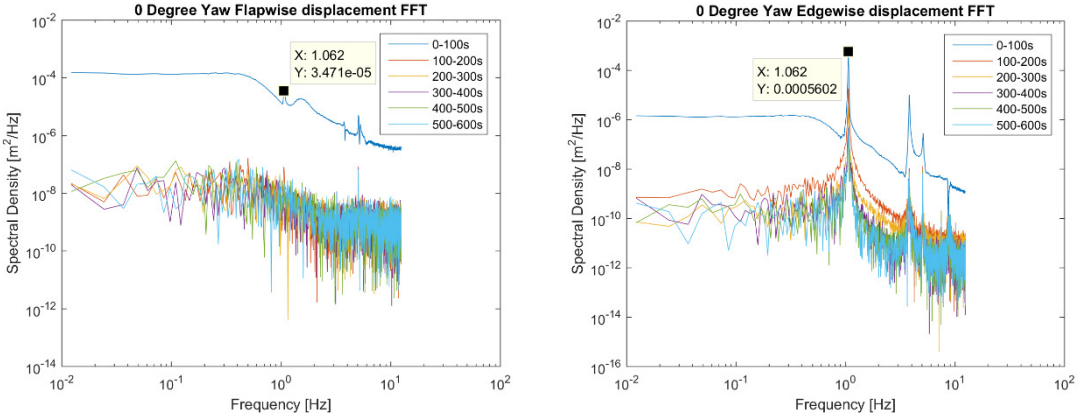

Figure A4: FFT of tip displacements blade 1 at 0° rotor azimuth, 90° blade pitch and 0° nacelle yaw in a) flapwise direction and b) edgewise direction with quasi steady aerodynamics

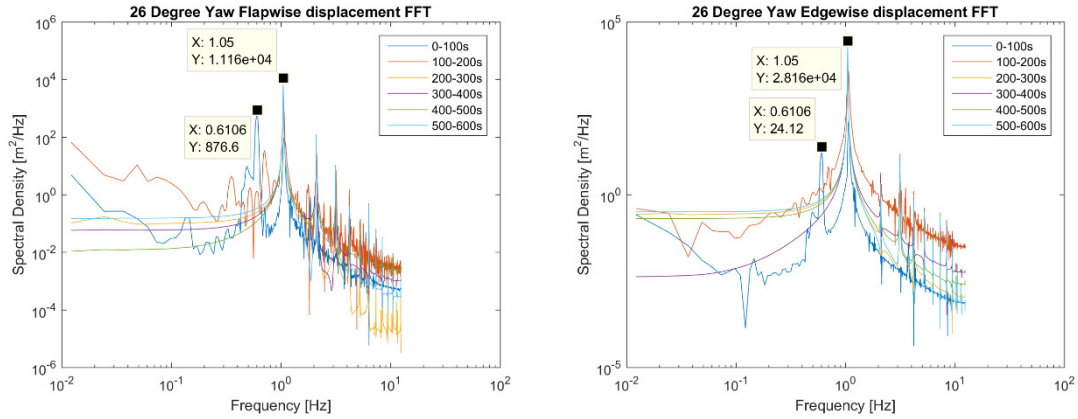

Figure A5: FFT of tip displacements blade 1 at 0° rotor azimuth, 90° blade pitch and 26° nacelle yaw in a) flapwise direction and b) edgewise direction with quasi steady aerodynamics

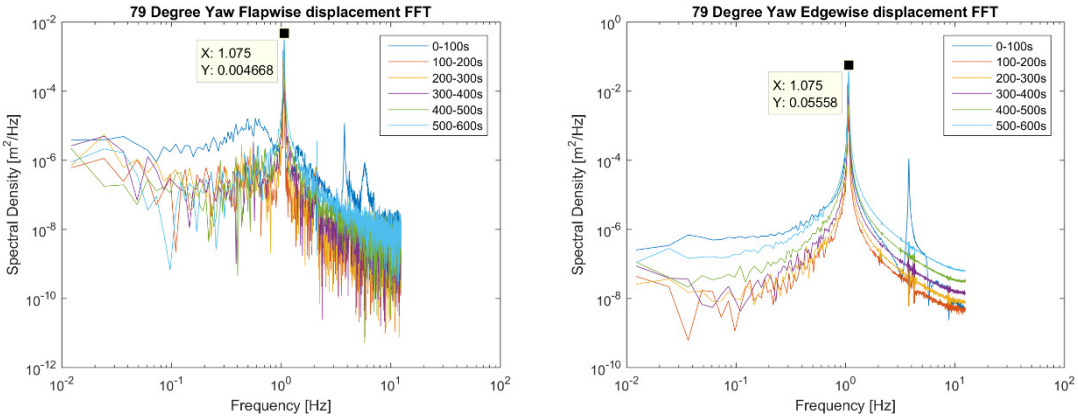

Figure A6: FFT of tip displacements blade 1 at 0° rotor azimuth, 90° blade pitch and 79° nacelle yaw in a) flapwise direction and b) edgewise direction with quasi steady aerodynamics

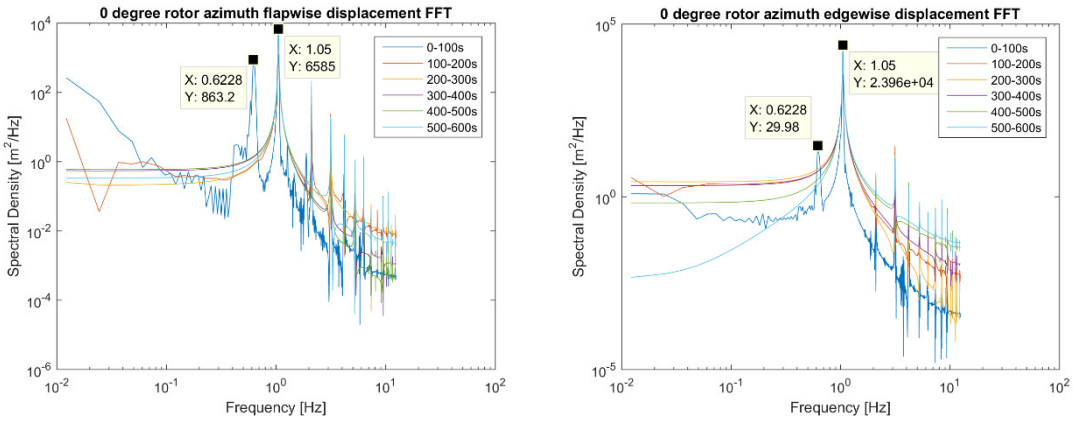

Figure A7: FFT of tip displacements blade 1 at 0° rotor azimuth, 90° blade pitch and 30° nacelle yaw in a) flapwise direction and b) edgewise direction with quasi steady aerodynamics

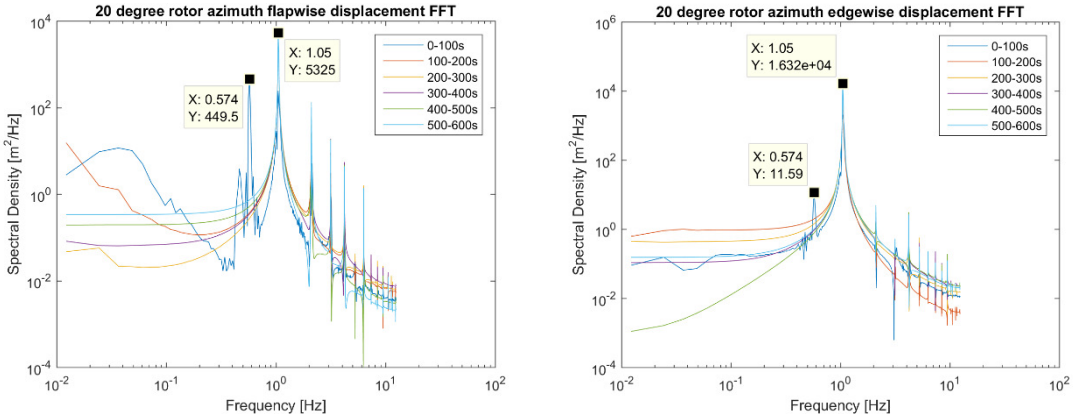

Figure A8: FFT of tip displacements blade 1 at 20° rotor azimuth, 90° blade pitch and 30° nacelle yaw in a) flapwise direction and b) edgewise direction with quasi steady aerodynamics

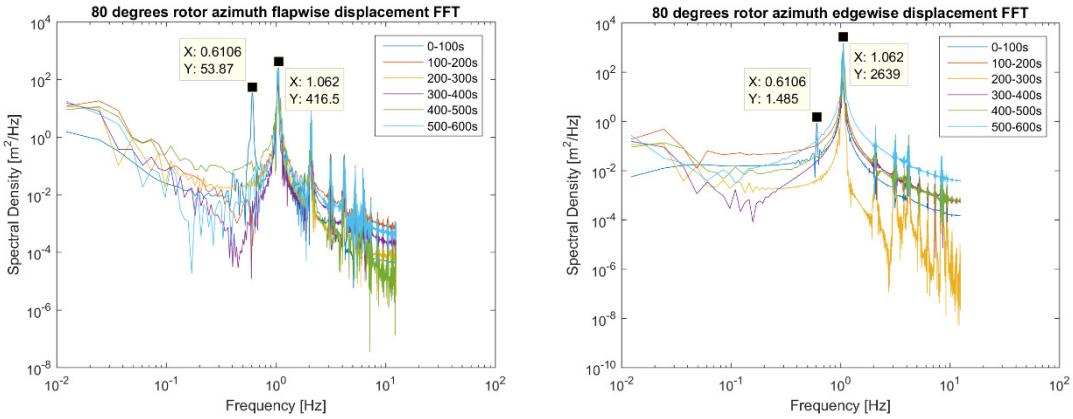

Figure A9: FFT of tip displacements blade 1 at 80° rotor azimuth, 90° blade pitch and 30° nacelle yaw in a) flapwise direction and b) edgewise direction with quasi steady aerodynamics

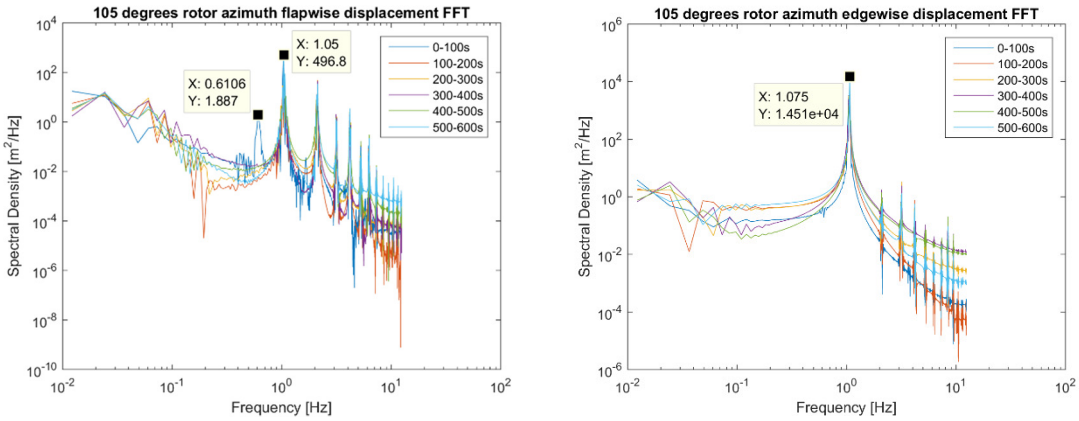

Figure A10: FFT of tip displacements blade 1 at 105° rotor azimuth, 90° blade pitch and 30° nacelle yaw in a) flapwise direction and b) edgewise direction with quasi steady aerodynamics

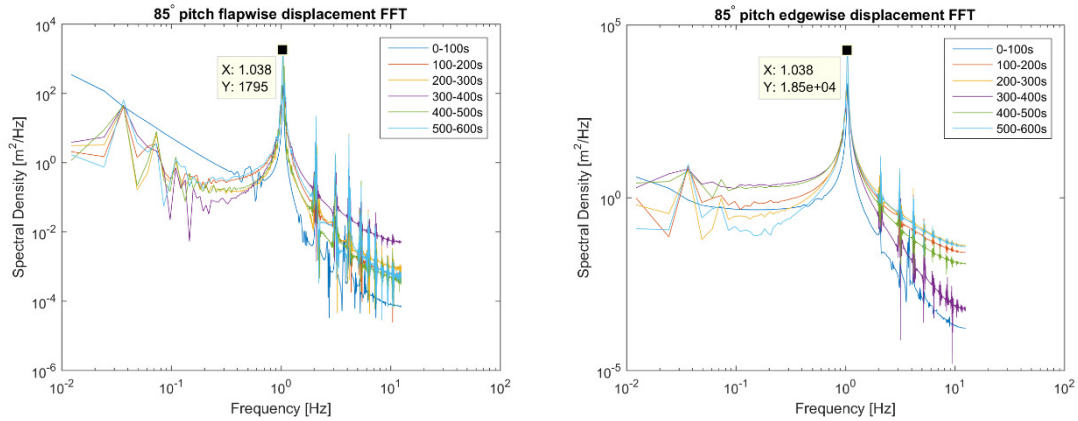

Figure A11: FFT of tip displacements blade 1 at 0° rotor azimuth, 85° blade pitch and 30° nacelle yaw in a) flapwise direction and b) edgewise direction with quasi steady aerodynamics

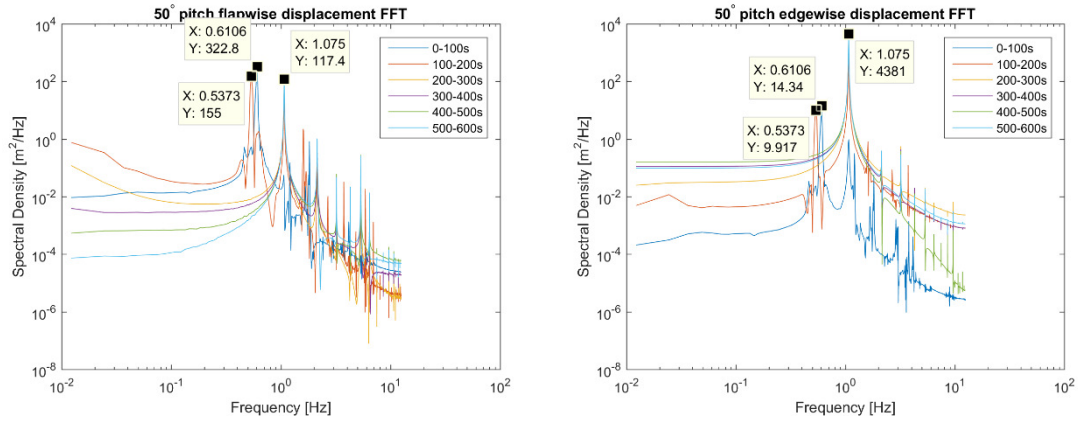

Figure A12: FFT of tip displacements blade 1 at 0° rotor azimuth, 50° blade pitch and 30° nacelle yaw in a) flapwise direction and b) edgewise direction with quasi steady aerodynamics

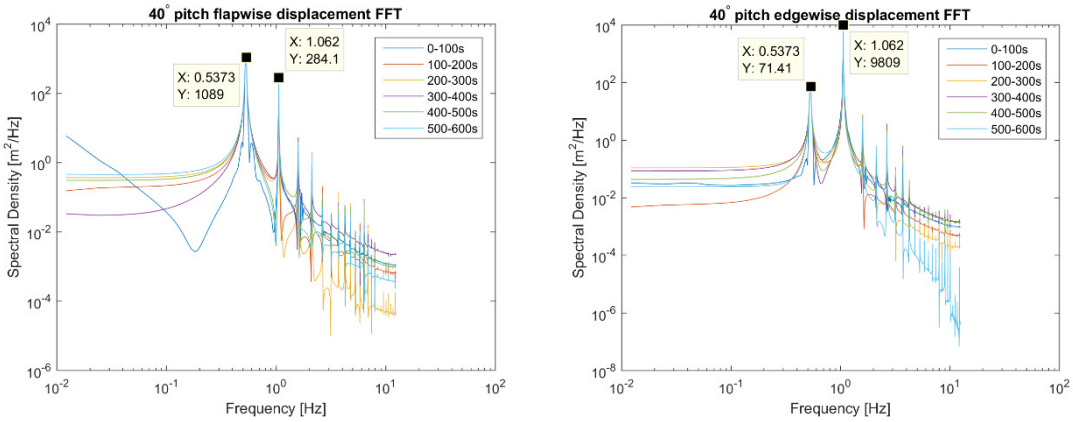

Figure A13: FFT of tip displacements blade 1 at 0° rotor azimuth, 40° blade pitch and 30° nacelle yaw in a) flapwise direction and b) edgewise direction with quasi steady aerodynamics

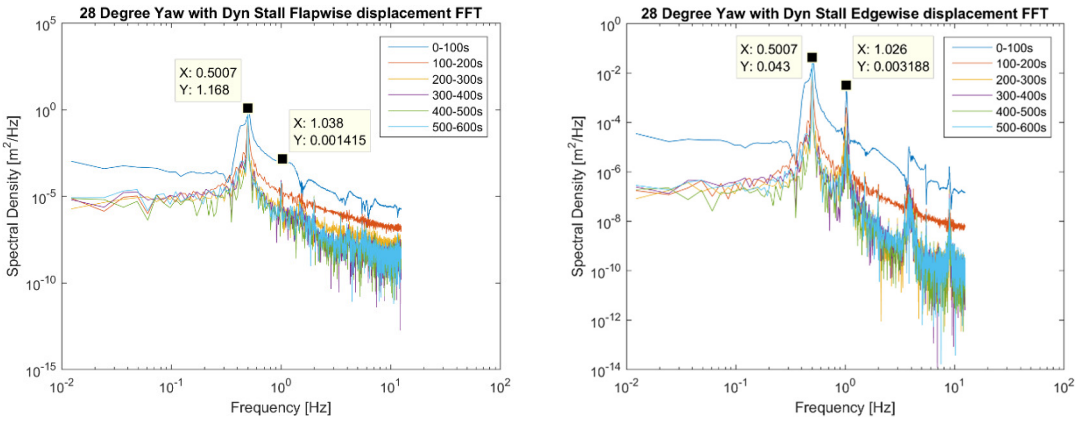

Figure A14: FFT of tip displacements blade 1 at 0° rotor azimuth, 90° blade pitch and 28° nacelle yaw in a) flapwise direction and b) edgewise direction with dynamic stall mode activated

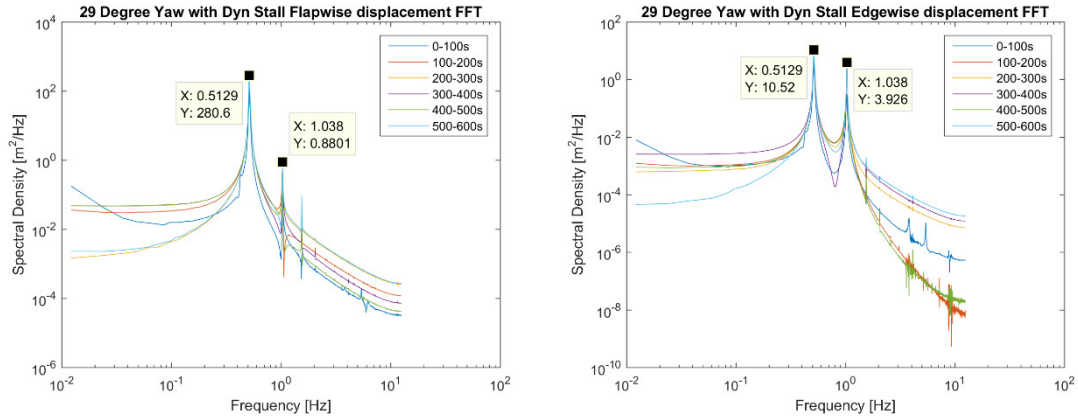

Figure A15: FFT of tip displacements blade 1 at 0° rotor azimuth, 90° blade pitch and 29° nacelle yaw in a) flapwise direction and b) edgewise direction with dynamic stall mode activated

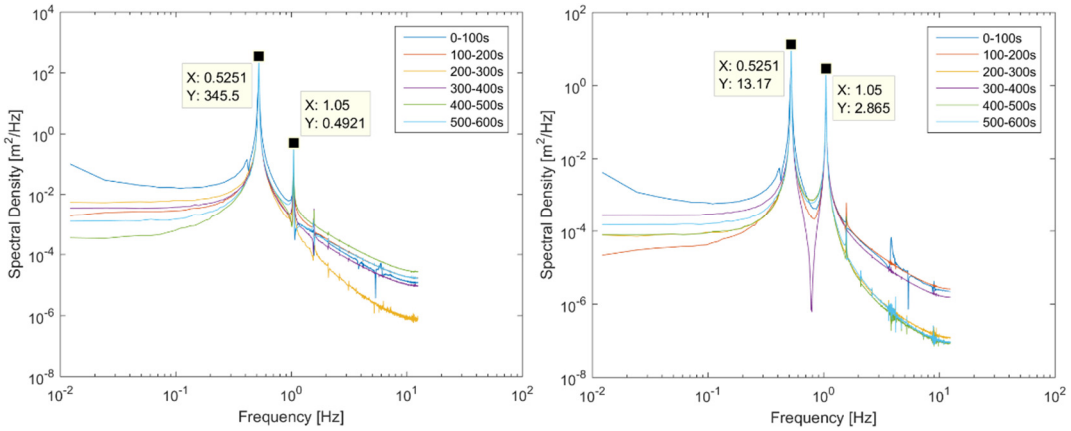

Figure A16: FFT of tip displacements blade 1 at 0° rotor azimuth, 90° blade pitch and 30° nacelle yaw in a) flapwise direction and b) edgewise direction with dynamic stall mode activated

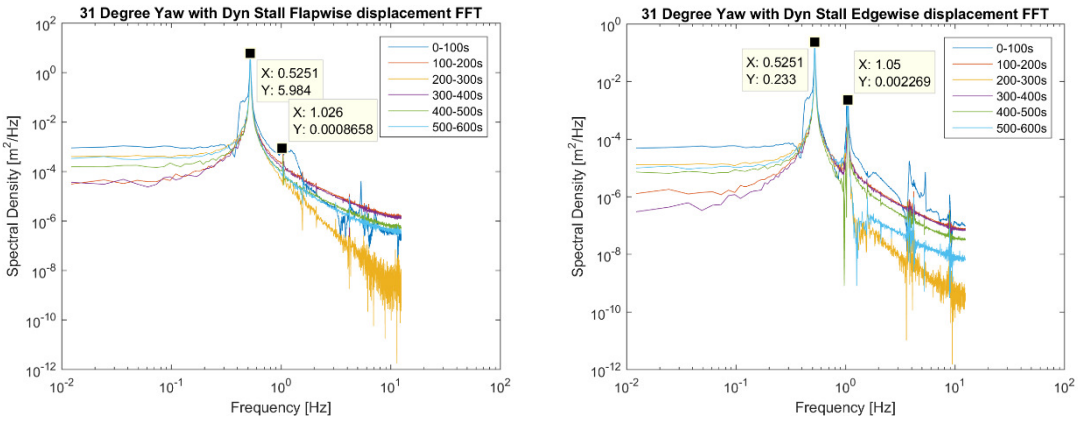

Figure A17: FFT of tip displacements blade 1 at 0° rotor azimuth, 90° blade pitch and 31° nacelle yaw in a) flapwise direction and b) edgewise direction with dynamic stall mode activated

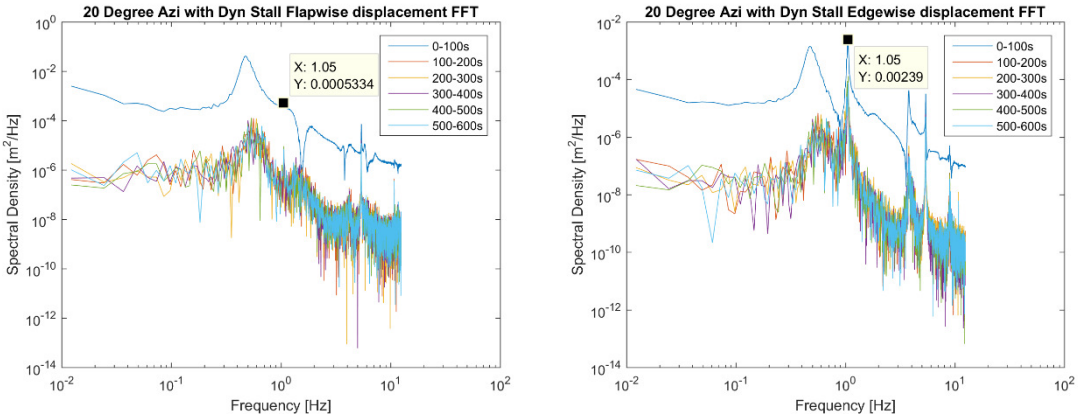

Figure A18: FFT of tip displacements blade 1 at 20° rotor azimuth, 90° blade pitch and 30° nacelle yaw in a) flapwise direction and b) edgewise direction with dynamic stall mode activated

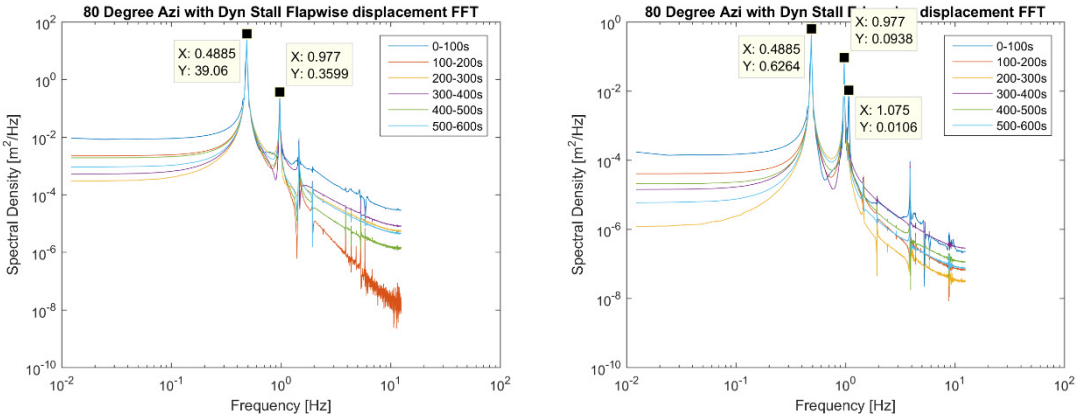

Figure A19: FFT of tip displacements blade 1 at 80° rotor azimuth, 90° blade pitch and 30° nacelle yaw in a) flapwise direction and b) edgewise direction with dynamic stall mode activated

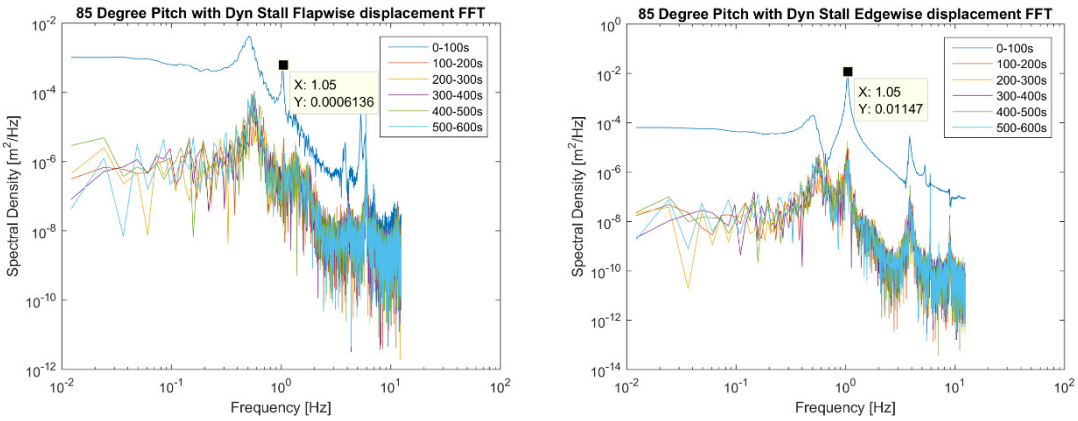

Figure A20: FFT of tip displacements blade 1 at 0° rotor azimuth, 85° blade pitch and 30° nacelle yaw in a) flapwise direction and b) edgewise direction with dynamic stall mode activated